Materials Today Advances 7 (2020) 100072

Contents lists available at ScienceDirect

Materials Today Advances

journal homepage: www.journals.elsevier.com/materials-today-advances/

Intercalation pseudocapacitance in electrochemical energy storage: recent advances in fundamental understanding and materials development

Y. Liu [a], S.P. Jiang [a], Z. Shao [a, b, *]

[a] WA School of Mines: Minerals, Energy and Chemical Engineering (WASM-MECE), Curtin University, Perth, WA, 6845, Australia
[b] State Key Laboratory of Materials-Oriented Chemical Engineering, College of Chemical Engineering, Nanjing Tech University, Nanjing, 210009, PR China

ARTICLE INFO

Article history:
Received 24 February 2020
Received in revised form
2 April 2020
Accepted 3 April 2020
Available online 18 May 2020

Keywords:
Lithium-ion batteries
Supercapacitors
Ion intercalation
Perovskites
Fast reaction kinetics

ABSTRACT

Electrochemical energy storage (EES) plays an important role in personal electronics, electrified vehicles, and smart grid. Lithium-ion batteries (LIBs) and supercapacitors (SCs) are two of the most important EES devices that have been widely used in our daily life. The energy density of LIBs is heavily dependent on the electrode capacity, in which the charge storage proceeds mainly in three different mechanisms, that is, alloying, conversion, and intercalation. Conventional LIBs show high energy density, but the rate performance is usually unfavorable. As a comparison, the SCs, which store energy based on electrochemical double layer capacitance (EDLC) or surface Faradaic redox pseudocapacitance, shows outstanding rate performance, but the energy density is still much worse than LIBs. Recently, intercalation pseudocapacitance appears as a new type of EES mechanism which stores energy into the bulk of electrode through a battery-like intercalation process but behaves similar to an electrode of SCs (fast reaction kinetics). Such intercalation pseudocapacitance can effectively narrow the gap between SCs and LIBs in energy density and power density, providing a new opportunity for the development of advanced energy storage system with both high energy density and power density. Up to now, more and more reports about intercalation pseudocapacitive materials have been appeared in literature, however, a systematic analysis of the recent development in intercalation pseudocapacitance is still lack. In this article, we provided an in-time review of the recent progress in the understanding of intercalation pseudocapacitive process and the development of related electrode materials for EES. Importance was paid to the difference between Faradaic surface-redox pseudocapacitance and intercalation pseudocapacitance, as well between battery-like intercalation and pseudocapacitive intercalation. Both cation interaction (Li^+ and Na^+) and oxygen anion intercalation pseudocapacitance was summarized.

1. Introduction

Considering the tremendous demand and fast-increased consumption of non-renewable fossil energy and the resultant environmental concerns, it is essential to find alternative sustainable energy materials/resources and develop advanced clean energy utilization/conversion/storage technologies. Solar and wind energies are important sustainable and clean energy resources for the future. However, owing to their intermittent nature and low energy density, the practical use of these energies should be integrated with efficient energy storage technologies. For this consideration, recently, electrochemical energy storage (EES), characterized by high energy density, compact size, and easy modulation, has received considerable attention, which can store the electricity as produced from wind/solar power via wind turbine/solar cells and then use in mobile transportation or electric grid for peak power leveling off. There are many types of EES technologies, including regenerative fuel cells, rechargeable batteries (lithium-ion batteries [LIBs], sodium-ion batteries, metal-air batteries, lithium-sulfur batteries), and supercapacitors (SCs). Among them, LIBs and SCs have been paid particular importance.

LIBs have the highest energy density among all the various battery technologies available today (100–265 Wh kg^{-1} or 250–670 Wh L^{-1}), which is partially resulted from their high cell voltage (3.6 V, 3 times higher than technologies such as Ni-Cd or Ni-

* Corresponding author.
E-mail address: shaozp@njtech.edu.cn (Z. Shao).

https://doi.org/10.1016/j.mtadv.2020.100072

MH) [1–3]. Based on the mechanism of electrode reaction, the LIBs electrode can be classified into three types, alloying, conversion, and intercalation. Silicon and tin are typical alloying-type electrodes, which show high theoretical capacity, but are suffered from large volume change during the alloying-dealloying processes, bringing big challenge for practical application. The conversion reaction normally occurs on the transition metal compound electrodes without any vacant sites in their crystal structure. Typically, 2–3 Li ions may be stored per atom of chalcogenide (e.g. O, S, etc.) or transition metal (e.g. Fe or Cu) in conversion-type cathodes. Although conversion reaction-based materials have aroused extensive attention owing to their high theoretical specific capacities, they are challengeable for practical application due to large irreversible capacity at room temperature, especially for the first cycle. The intercalation refers to the reversible exsolution or insertion of a molecule (or ion) into compounds with layered structures. The first generation of commercial LIBs with high energy density were built from interaction-type $LiCoO_2$ positive electrode and carbon negative electrode. Both $LiCoO_2$ cathode and graphite anode are in layered structure, and the lithium can intercalate into their layer spaces during charge or discharge process, meanwhile a phase transition is usually accompanied. During the past, great interests have been given to the development of highly active electrode materials with intercalation reaction. The main drawback of intercalation-type electrodes in LIBs may be the poor rate performance because of the relatively low lithium diffusion rate.

SCs are another important type of EES devices, which show the advantageous features of excellent power density (up to 10,000 W kg^{-1}) and superior cycling stability (up to 20,000 cycles). According to the charge-storage mechanism, SCs are typically classified into two categories: electric double-layer capacitors (EDLCs) and pseudocapacitors. EDLCs physically store charges (physisorption) by forming an electric double layer at the interface between the electrode and electrolyte. The drawback of SCs based on EDLCs is that the energy density is much lower than LIBs, although cycling stability is far better. By contrast, pseudocapacitors can store charges via not only the formation of an EDL but also reversible oxidation-reduction (redox) reactions with fast insertion of the electrolytes on the surface layer of the electrode. The presence of pseudocapacitance can greatly increase the energy density of SCs, while cycling stability is still favored. As claimed by Dunn's previous report, the pseudocapacitors have three different mechanisms, including underpotential deposition, redox pseudocapacitance and intercalation pseudocapacitance [4]. Particularly, intercalation pseudocapacitance happens by the intercalation of ions into the tunnels or layers of redox-active materials together with a Faradaic charge transfer without the appearance of crystallographic phase transition, similar to the ion intercalation in LIB electrode for which a phase transition is however usually accompanied. For instance, Dunn et al. [5–7] have investigated the feasibility of this expectation in their pioneering work on intercalation pseudocapacitance of T-Nb_2O_5. The key requirement for intercalation pseudocapacitance is a crystal structure that can provide two-dimensional fast ion diffusion channels and is sufficiently stable to prevent structural phase transitions during the ion intercalation. Because the intercalation pseudocapacitance can extend the charge storage in SCs from the electrode surface into the electrode bulk, a further increase in energy density is expected.

With increased sophistication of modern electronics and quickly expanded demand from mobile transportation and large-scale energy storage, there are more stringent requirement on EES systems that should be safer and cheaper and have much improved energy density, cycling stability, and rate performance, as compared with the state-of-the-art LIBs with $LiCoO_2$ cathode and graphite anode. Accordingly, new advances in materials and energy storage mechanisms are urgently needed. Nowadays, with the advances in nanotechnology, the difference between LIBs and SCs become smaller and smaller. For example, the energy density and power density of LIBs and SCs become ever closer. This is owing to the fact that pseudocapacitance may contribute significantly to the energy storage in LIBs as well. On the other hand, the introduction of intercalation pseudocapacitance into electrode system may break the bottleneck effect of energy density of conventional SCs. Actually, the intercalation pseudocapacitance has acquired considerable attention from the research communities recently, which may significantly increase the energy density of SCs or power density of LIBs. As a result, simultaneous achievement of high energy density, high power density, and long cycling lifetime could be realized.

Some layered-structured crystalline materials can offer fast two-dimensional ion transport pathways with almost no kinetics limitations from solid-state diffusion, giving rise to an intrinsic pseudocapacitive behavior. In addition, the ions in the electrolyte provide a wide potential window, leading to higher energy density than the conventional electrodes. Besides cations, oxygen anion intercalation pseudocapacitance has also been recently demonstrated in aqueous alkaline electrolyte at room temperature. In 1975, Kudo et al. [8] first reported that a reversible electrochemical intercalation of oxygen into the crystal lattice of $Nd_{1-x}Sr_xCoO_{3-\delta}$ perovskite oxide was demonstrated in a KOH solution at room temperature. The diffusion constant was calculated to be 1.4×10^{-11} cm^2 s^{-1}, much larger than that of most ordinary oxides [8]. The use of aqueous solution as electrolyte in anion intercalation-type SCs brings about environmental benignity and safe operation. As well, high ionic conductivity can be easily achieved for aqueous solution, enabling high power density and excellent rate capability. Recently, several perovskite oxides have been studied as electrodes of oxygen anion intercalation-type SCs. Compared with Li^+ or Na^+ cations, which just contain one positive charge per unit, O^{2-} can carry two negative charges per unit, which means that the intercalation pseudocapacitance of O^{2-} can store twice charges in one charge/discharge cycle than that of Li^+ intercalation in principle.

Although intercalation pseudocapacitance has been proposed and received increasing importance in both LIBs and SCs, and both cation and anion intercalation pseudocapacitance has been reported, the results about this research field are really scattered and a comprehensive review is still lack. In this review, we will first discuss the fundamental knowledge of intercalation pseudocapacitance in energy storage devices, focusing on the distinctions between the intercalation pseudocapacitance, and other energy storage mechanism in different devices. The second part of this review illustrates the materials which can exhibit the intercalation pseudocapacitive behavior. In particular, we highlight the layered metal oxides for cation intercalation pseudocapacitance and the perovskite oxides for the oxygen anion intercalation pseudocapacitance. Finally, after providing a conclusion of this review, the insights and prospective on the role of intercalation pseudocapacitive electrodes in future energy storage field are proposed.

2. Fundamentals of intercalation pseudocapacitance

Pseudocapacitance is defined as the electric power stored in a pseudocapacitor via fast Faradaic charge transfer, which is realized through a rapid sequence of reversible Faradaic redox, electrosorption, or intercalation processes on the surface or of appropriate electrodes, or even penetration into the electrode bulk. The principle of pseudocapacitance is defined by Conway in his book titled 'Electrochemical Supercapacitors: Scientific Fundamentals and

Technological Applications' [9]. For a regular SC, the charge is stored via the formation of EDLC, as shown in Fig. 1. For this charge-storage mechanism, the capacitance is strongly dependent on the electrode surface area. Activated carbon is the most well-known electrode material for EDLC, which has the modest capacitance of up to 200 F cm^{-1} owing to the limitation of specific surface area. The typical pseudocapacitance also arises from the electrode surfaces but an associated Faradaic charge-storage reaction is involved. This capacitance is called 'pseudocapacitance' because it originates in a quite different way from that corresponding to classical electrostatic capacitance of double layer.

During the past, on the basis of different Faradaic mechanisms, there are mainly two types of pseudocapacitance, as shown in Fig. 2 [4,9]. The first one is underpotential deposition. It occurs when cations in the electrolyte generate an adsorbed monolayer on the surface of metal electrode with a higher redox potential. For example, the Pb^{2+} underpotential deposition processes taking place at a certain potential on the surface of Au electrode can provide pseudocapacitance [10]. The second one is the more popular redox pseudocapacitance. It primarily takes place on the electrode surface or subsurface with an associated Faradaic charge transfer between the ions in the liquid electrolyte and the solid electrode. For instance, the redox processes were observed upon potential cycling and involved the 2^+, 3^+, and 4^+ oxidation states in RuO_2. This process coupled with proton transfer giving rise to pseudocapacitance is predominant in the charging mechanism [11].

More recently, a new third type, so-called intercalation pseudocapacitance, was proposed (Fig. 2c). It occurs when the intercalation of ions into the tunnels or layers of a redox-active material and accompany with a fast Faradaic charge transfer without the change of crystallographic phase. Therefore, it retains an ultrastable structure in electrochemical reaction. As aforementioned, Faradaic redox pseudocapacitance occurs only on the surface of materials and the electrolyte ions never insert into the bulk of electrode. However, the intercalation process will allow the ions occupy the tunnels or vacancy position inside the bulk of materials. Such intercalation process is so fast that it behaves like the electrode reaction of a SC other than a battery. Consequently, the rate capability of intercalation pseudocapacitive materials is normally much better than battery materials. A big difference in galvanostatic charge and discharge profiles between intercalation pseudocapacitance and battery-like intercalation is that the intercalation pseudocapacitance displays sloping charge-discharge profiles similar to EDLC and surface-redox pseudocapacitance, whereas battery-like intercalation processes typically present apparent plateaus in their charge-discharge profiles (Fig. 3). This is owing to the fact that, for battery-like intercalation, the materials always undergo crystallographic phase transformations. In addition, electrode based on intercalation pseudocapacitance usually exhibits higher rate capability than intercalation-type battery-like electrode, which is mainly attributed to the higher kinetics of the former reaction because of no phase transition is accompanied [12]. Battery-like intercalation usually has a great voltage hysteresis between the charge and discharge steps. The voltage of a battery-like intercalation cell is determined by the free enthalpy of the ion exchange reaction, which consists of cation intercalation and deintercalation reactions at the active electrode materials. For the intercalation pseudocapacitance, the potential is determined by any irreversible electrode reaction, such as composition and/or concentration of the solution and irreversible redox reactions in the electrodes. High valent niobium oxide (Nb_2O_5) is a typical electrode material of lion-ion intercalation-type pseudocapacitor [13]. Nevertheless, only very few crystalline materials have a structure that can fulfill the strict demands of fast ion transport pathways and insignificant structural transition upon ion insertion and extraction to induce intercalation pseudocapacitance.

Normally, the intercalation pseudocapacitive behavior of most materials shows no dependence on the particle size and morphologies. Perovskite oxides, T-Nb_2O_5 and TiO_2-B are typical intercalation pseudocapacitive materials [14]. For some other materials, the intercalation pseudocapacitive behavior is only happened when the particle size is reduced to nanoscale. Within the nanosized particles, the battery-like intercalation behavior is replaced by the intercalation pseudocapacitance. The phase transformation during the intercalation progress is suppressed owing to nanostructuring of the electrode material. Both the nanocrystallization and suppression of phase transformation are beneficial for improving the high-rate behavior of electrode at high discharge current density range. It could probably because that the nanoparticles decrease the ion diffusion distance and the no-phase transition diminishes the energy barrier, thus the electrochemical reaction over this type of electrode becomes highly kinetic [4,12]. Many typical battery electrode materials, such as MoO_3, V_2O_5, and $LiCoO_2$, possess this property. For example, the first charge

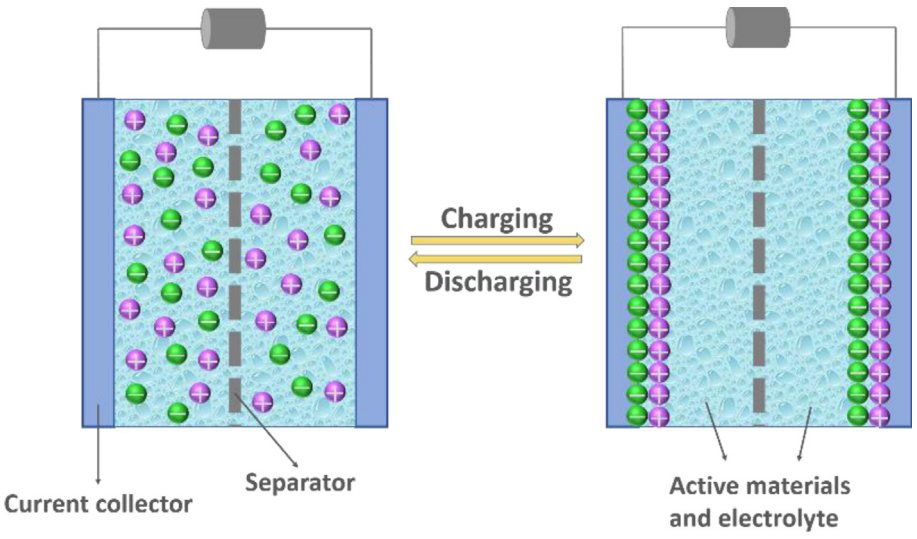

Fig. 1. Charge-storage mechanism of EDLC.

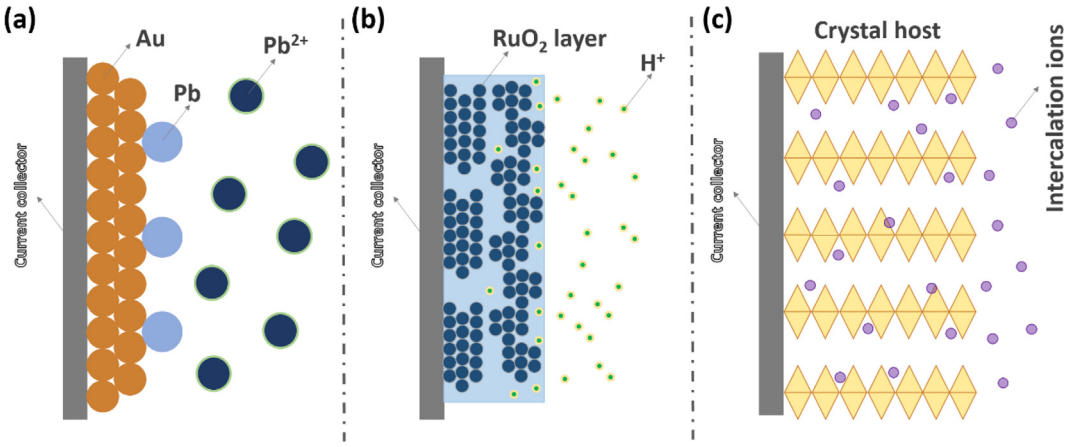

Fig. 2. Three different reversible pseudocapacitance: (a) underpotential deposition; (b) Faradaic redox pseudocapacitance, and (c) intercalation pseudocapacitance.

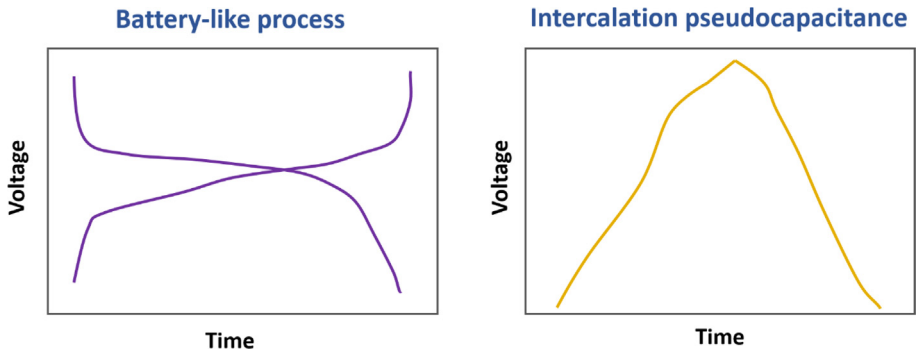

Fig. 3. The typical galvanostatic charge/discharge curves of battery-like process and intercalation pseudocapacitance.

capacitance of $LiCoO_2$ was found to increase with decreasing particle size when it was applied as an electrode of LIBs (Fig. 4). In addition, there is no obvious voltage plateau when the particle size is smaller than 11 nm. Thus, intercalation pseudocapacitance became more dominant with decreasing particle size. Compared with bulk $LiCoO_2$, nanosized $LiCoO_2$ electrode had an excellent rate capability at high current densities [15]. Cao et al. [16]investigated the intercalation pseudocapacitance of *d*-MoO_3 which promoted by the nanoscaling progress. They found that this pseudocapacitance contribution to the Li ion storage well explained the high rate performance and the capacity. This significant contribution could be ascribed to the reduced ion diffusion path and the increased surface ion storage sites.

Similar to other types of pseudocapacitive behavior, intercalation pseudocapacitance happens whenever the charge (Q) relies on the alteration in potential (dE), generating a capacitance (dQ/dE). Although Faradaic exists in nature in the electrochemical processes, their phenomenological behavior, as well as response to experimental variables such as sweep rate, is typical for capacitors. These processes yield a relationship between the fractional extent of charge storage, X, and the potential as the following:

$$E \sim E^0 - \frac{RT}{nF}\ln(\frac{X}{1-X})$$

where E signifies the measured potential (V) for oxygen intercalation, E^0 is the standard potential (V) for ion intercalation, R means the ideal gas constant (8.314 J mol^{-1} K^{-1}), T represents the temperature (K), n symbolizes the number of electrons, F means the Faraday constant (96.485 C mol^{-1}), and X represents the extent of fractional coverage of the surface or inner structure. Intercalation pseudocapacitance exhibits indicative of ion diffusion-controlled electrochemical processes:

$$i = Cv^{1/2}$$

where *i* represents the current (A) and v means the sweep rate (mV s^{-1}) of a cyclic voltammetry experiment [6].

Owing to Faradaic charge transfer involves for both the surface faradiac redox pseudocapacitance and intercalation pseudocapacitance, it is very difficult to distinguish these two processes just by the shape of cyclic voltammograms (CV) and galvanostatic charge/discharge curves. For practical SCs, the total charge stored may be a combination of aforementioned three parts: the Faradaic contributed by the insertion process of the cations/anions (intercalation pseudocapacitance), the Faradaic contributed by the process of charge and transfer with surface atoms (surface-redox pseudocapacitance), and the non-Faradaic contributed by the double layer effect. To analyze the role of intercalation pseudocapacitance, it is very important to separate the contribution of intercalation pseudocapacitance from the total capacitance. In the CV curves, the charge-storage process determines the current response (i) upon the variation of the sweep rate (ʋ). To be specific, the effects of diffusion-controlled intercalation process and surface-induced capacitive process could be distinguished from the power-law relationship

$$i(v) = av^b$$

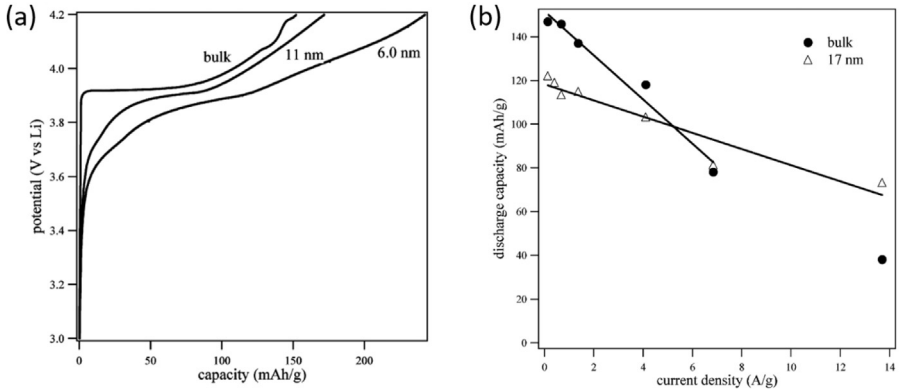

Fig. 4. Crystallite size dependence of (a) the first charge curves for $LiCoO_2$ (bulk, 11 and 6 nm), (b) rate capability plot the nanosized 17 nm $LiCoO_2$ and bulk $LiCoO_2$. Reprinted with permission from a study by Okubo [15]. Copyright (2007) American Chemical Society.

where a represents a constant and b means the power-law exponent. The value of b value could be achieved by the slope of the plot of log(*i*) versus log(υ) with regards to the cathodic and anodic peaks. On the basis of the value of b, the qualitative determination can be carried out for the kinetics of the charge-storage mechanism, whereas b equals to 0.5, and the *i* is proportional to the square root of the ν and controlled by the semi-infinite linear diffusion, b value of 1 indicates that the current is surface controlled [17,18]. For example, Augustyn et al. [6] tested the T-Nb_2O_5 electrode in 1 M $LiClO_4$ electrolyte in propylene carbonate from 0.1 to 500 mV s^{-1} by CV. When sweep rates range from 0.1 to 20 mV s^{-1}, which correspond to charging times >60 s, the b-value for both cathodic and anodic peaks is 1, demonstrating that the kinetics are controlled by surface, and thus are very fast. At sweep rate higher than 50 mV s^{-1}, the b-value, owing to slow diffusion, decreases to 0.7.

2.1. Cation intercalation process

The key requirement for realizing cation intercalation pseudocapacitance of an electrode material is that it should have a crystal structure with two-dimensional fast ion diffusion channels and sufficient stability to prevent structural phase transition during the ion intercalation. For the mechanism of intercalation storage controlled by diffusion, which accords with the typical charge-storage behavior of battery materials, the Faradaic reaction takes place in the bulk phase with the deep diffusion of ions into interlayer gaps (or van der Waals gaps) [6,19]. If intercalation is fast enough in kinetics, pseudocapacitance may appear. However, such materials are few [4]. Up to now, several cations, including Li^+, Na^+, K^+, Mg^{2+}, and Al^{3+}, have shown the capability of electrochemical intercalation in a pseudocapacitive way, providing capacitance over 300 F cm^{-2} (much higher than that of porous carbons). With the increase of the ionic radii of intercalated cation, the ionization energy and the electronegativity decrease gradually. After the systematic investigation, Zhao et al. [20]found that the limitation of cycling ability and rate capability could be overcome by suitable intercalation of alkali metal ion in admissible layered structure. This is ascribed to the synergistic stabilizing influence between intercalated ions and the layers with appropriate layer — surface configuration in charge — discharge processes together with the enlarged layer spacing. Nanocrystalline Nb_2O_5 films was demonstrated storage capacities of approximately 130 mAh g^{-1} at a rate of 10 C (charge/discharge in 6 min) for Li^+ ions in organic electrolytes. The unique open tunnels in the crystal structure of T-Nb_2O_5, provided by the mostly vacant octahedral sites between (001) planes throughout the a-b plane, allow the fast transport of Li^+, leading to the high-rate capability [6]. Such open tunnels diminish the energy barrier and promoted the local charge transfer between lithium and oxygen structures [21]. Another example is that high-rate capability and long cycle life of a sodium-ion battery could be achieved by intercalation pseudocapacitance of Na^+ in TiO_2/graphene nanocomposites. A specific capacity in excess of 90 mA h g^{-1} was achieved by this hybrid at a high current density of 12 A g^{-1} (~36 C), which showed high reversibility for over 4000 cycles. The unique chemically bonded hybrid structure offered a more facile channel for Na^+ to insert/extract in the graphene–TiO_2 interface, led to the pseudocapacitive behavior of Na^+ intercalation into the TiO_2/graphene composite [19].

2.2. Anion intercalation process

Recently, the intercalation pseudocapacitance induced by oxygen ion intercalating into the lattice of electrode materials has also attracted great attentions [22–27]. Owing to the bulk intercalation mechanism, high capacity is no longer ensured by high surface area [22]. Compared with conventional Li^+ or Na^+ (which has one positive charge per unit) intercalation pseudocapacitance, O^{2-} can carry two negative charges per unit, which means that the intercalation pseudocapacitance of O^{2-} can store twice charges in one charge/discharge cycle than that of Li^+ intercalation in principle. Thus, the oxygen-ion intercalation is expected to possess a higher ability of energy storage than monovalent ion intercalation. Mefford et al. [28] first demonstrated that a novel type of SCs which stored energy through oxygen-ion intercalation into $LaMnO_3$ perovskite oxide lattice in an aqueous KOH electrolyte. They proposed oxygen-ion intercalation pseudocapacitance mechanism as follows: Initially, the diffusion of oxygen in the form of hydroxide anion occurs from KOH electrolyte to active electrode material surface. Subsequently, the oxygen vacancy is intercalated by the oxygen of hydroxide anion, which diffuses into lattice with the oxidation of B elements. Meanwhile, the proton transfers to hydroxide anion in electrolyte and yield water as a product. In the next step, the superfluous oxygen intercalates into perovskite lattice and the surface of lattice through diffusion of B site elements. During this process, a slight shift of the positive charge centers of B elements on the surface occurs toward the oxygen-ions intercalation, causing B elements to have high chemical valence states. Based on aforementioned mechanism, we propose that there are three factors of perovskite oxides mainly determining the oxygen-ion intercalation pseudocapacitive behavior, including oxygen vacancy concentration, electric conductivity and phase stability. The oxygen vacancies not only provide ‘spaces’ or charge-storage sites

for oxygen-ion intercalation but also could improve the oxygen diffusion rate and the conductivity. This is owing to the fact that oxygen vacancies are especially vital for oxygen ionic conduction [29]. Therefore, higher oxygen vacancy concentration gives rise to higher specific capacitance and electrochemical performance of perovskite electrodes. High conductivity of perovskite electrodes are favorable to high power densities of perovskite oxides, which could shorten the charge/discharge time of SCs. The stable crystalline structure of perovskite oxides ensures the long stability of electrode under the electrochemical condition in the neutral or alkaline electrolyte. Therefore, designing a perovskite oxide with high oxygen vacancy concentration, conductivity and stable crystalline phase is expected to obtain high performance in terms of oxygen-ion intercalation-type SC. After that, plenty of perovskite oxides have been reported as the oxygen-ion intercalation pseudocapacitive electrodes in the SCs [22,27,30–33].

3. Advances in materials development

3.1. Cation intercalation process

3.1.1. Li-ion intercalation

3.1.1.1. Ti-based materials. Titanium oxides and titanium-based compounds have been most extensively investigated as electrode materials that show Li-ion intercalation-type pseudocapacitance. (Table 1) Through studying the electrochemical performance of TiO_2 in 1 M solution of $LiPF_6$-based electrolyte, the intercalation pseudocapacitive behavior of TiO_2 was declared by Li et al [34]. They found that Li ion could intercalate into and deintercalate from the TiO_2 lattice easily and reversibly:

$$Ti_2 + x(Li^+ + e^-) \rightarrow Li_xTiO_2$$

In the CV curve of TiO_2, there are two pairs of reversible pseudocapacitive peaks which are ascribed to the lithium-ion intercalation. These peaks significantly enhance the storage capacity of Li, owing to a more favorable stoichiometry.

Charge-storage mechanism and storage ability of TiO_2 is highly dependent on the material's crystallography and microstructure. The TiO_2 oxides that have more open structure of morphology and lattice, higher surface area, and lower degree of crystallinity, usually show better intercalation pseudocapacitive performance. Li et al. [35] demonstrated that the TiO_2 nanotube electrode possessed large lithium intercalation pseudocapacitance. Wang et al. [36] showed that the intercalation pseudocapacitive contribution to the whole charge storage could be improved by reducing the particle size of TiO_2. They also pointed out that a more rapid charging rate was exhibited by the smaller particles than the larger ones for lithium-ion storage [37]. Thus, not only higher amounts of total charge storage but also more rapid charge/discharge rates could be achieved by reducing particle size of TiO_2 to the nanoscale regime. The amount of charge stored at the surface of TiO_2 from the intercalation pseudocapacitance in nanomaterials could be comparable with that obtained from the intercalation process in bulk materials [38]. Huang et al. [39] prepared 3D TiO_2 nanomembranes by physical vapor deposition combined with strain-released rolled-up technology. The electrochemical testing results demonstrated that the crystallinity degree determined the pseudocapacitance contribution. The pseudocapacitive contribution of higher crystallinity TiO_2 is much lower than that of amorphous TiO_2. As to the crystal structure, anatase and TiO_2-B are the two most active forms of TiO_2 polystructures for lithium insertion and extraction. It was reported anatase TiO_2 had the reversible insertion number x as high as 0.5 at room temperature [40,41]. Various ways to improve the intercalation capacitance of TiO_2 electrode have been extensively tried.

For pure phase TiO_2-B, it was found pseudocapacitive Faradaic process governed the Li^+ ion into the material lattice, whereas solid-state diffusion of Li^+ did not limit its rate in a broad interval of scan rates. This distinctive behavior was attributed to the unique crystal structure of the TiO_2-B host which possessed accessible parallel channels for Li^+ free transport perpendicular to the (010) face [42]. Based on density functional theory (DFT) calculation, it was demonstrated that the lithium ion was bound at a site near the titania octahedral layer in accordance with first-principles calculation, whereas the lowest activation energy of 27 kJ mol^{-1} was observed for diffusion along the open channel which was parallel to the b axis of the material. In terms of the electrochemical behavior of this polymorph of titania, this prediction seems to be consistent with experimental results [43]. As illustrated in Fig. 5, the surface-affected relative stability of the sorption sites, which is prevented lithiated TiO_2-B from structural anisotropic expansion. Each surface absorption site is in connection with the interior via a low-energy radial pathway, bringing Li ion to absorb almost independently to its trapping site, which resulted in pseudocapacitive behavior of TiO_2-B nanowires in terms of Li-ions [44]. To further improve the intercalation capacitance, various synthesis methods have been tried to obtain TiO_2-B with different morphological shapes. For example, Chen et al. [45] prepared TiO_2-B nanobelts by microwave irradiation, which showed high specific capacity contributed from the intercalation pseudocapacitance. In another study, multiple TiO_2-B nanosheets stringed by 1D nanowire were prepared which showed efficient transfer pathway for ion and electron and excellent structural stability, resulting in the superb electrochemical performance with pseudocapacitive behavior [46]. TiO_2-B nanowires were also reported to show Li^+ intercalation pseudocapacitance in Li^+/Mg^{2+} hybrid-ion batteries [47].

The intercalation pseudocapacitance of TiO_2 anatase was also extensively exploited. Kang et al. [48] used a first-principles method for the calculation of the electrochemical capacitance of TiO_2 anatase nanosheets. As can be seen from Fig. 6a&b, TiO_2 nanosheet is a combination of SC and battery, exhibiting both characteristics relying on electrode potential. When positive electrode potential is higher than 2.2 V versus Li/Li^+, the system functions as a capacitor via forming electric double layers at the surface. When the electrode potential is lower than the threshold, lithium will intercalate into the interior, which is facilitated by the surface charge transfer pseudocapacitance. However, the difficulty

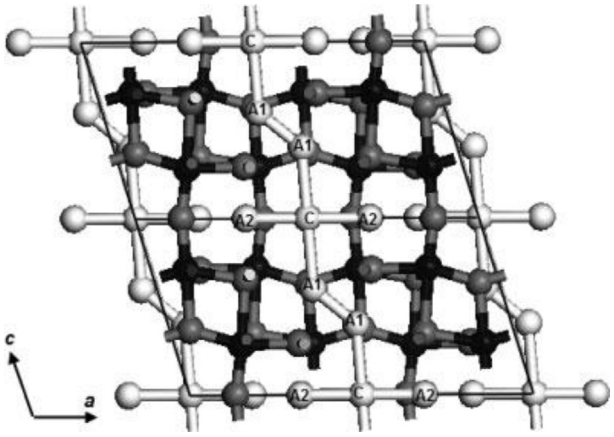

Fig. 5. Long energy pathway for Li diffusion in TiO_2-B. (Ti ions are shown in black, O ions in gray, Li ions in white) Reprinted with permission from a study by Koudriachova [44]. Copyright (2010) John Wiley & Sons, Ltd.

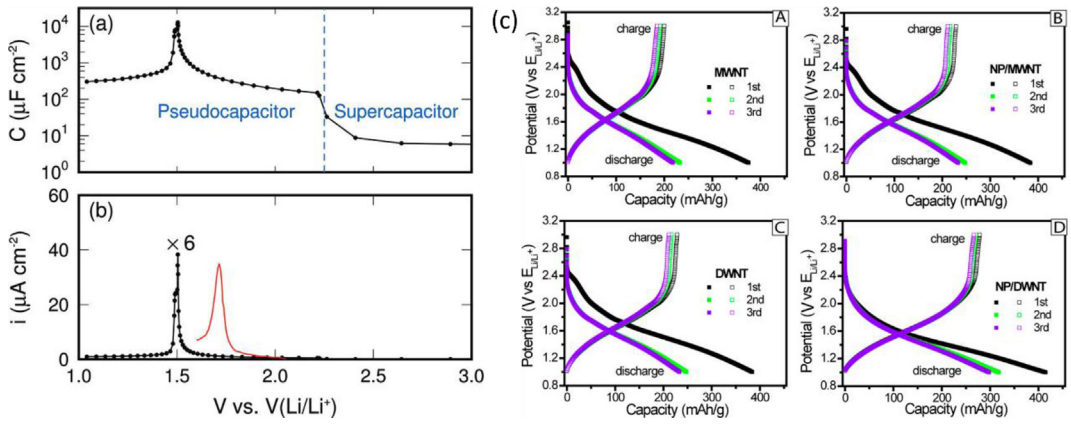

Fig. 6. (a, b) The potential-capacitance plot is redrawn with the potential V vs V(Li/Li$^+$); (c) Potential-capacity plots for both charge and discharge processes for TiO_2-B with different nanotubes. Reprinted with permission from a study by Kang et al. [48] and Qu et al. [52]. Copyright (2011) American Chemical Society; Copyright (2014) American Chemical Society.

in the separation of capacitive behavior from the insertion behavior controlled by diffusion might be a major issue. Brezesinski et al. [49] distinguished capacitive processes and slower diffusion-controlled processes by electrochemical analytical methods. They found that less capacitive storage was exhibited by the mesoporous films fabricated by $TiCl_4$ than those prepared by TiO_2 nanoparticles. Large surface area and mesoporous structure are beneficial to the intercalation pseudocapacitance. Sussman et al. [50] found that enhanced surface area and capability for pseudocapacitive storage of Li ions at high rate resulted in high capacity of the anatase TiO_2. To improve the pseudocapacitance associated with Li^+ intercalation in TiO_2, Hao et al. [51] synthesized a biomimetic layer-by-layer TiO_2. This material has pseudocapacitive storage associated with surface and bulk diffusion storage, and the former played a dominant role in the total capacity if the scan rates are higher than 1 mV s^{-1}. Such a rapid and stable lithium storage performance is likely to be resulted from the high contribution of pseudocapacitive storage at high rates, which was occurred at nanocrystal interfaces, as well as nanosheet surfaces. TiO_2 nanotubes decorated by TiO_2 nanoparticles was prepared by Qu et al. [52] to enhance the electrode capacity. In accordance with the CV test (Fig. 6c), sloping characteristics with no voltage plateaus in the cycles of lithiation/delithiation in terms of all four samples implies that homogeneous insertion/extraction of Li ions occurred in the electrode with no phase transition between Li_xTiO_2 and TiO_2, which is typical of intercalation pseudocapacitance. Therefore, pseudocapacitive nature in the processes of lithiation/delithiation in the bulk, as well as on the surface determines the high rate capability of this electrode. As a result, up to 163 mAh g^{-1} of capacity could be achieved even at a high current density of 2000 mA g^{-1}. In another study of the mixture electrode of TiO_2-B and anatase TiO_2 microparticles, it showed three different capacities, including homogeneous bulk lithium insertion, bulk intercalation storage, and pseudocapacitive storage [53]. The ratio of intercalation pseudocapacitance increased with anatase phase content in mixture [54].

Considering the poor electronic conductivity of TiO_2, the formation of composite with carbon (including carbon nanotubes (CNTs), graphite, graphene, fullerenes, carbon spheres, and so on.) was also tried for enhancing intercalation pseudocapacitance of TiO_2. Saruhan et al. [55] deposited the TiO_2 on the graphite substrate to yield randomly distributed fine pores and large surface area, which can be applied as the electrode of pseudocapacitive SCs. Sussman et al. [56] reported a binder-free fabrication of nano-TiO_2/carbon electrode with superior Li^+ intercalation properties. Hemalatha et al. [57] have investigated the charge-storage mechanism in TiO_2 coated on CNTs. The TiO_2/CNT composite could be an important electrode for high-performance SCs by combining the double layer effect of CNT and pseudocapacitance of TiO_2 because of intercalation/deintercalation of Li^+ in the TiO_2 crystal lattice. The contribution from intercalation and pseudocapacitance to the overall charge storage depends on the loading percentage of TiO_2 over CNTs as it influences the surface area and phase interface (Fig. 7). The pseudocapacitive contribution decreased with an increase in TiO_2 loading owing to the decrease of available TiO_2

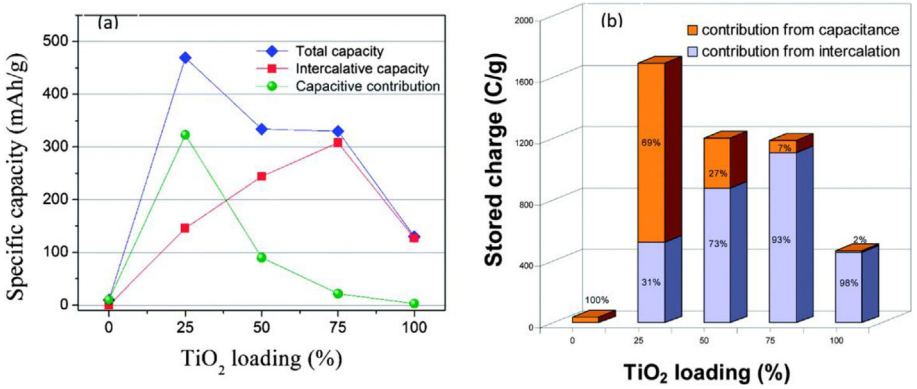

Fig. 7. (a) Plot of specific capacity of TiO_2/CNT as a function of different percentage of TiO_2 loading. (b) Bar chart representing charge stored as a function of different percentage of TiO_2 loading. Reprinted with permission from a study Hemalatha et al. [57]. Copyright (2014) The Royal Society of Chemistry.

surface which are covered by CNTs. Liu et al. [58] used the first-principle calculation to investigate the Li^+ intercalation in graphene/TiO_2 electrode. The graphene phase in the electrode acted as electron acceptor. With the interfacial Li atoms insertion, an additional electronic charge transfer toward the graphene was happened. The total capacity was contributed from surface, bulk, and interface storage. About 35% additional Li storage capacity beyond the TiO_2 theoretical capacity was from the surface and interface storage process via a pseudocapacitance-like energy storage mechanism. Li et al. [59] used the nitrogen-doped graphene as the substrate to support TiO_2. The electrochemical characteristics of the composite demonstrated a close relationship with this pseudocapacitive storage process. Consequently, the as-obtained composite exhibited about 183 mAh g^{-1} reversible discharge capacity after 100 cycles at a high rate of 10 C. Chen et al. [60] prepared TiO_2-B nanosheets featured by N-doped carbon, which demonstrated a capacity of 180 mAh g^{-1} at 6 A g^{-1}, about 72% of the total capacity belongs to intercalation pseudocapacitance. Senthil et al. [61] prepared nitrogen-rich carbon nanosheets wrapped anatase TiO_2 nanospheres electrode which delivered superior Li storage, cycle life, as well as rate performance, owing to the synergistic effect in enhancing electronic and ionic conductivities, structural flexibility, and mechanical stability of the electrode. This core-shell nanocomposites delivered a dual charge-storage contribution, which showed high rate performance and superior lithium storage contributed significantly from the pseudocapacitive lithium storage at interfaces, surface, and grain boundaries.

The poor electronic conductivity of pristine TiO_2 may also be mediated through introducing dopants into the oxide lattice structure, both for the Ti and O sites. Fehse et al [62] demonstrated that the partial density of states were similar for Nb 4d and Ti 3d, but the extra Nb 4d electron pushed the Fermi level from the highest of the valence band for undoped TiO_2 to the lowest of the conduction band for Nb-doped TiO_2. Thus, metallic conductivity was exhibited by Nb-doped anatase TiO_2 because this additional Nb 4d electron delocalized. At the low applied 0.5 C current rate, the Nb-doped TiO_2 showed a 180 mAh g^{-1} specific capacity; at the high rate of 86 C, this electrode still showed a specific capacity of 48 mAh g^{-1}. The enhanced high power performance of Nb-doped TiO_2 was resulted from its larger electronic conductivity, better lithium-ion diffusivity and a greater charge-storage contribution from surface effects such as pseudocapacitance [63]. Liu et al. [64] prepared a composite of heterogeneous TiO_2@Nb_2O_5, in which TiO_2 nanoparticles were in even embedding on ultrathin Nb_2O_5 nanosheets. The lithium storage process of this electrode was mostly dominated by the pseudocapacitive contributions. The impregnation of TiO_2 nanoparticles on Nb_2O_5 nanosheets provided a short distance to diffuse and more surface sites to store Li^+ ions. In addition, an excellent reversible capacity can be delivered by pseudocapacitive behavior of Nb_2O_5 at high current densities. The P-$Ti_2Nb_{10}O_{29}$ nanospheres with hierarchical structure were beneficial to the facile Li^+ intercalation/deintercalation kinetics through a short-length diffusion process and an intercalation pseudocapacitance occurred on the material surface. The intercalation pseudocapacitance, not related with the usual Faradaic Li^+ storage, did not cause phase transitions and was greatly conducive to the electrodes long-term cycling stability. As a result, about 61% of the total capacity was pseudocapacitive in nature at the scan rate of 0.5 mV s^{-1} for P-$Ti_2Nb_{10}O_{29}$ electrode [65].

The full substitution of O in TiO_2 by N or S was found to significantly improve the conductivity. After the replacement of O in the TiO_2 by N, the TiN still exhibited the capability of cation intercalation pseudocapacitance. The pseudocapacitance has witnessed an obvious increase following the order of $K^+ < Na^+ < Li^+$, opposite to EDLC. This is likely owing to the increase of effective reaction sites by cations with smaller bare ionic size [66]. Wen et al. [67] reported core/shell TiN/TiO_2 nanowire array to tackle these problems. The single-crystal–like TiN nanowire cores functioned as highly conductive nanostructured current collectors, and the branched shell was constructed by nanoporous anatase TiO_2 mesocrystals. This 3D nanoarray electrode exhibited a pseudocapacity-dominated charge storage of lithium ions with outstanding performance with respect to high areal and volumetric capacity, rapid charge/discharge ability, and lasting cycling lifetime. Sulfur doping into the TiO_2 could also improve the electrochemical properties. In the 1990s, Conway claimed that TiS_2 demonstrated pseudocapacitive characteristics, but whether the intercalation kinetics was in significant difference from bulk TiS_2 is not clear [68,69]. Muller et al. [70] characterized the characteristics of few-layer 2D-TiS_2 nanocrystals structurally and electrochemically and investigated their kinetics and charge-storage mechanism compared with micron-sized TiS_2 particles. Compared with relevant bulk materials, the two-dimensional morphology resulted in disparate behaviors. With regard to the bulk-TiS_2 materials, the kinetics was featured by diffusion-controlled behavior. However, for 2D-TiS_2, the kinetics exhibited capacitive-controlled behavior at low rates and the capacity altered linearly corresponding to diffusion-controlled behavior at high rates. In solid-state battery, the mechanism of pseudocapacitance would happen at the surface of a TiS_2 slab. The interfacial Li between $LiTiS_2$ and a-Li_2TiS_2 may lead to a pseudocapacitive behavior in the battery, which will provide additional room for possible improvement by engineering the solid-solid interface [71].

In addition to TiO_2, several titanium contained compounds also showed the intercalation-pseudocapacitance behavior. Wang et al. [72] fabricated layered $H_2Ti_6O_{13}$ nanowires and tested their Li-storage behavior in a non-aqueous electrolyte. Owing to the nanosize feature and expanded interlayer space of nanowire, this electrode exhibited a typical pseudocapacitive characteristic of Li^+ intercalation. It reached a capacitance of about 830 F g^{-1} with the potential window range of 2.0 to 1.0 V versus Li/Li^+. However, Byeon et al. [73] did not find any evidence that the increase in capacitance of hydrogenated TiO_2 was due to pseudocapacitance compared with pure TiO_2. The layered $H_{1.1}Na_{0.9}Ti_3O_7$ electrode displayed a intercalation pseudocapacitance that occupied 42% of overall capacity at 0.5 mV s^{-1} scan rate, which was increased to 53% of overall capacity at 1.5 mV s^{-1} [74]. Both nanowires and nanotubes of hydrogen titanate were prepared for lithium storage, which did not exhibit microstructure and morphology changes after decades of cycling [75]. The $H_2Ti_2O_5$ nanotubes could be easily prepared via a hydrothermal method. Owing to the high rate capability, which is promoted by pseudocapacitive Li^+ intercalation mechanism, the electrode can be fully charged within minutes for thousands of times [76]. Layer-structured hydrogen titanate has been used as precursor for the preparation of TiO_2 with enhanced Li ion intercalation pseudocapacitance. Armstrong et al. [77]prepared titanate nanowires and adopted subsequent annealing to convert it to TiO_2-B nanowires. This TiO_2-B nanowires displayed an outstanding specific charge-storage capacity of 275 mAh g^{-1} and excellent rate capabilities for lithium intercalation via galvanostatic approaches, much greater than normal TiO_2-B electrode and nanostructured anatase [34].

Compared with protonated titanates, the alkali titanates (for example Na_2TiO_3) possess much better structural stability at elevated temperature [78]. In alkali titanates, the alkali ions exist in the interlayer space between the titanate layers. The Li ion can intercalate into Na_2TiO_{13} nanorods reversibly in the potential ranging between 1.5 and 1.0 V versus Li metal [79]. Zhang et al. [77] proved that the high rate charge/discharge capability of $Na_2Ti_3O_7$ was due to the pseudocapacitive contribution to the

electrochemical lithium storage. Thermal treatment of hydrogen titanate can result in the formation of various TiO_2 products, including anatase TiO_2 nanotubes and TiO_2-B nanowires.

Nanoscaled spinel $LiFeTiO_4$ are also found to exhibit certain degree of intercalation pseudocapacitive Li^+ storage behavior. The Li^+ intercalation into bulk spinel $LiFeTiO_4$ may result in the full Fe^{3+}/Fe^{2+} reductions at a flat plateau of about 2.3 V without changes in the lattice structure [80]. Thus, $LiFeTiO_4$ fulfilled the prerequisite for intercalation pseudocapacitance with excellent structural stability and minor lattice changes. Chen et al. [81] revealed that Li^+ storage proceeded with slight changes in lattice parameters, and Li^+ storage kinetics was not solid-state diffusion-limited. It is believed that the spinel host allows the low energy diffusion path for Li^+. The unoccupied crystallographic sites are available for accommodating guest Li^+. Furthermore, the high-rate Li^+ storage in $LiFeTiO_4$ does not need advanced nanoarchitectures of electrode materials.

3.1.1.2. Nb-based materials. The intercalation pseudocapacitive behavior of Nb_2O_5 was also well investigated. (Table 1) The electrochemical behavior of Nb_2O_5 was first investigated by Reichman and Bard et al. [82,83], they pointed out that Nb_2O_5 possessed lithium insertion capability and was electrochromic as well. These investigations resulted in deeper research of Nb_2O_5 as a LIB electrode and as an electrochromic window. Inserting lithium into Nb_2O_5 happens under 2 V (vs. Li/Li^+) and the incorporation of the material has been obtained in 2 V LIB with a lithium alloy as the negative electrode [84,85]. What is particularly interesting with Nb_2O_5 is that even sweep rates are slow and crystallite sizes are reasonably large (30–40 nm), only a small amount of the entire charge is contributed by diffusion processes with less than 20% at 5 mV s^{-1} [7]. Besides the thin film electrode, Come et al. [86] also demonstrated the 40-μm thick Nb_2O_5 electrodes did not have diffusion limitation for charging time up to 1 min. Thus, the intercalation pseudocapacitance observed with Nb_2O_5 is an inherent property of this material, which is owing to rapid Li^+ transport through the structure and reversible crystallographic changes. Kumagai et al. [87] investigated the lithium intercalation and deintercalation process in the Nb_2O_5 film and calculated the chemical diffusion coefficient of Li ion in the electrode. Brezesinski et al. [5] pointed out that mesoporous T-Nb_2O_5 films possessed large amounts of pseudocapacitive charge storage and much higher capacities than mesoporous amorphous films with the same initial composition of T-Nb_2O_5. This high capacity was partially derived from intercalation pseudocapacitance. The Li^+ intercalation behavior in T-Nb_2O_5 was also demonstrated by *operando* Raman spectroscopy [88]. The specific capacitance for the orthorhombic Nb_2O_5 reached 400 F g^{-1}. Orthorhombic and pseudo-hexagonal phases exhibited much higher specific capacitances than amorphous phase, implying that Faradaic reactions resulting in extra capacitive energy storage were in association with Li^+ insertion through preferred crystallographic pathways [7]. Charge storage stemmed from lithium-ions intercalation into Nb_2O_5 could be described as:

$$Nb_2O_5 + xLi^+ + xe^- \leftrightarrow Li_xNb_2O_5$$

in which the maximum capacity x is 2 [89]. The intercalation pseudocapacitive response of Nb_2O_5 was ascribed to surface-redox reactions, as well as rapid two-dimensional transport of Li^+ through the crystal structure, which triggered no phase changes in the electrochemical reaction.

Lubimtsev et al. [21] studied the mechanism for the intercalation pseudocapacitance of Nb_2O_5. A solid solution adsorbed at specific sites was formed by the intercalation of Li^+ in a network of quasi-2D NbO_x faces with x = (1.3, 1.67, or 2), which donated local electrons to its nearby atoms to reduce niobium. Compared with solid electrolytes with high performance, low diffusion barriers were exhibited by open channels in the structure, enabling the migration of ions between these sites (E_b ~ 0.28–0.44 eV). The high performance of Nb_2O_5 electrode can also be explained as various adsorption sites per unit cell featured by similar adsorption energies and local charge transfer leads to high capacity and energy density, while the interconnected open channels result in low-cost diffusion pathways with low cost between these sites for high power density.

Nb_2O_5 has a variety of crystal structures which demonstrate similar behavior of Li^+ capacitive intercalation, however, the unit cell that shows more ordered arrangement is likely to provide more Li^+ vacancies with lower diffusion barriers, thereby resulting in higher rate performance [90]. On other words, the inherent properties of the bulk crystal structure of Nb_2O_5 are conducive to the capacity and rate performance. It suggests the distinctive 'room-and-pillar' NbO_6/NbO_7 framework structure in T-Nb_2O_5 rendered lithium intercalation with stable host; bond valence sum mapping put the degenerate diffusion pathways in exposure in the sites (spaces) surrounding the oxygen pillars of this complex structure [91]. Augustyn et al. [6] studied the intercalation pseudocapacitance and high-rate behavior of T-Nb_2O_5. The kinetics of T-Nb_2O_5 are surface-controlled for charging time >60 s, and the kinetic are limited by linear diffusion for charging time <20s. That is, no diffusion limitations occurred in T-Nb_2O_5 when charging time is as fast as 1 min (60 C rate). In addition, the high-rate capability of T-Nb_2O_5 suggests that exceptionally fast ionic transport is permitted by the unique crystal structure.

Morphology also plays an important role in Li-ion intercalation pseudocapacitive performance of Nb_2O_5. Various synthesis methods have been exploited for the development of nanostructured Nb_2O_5 with different morphologic structure. Kong et al. [92] adopted a facile and sustainable method to fabricate T-Nb_2O_5 nanocrystals with novel nanorod-like cellulose nanocrystals as soft templates. The as-prepared T-Nb_2O_5 films exhibited typical capacitive behavior in the sweep rate ranging from 1 to 20 mV s^{-1}. It demonstrated an initial intercalation capacity of 644 C g^{-1} at 0.625 A g^{-1} current density. A Nb_2O_5 nanosheet with two-dimensional structure enabled the electrode to exhibit a specific capacity of 164 mAh g^{-1} and good rate capability. These nanosheets were perpendicular to (001) planes, which may enable lithium ion to transport via natural tunnels throughout the a–b plane, and thus favor fast intercalation/deintercalation reaction [93]. Cheong et al. [94] prepared mesoporous T-Nb_2O_5 nanofibers by electrospinning and calcination. It showed exceptionally long cycle retention (~160 mAh g^{-1} at 500 mA g^{-1} after 2000 cycles and ~88 mAh g^{-1} at 3000 mA g^{-1} after 5000 cycles), as well as better rate capability (~70 mAh g^{-1} at 5000 mA g^{-1}). Free-standing T-Nb_2O_5 nanowires electrodes are featured by 20~50 nm diameter and several micrometers long cross with each other and yield a three-dimensional (3D) porous network. The hybrid electrodes as designed can deliver a high gravimetric capacitance of 220 mAh g^{-1} at a 0.5 C current density [95]. T-Nb_2O_5 quantum dots were electrodeposited by Zhao et al. [96] on Ti nanorod arrays to fabricate Ti@T-Nb_2O_5 core-shell array electrodes, which showed no apparent decay after 500 cycles at a high rate current of 30 A g^{-1}. As shown in Fig. 8, three-dimensionally ordered macroporous (3DOM) microstructure of T-Nb_2O_5 presents three typical porous structures. Nanopores distributing in the interconnected walls supply excessive interstitial storage sites for Li^+. In addition, the 3DOM architecture is equivalent to a three dimensional electron conductive network in the process of charge/discharge and can favor electron and ion transport together with the reduced Li^+ diffusion lengths in the

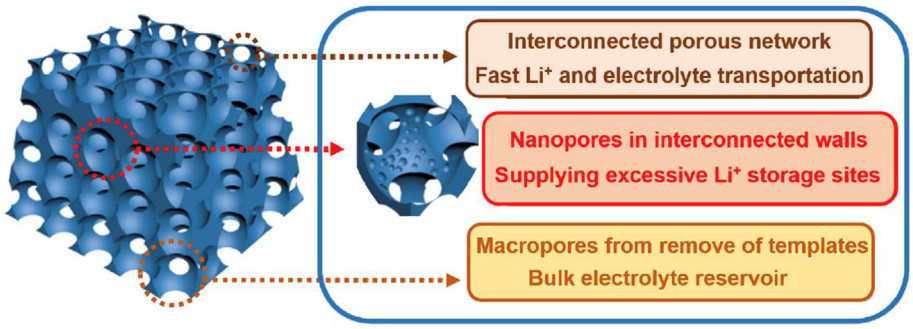

Fig. 8. Schematic representation of the T-Nb_2O_5 hierarchical structure, electrolyte molecule storage, and lithium-ion surface storage in the 3DOM T-Nb_2O_5. Reprinted with permission from a study by Lou et al. [97]. Copyright (2017) Elsevier Ltd.

electrode material [97]. The flower-like hierarchical Nb_2O_5 microspheres exhibit the reversible capacity of 191.42 mAh g^{-1} at 0.05 A g^{-1} and rate performance of 90 mAh g^{-1} at 5 A g^{-1} [98].

Doping strategy was also used to further improve the intercalation pseudocapacitance performance of Nb_2O_5. For example, Wang et al. [99] introduced titanium into the lattice of Nb_2O_5 to improve the electrochemical performance. The doped Ti was found to provide an additional redox reaction and decrease the resistance of charge transfer during the electrochemical reaction. Meanwhile, intercalation pseudocapacitance of Li^+ storage behavior was not affected by Ti doping. This property is definitely beneficial for high rate capability energy storage. In addition to doping, formation of composite was also tried. For example, heterogeneous TiO_2@Nb_2O_5 composites were prepared by Liu et al. [64] with even embedding of TiO_2 nanoparticles on ultrathin Nb_2O_5 nanosheets. The contact can be enhanced between the active material and the electrolyte owing to the large surface area of the composite. The buffering of TiO_2 nanoparticles aggregation can be achieved on Nb_2O_5 nanosheets surface; and a short diffusion pathway and greater surface storage sites for Li^+ ions can be offered by the embedding of TiO_2 nanoparticles on Nb_2O_5 nanosheets. The 3DOM $TiNb_2O_7$ consisting of interconnected single-crystalline nanoparticles enables Li^+ to insert/extract facilely and electrons to transfer fast, yielding high performance lithium ion pseudocapacitive behavior and thus good electrochemical performance [100]. By doping of K and F, Cao et al. [101] introduced a small fraction of tetragonal tungsten bronze related $KNb_6O_{15}F$ as conductive wires into H-Nb_2O_5. The rate performance is exceptional with reversible capacities of 120, 100, and 80 mAh g^{-1} at 5 C, 10 C, and 20 C, respectively.

Considering the low electronic conductivity of oxides, which may cause a block for electron charge transfer during electrode reaction, the formation of metal oxide and carbonaceous hybrid electrodes always show higher energy and power density than corresponding original pure oxide electrodes. Compositing Nb_2O_5 with carbonaceous materials was also tried recently towards improving the intercalation pseudocapacitance. For example, Lim et al. [102] developed a mesoporous Nb_2O_5/carbon electrode as the anode in the hybrid SC. The mechanism of charge and storage in the electrode was on the basis of a Faradaic pseudocapacitive reaction at the anode. It exhibited an energy density of 74 W h kg^{-1} and power density of 18,510 W kg^{-1}. Cai et al. [103] synthesized the Nb_2O_5/carbon electrode by oleylamine-assisted hydrothermal. This nanostructured electrode delivered about 298 mA h g^{-1} after 200 cycles at 100 mA g^{-1} in battery testing. This is most likely due to the improvement of electric conductivity by carbon component, the use of active materials and perhaps the structural stability as well upon cycling. Lim et al. [104]developed a similar Nb_2O_5/carbon hybrid electrode with core-shell structure. Keeping microemulsion parameters in good control can achieve the ideal synthesis of T-Nb_2O_5 for rapid Li^+ diffusion. The excellent rate capability of this electrode was mainly due to the synergistic effect of high electrochemical performance of Nb_2O_5 and electron mobility in the conductive carbon shell. Kong et al. [105] prepared free-standing T-Nb_2O_5/graphene composite papers for Li-intercalating pseudocapacitive process. Such an electrode delivered a gravimetric capacitance of 620.5 F g^{-1} because T-Nb_2O_5/graphene composite papers after thermal treatment demonstrated a nanoporous layer−stacked structure featured by excellent ionic/electric conductive pathways. This result implies that the intrinsic capacitive behavior could be improved by anchoring Nb_2O_5 nanoparticles onto conductive graphene sheets, which may be achieved via the synergetic efforts of intercalation pseudocapacitance from small Nb_2O_5 nanoparticles and electric double-layer capacitance from graphene sheets. Kong et al. [90] investigated a variety of crystalline phases of Nb_2O_5 anchored on graphene substrate during Li^+ intercalation process. Compared with T- and TT-phases, M − and H-phase obtained higher capacity-retention. Higher Li^+ diffusion coefficients (D_{Li}) of 1.6×10^{-12} cm^2 s^{-1} leads high rate performance of H-phase, which is nearly two order of magnitude greater than TT-phase of 4.7×10^{-14} cm^2 s^{-1}. The T-Nb_2O_5 nanocrystals offer favorable accessibility of the electrolyte and rapid ion diffusion, resulting in high intercalation pseudocapacitance. Meanwhile, rGO networks increase the electrical conductivity throughout the electrode and provide fast transport pathways for electron mobility, thus improving the use of active materials [106]. Wang et al. [107] coated Nb_2O_5 by a thin amorphous carbon layer and the composite delivered a discharge capacity of 396 mA h g^{-1} after 100 cycles at 100 mA g^{-1}current density, which was rather higher than bare Nb_2O_5 nanosheets. Nb_2O_5 primary particles with tens of nanometers were in uniform coating with thin amorphous carbon layers. The amorphous carbon layer had vital roles such as providing electronic network and suppressing the morphological changes in particles [108]. Luo et al. [109] prepared the T-Nb_2O_5/CNTs composite by a simple template-free method, which showed great storage ability for Li^+ with typical intercalation capacitive behavior. CNTs with good dispersion in Nb_2O_5 can obviously decrease the limitation from diffusion process and enhance the capability of high rate charge and discharge. Wang et al. [110] reported an electrode material on the basis of Nb_2O_5 nanocrystals in situ formed on CNTs with a distinctive structure, which demonstrated exceptionally enhanced energy density of 50 W h kg^{-1} with a power of 86.46 W kg^{-1}. T-Nb_2O_5 nanowires featured by ultrathin carbon coating exhibited stable high rate capability of Li^+ storage [111]. The introduction of carbide-derived carbon into Nb_2O_5 leads to the formation of amorphous Nb_2O_5 particles on the carbon framework. This electrode showed reversible Li^+ intercalation/deintercalation [112], which was in agreement with the properties of similar electrodes prepared by a hydrothermal method [113]. Nb_2O_5

nanoparticles with support of three-dimensional porous carbon nanowebs exhibited a high reversible capacity of ~125 mA h g^{-1}, and fast Li-ion storage kinetics [114]. Doping Zr into Nb-based oxides leads to a one-dimensional hierarchically porous $ZrNb_{24}O_{62}$ nanowires, which have an ultralarge Li^+ ion diffusion coefficient as a new intercalating pseudocapacitive material for boosting Li^+ ion storage and clearly surpass those of corresponding $TiNb_{24}O_{62}$ materials [115].

Kong et al. [116] compared the intercalation pseudocapacitive behaviors of Nb_2O_5 loaded on various carbon substrates. These materials with different nanoarchitecture are composed of small nanocrystals with highly exposed active surfaces, and they all show excellent Li^+ intercalation pseudocapacitive characteristics. In addition, the 3D urchin-like shell structure assembled by multiple nanorods can enhance the nanocrystals utilization degree and increase the electrode kinetics. It was reported that a hierarchically hybrid material with T-Nb_2O_5 nanoparticles was in uniform support on the surface of Nb_2CT_x sheets featured by disordered carbon. However, a surface-controlled process plays a dominant role in the charge-storage kinetics [117]. Three synergistic influences could be used to explain the outstanding electrochemical performance: (1) the excellent conductivity of the interior, $Nb_4C_3T_x$ layers without oxidation, (2) the rapid rate response and great capacity of the exterior Nb_2O_5 nanoparticles, and (3) the electron 'bridge' influences of the disordered carbon [118].

3.1.1.3. Vanadium-based electrodes. Vanadium pentoxide, V_2O_5, has been in widespread investigations for a variety of applications. V_2O_5, as an intercalation compound, has aroused great attentions in the application of electrode for electrochemical pseudocapacitor. (Table 1) It was reported that Li^+ ion intercalated reversibly into V_2O_5 followed by the intercalation reaction:

$$V_2O_5 + xLi^+ + xe^- \leftrightarrow Li_xV_2O_5$$

The level of intercalation seems to be dependent upon multiple factors including the morphology of the material, the presence of V^{4+} and such experimental considerations as electrolyte and discharge rate. McNulty et al. demonstrated that intercalation-based processes were not the only cause of the total charge storage of V_2O_5 but also capacitive processes. Intercalation mode reactions would transit to capacitive charge storage at slower scan rates in various potential ranges with respect to nanoscale and bulk vanadium oxide materials. When scan rates are higher, both intercalation and diffusion-based reaction processes are present at electrode materials on bulk or nanoscale level even multivalent surface chemistry are obviously different [119]. Owing to the small size of Li^+, the differences between various V_2O_5 polymorphs are relatively small and the structural distortions induced upon Li^+ intercalation is slight [120]. Takahashi et al. [121] prepared a single-crystal V_2O_5 nanorod arrays with a length of approximately 10 μm and diameters from 100 to 200 nm. Such structure greatly facilitate Li^+ to intercalation and deintercalation because the reactions of surface oxidation and reduction happen along nanorods side surface and the solid-state diffusion distance is very small. Li et al. [122] demonstrated the intercalation pseudocapacitance occurred in the porous V_2O_5 electrode in the electrolyte of LiCl. It can reach the specific capacitance of 606 F g^{-1} at high current rate of 500 mV s^{-1}. The microstructure and nanostructure of V_2O_5 effectively enhanced Li^+ intercalation capacities and pseudocapacitance, which promoted rate capabilities and cyclic stability. Enlarging surface area can prevent irreversible phase transition and result in substantial enhancement of cycling stability, storage capacity, and electrochemical kinetics [123]. In the microstructured/nanostructured V_2O_5, the surface pseudocapacitive storage played a dominant role in the total storage capacity when scan rates are higher, whereas the bulk Li^+ storage dominated at the lower scan rate [123]. The intercalation pseudocapacitance of V_2O_5 is also obtained in a gel electrolyte. The enhanced pseudocapacitance could be due to higher lithium ion concentration in the gel electrolyte, which facilitates lithium ion diffusion and absorption [124]. The 3D structure of V_2O_5 can overcome slow ion insertion/deintercalation by diffusion of Li^+ through the V_2O_5 bulk. It exhibited a specific capacitance of 155 F g^{-1} and showed an obvious electrochromic color transfer from green/gray to yellow, demonstrating the charge condition of the capacitor [125]. Yang et al. [126] synthesized a hollow V_2O_5 spheres (Fig. 9) featured by a remarkable pseudocapacitance effect with 479 F g^{-1} capacitance at 5 mV s^{-1} in the application of SC electrodes in a solution of 5 M $LiNO_3$. The PPy coating on V_2O_5 particles surface can effectively reduce the direct contact of active materials and electrolyte, and thus stabilize the phase transformation. Rauda et al. [127] prepared V_2O_5 thin films by atomic layer deposition (ALD) with two thicknesses. For 2-nm vanadia samples, its internal specific surface area is characterized with full accessibility; whereas for the 7-nm vanadia, electrolyte diffusion is limited by a few pore blockage. However, high levels of pseudocapacitance are exhibited by both thick and thin vanadia layers, implying that Li^+ diffuse rapidly through vanadia of even 7 nm thick. Armstrong et al. [128] compared the bulk V_2O_5 and inverse opal structured V_2O_5 and found that the latter electrode maintained a dominant intercalation-mode response, even at higher scan rates. High rate performance was exhibited by the 3DOM vanadium oxide film with 355 F g^{-1} at 0.5 A g^{-1} and 125 F g^{-1} at 15 A g^{-1}, respectively. The 3DOM nanostructure enhanced pseudocapacitive influence and diffusion coefficient of Li ion and also resulted in high rate capability of vanadia [129]. Aerogels are composed of a three-dimensional network of nanometer-sized solid particles surrounded by a continuous macroporous and mesoporous volume. The V_2O_5 aerogels also showed pseudocapacitive behavior rather than double-layer capacitive behavior [130]. The large surface area, short diffusion paths, nanodimensional solid phase, and interconnected mesoporosity of V_2O_5 aerogels play a significant role in pseudocapacitive charge-storage mechanism. The addition of a Faradaic pseudocapacitance to the traditional ion intercalation process would seem to explain the enhanced electrochemical properties observed for V_2O_5 aerogels [131].

As reported previously, Li^+-ion intercalation into V_2O_5 is intrinsically slow, with a reported diffusion coefficient of the order of 10^{-13} cm^2 s^{-1} [132]. Short Li^+ ions diffusion time in the intercalation material can improve the high rate performance of Li^+ ion intercalation materials. Because Li^+ ion diffusivity is an inherent characteristic of the guest-host species couple, decreasing Li^+ ion diffusion path, i.e., reducing the thickness of intercalation material, has been regarded as the most rational method to enhance the specific power of Li^+-ion intercalation materials. Based on this, composite electrodes of V_2O_5 thin layer on conductive materials, such as metal fibers or carbonaceous materials, have aroused great attentions in recent years in the application of high rate intercalation electrodes for pseudocapacitor. The electrodeposition of V_2O_5 was obtained on a CNT film substrate featured by a three-dimensional porous structure at the nanometer scale. The maximum specific energy of 851 Wh kg^{-1} and specific power of 125 kW kg^{-1} were achieved from the discharging curves of this electrode [133]. Perera et al. [134] developed a facile approach to prepare freestanding hybrid electrode of V_2O_5 nanowire and CNT paper electrodes with no binders. This paper electrode demonstrated a power density of 5.26 kW kg^{-1} and an energy density of 46.3 Wh Kg^{-1}. The unique property of the V_2O_5/CNT electrode offers Li^+ ions with short diffusion path and enables facile access to vanadium redox centers in addition to the high conductivity of CNTs. Not only high power density but also high-energy density is

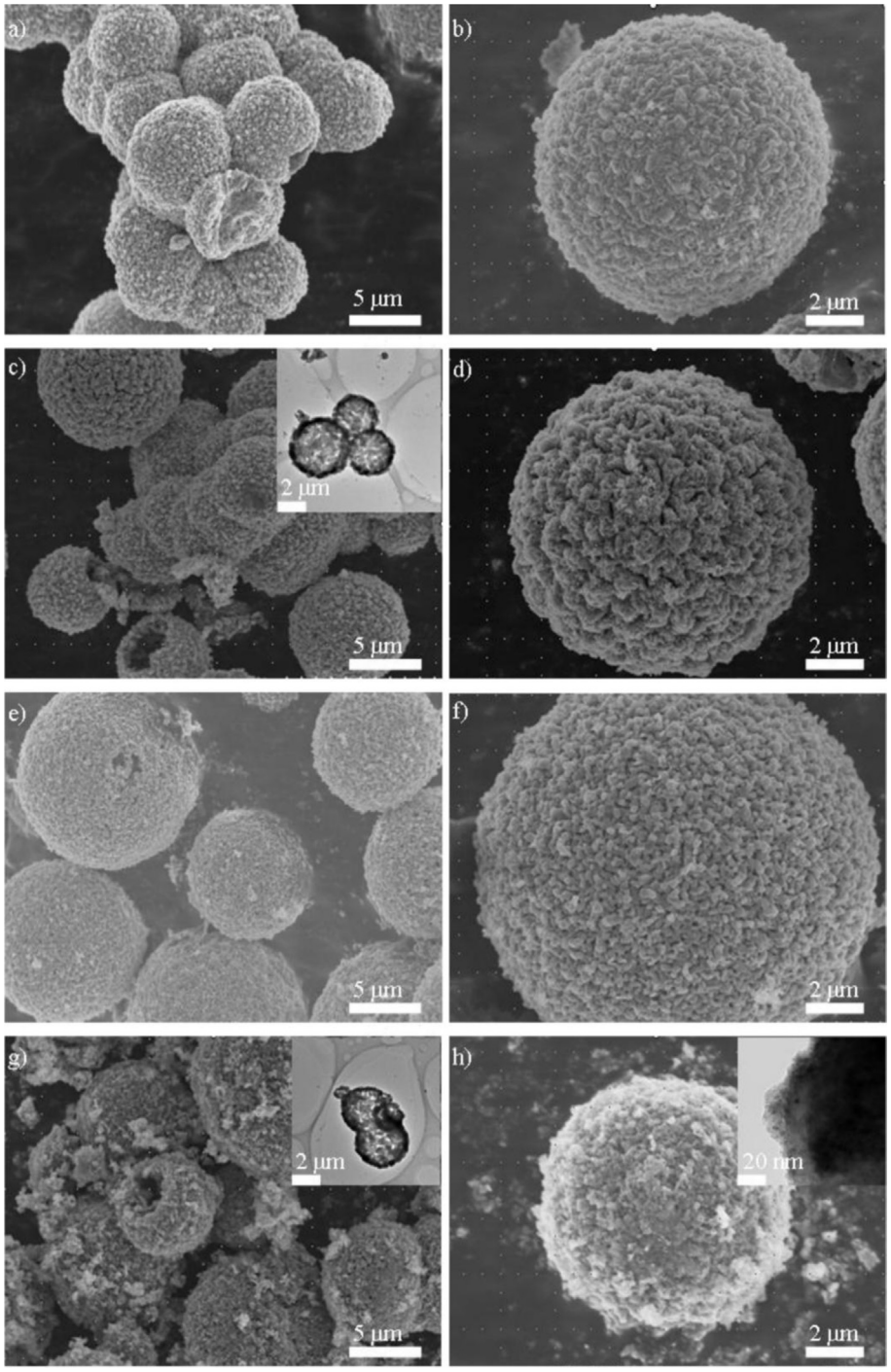

Fig. 9. SEM images of V_2O_5 synthesized at different temperatures. Reprinted with permission from a study by Yang et al. [126]. Copyright (2013) Elsevier Ltd.

exhibited by the composite architecture, emphasizing the advantages of applying carbon substrates to fabricate high performance SC electrodes [135]. Zhang et al. [136] prepared 2D V_2O_5 nanosheets on the CNT substrate with large interlayer distance. The high conductivity of CNTs improved the reversible phase transition reactions of V_2O_5, enhanced the ion diffusion kinetics, maintained the electrode's mechanical integrity and provided electron transport pathways. The total capacity was primarily contributed by the surface pseudocapacitance. Under hydrothermal conditions, flower-like vanadium oxide nanostructures nucleate on carbon onion nanoparticles to generate a highly intertwined network. $P2_1/c$ VO_2, applied as a lithium intercalation electrode, shows capacitor-like (pseudocapacitive) lithium intercalation [137]. ALD enabled the orthorhombic V_2O_5 to deposit on the mesoporous carbon substrate. It was found that lithium intercalation was pseudocapacitive predominantly and its maximum capacities were 200 mAh g^{-1} [138]. Ren et al. [139] reported the synthesis of VO_2 nanobelt on the basis of forest structure via a solvothermal method with graphene network as the underlying support. This composite has stable discharge capacity of 178 mA h g^{-1} at a current density of 10 A g^{-1}

and 100 mA h g^{-1} at 27 A g^{-1}. The graphene substrate may provide a much larger surface area and denser nucleation sites for better active mass loading.

Typical characteristics of pseudocapacitive behavior are shown by CoV_2O_6 nanosheets, including currents which are mostly in linear dependence on sweep rate, as well as redox peaks whose potentials do not show a significance shift with sweep rate. This behavior is stimulated by the rapid Faradaic charge transfer kinetics at the interface and result in the improved kinetics which could be achieved owing to the relative absence of diffusion [140]. However, some other V-based materials exhibited the intercalation pseudocapacitance in bulk. Heli et al. [141] prepared LiV_3O_8 nanosheets by a citrate sol-gel combustion route. There is no phase transformation during the process of intercalation/deintercalation, which is under control of lithium-ion diffusion in the bulk material. Therefore, the pseudocapacitance induced by Li^+ intercalation in LiV_3O_8 would not induce any phase transformation. Li_3VO_4 featured by low insertion voltage of Li^+ ion and rapid kinetics could be favorably applied for lithium-ion capacitors. After the introduction of N-doped carbon into Li_3VO_4, the electrode exhibited a high-rate pseudocapacitive behavior, which presented a high energy density of 136.4 Wh kg^{-1} at a power density of 532 W kg^{-1} [142]. $Na_{0.33}V_2O_5$ nanowires are tested, and exhibits an outstanding specific capacitance of 498 F g^{-1} at 0.4 A g^{-1} current density. The performance is primarily attributed to the redox pseudocapacitance and intercalation pseudocapacitance resulting from the layered structure, high electrical conductivity, and excellent adhesion between the nanowires and the current collector [143]. Based on DFT calculation, the V_2C monolayer could exhibit faster transport and higher charge and discharge rates for Li, which may supply an intercalation pseudocapacitance [144]. Zhu et al. [145] demonstrated that the charge-storage process was dominated by pseudocapacitance in $VOPO_4$ nanosheets, resulting in exceptional rate capability and lasting stability. Capacity decay was not suffered by exfoliated $VOPO_4$ nanosheets and they have rather greater rate capability than bulk counterpart in LIB. Joseph et al. [146] investigated the influence of crystallite size on the intercalation pseudocapacitance of $LiNiVO_4$ in 1-M LiOH electrolyte solution. The intercalation pseudocapacitance for the $LiNiVO_4$ nanostructure was larger than that of the $LiNiVO_4$ microstructure.

3.1.1.4. Mo-based materials. As a two-dimensional (2D) layered material with electroactivity, MoO_3 can accommodate 1.5 Li per Mo. It consists of alternately stacked layers which are combined together by weak van der Waals forces along [010]. Li^+ insertion can be achieved by the interlayer gaps; however, few interests have been given to MoO_3 in the applications of battery owing to moderate reaction kinetics and bad cycling behavior. (Table 1) Wang et al. [36] demonstrated that mesoporous MoO_3 with layered structure had Li^+ intercalation pseudocapacitance and high charge storage. The electrochemical Li^+ insertion process is represented as follows:

$$MoO_3 + xLi^+ + xe^- \leftrightarrow Li_xMoO_3$$

In the CV curves, the cathodic peak of approximately 2.7 V versus Li/Li^+ could be arisen from an irreversible phase transition between MoO_3 and $Li_{0.25}MoO_3$. Brezesinski et al. [147] stated that mesoporous α-MoO_3 is featured by iso-oriented layered nanocrystalline grains that facilitates intercalation pseudocapacitance to happen on the same timescale as redox pseudocapacitance. The pseudocapacitive behavior of α-MoO_3 is highly depended on the particle size of materials. The bulk α-MoO_3 materials possess a phase transformation during the Li^+ intercalation process [37,42]. Compared with the crystalline MoO_3, the amorphous structure can offer redox pseudocapacitance with surface sites but does not have abundant order to make Li^+ access to the region below the surface. However, Li^+ intercalates into the interlayer gap and implements charge transfer reactions in crystalline MoO_3 [147]. Guan et al. [148] compared the effects of amorphous and crystalline MoO_3 on the mechanism of Li storage. Liu et al. [149] prepared MoO_3 film and studied its electrochemical properties. Crystalline α-MoO_3 is better than amorphous MoO_3 in terms of intercalation pseudocapacitance. The film electrode combined surface-redox pseudocapacitance and Li^+ intercalation pseudocapacitance. It showed 65 F g^{-1} capacitance at 5 mV s^{-1} [149]. Jiang et al. [150] used a simple hydrothermal approach to prepare α-MoO_3 nanobelts (Fig. 10). α-MoO_3 nanobelts have much higher maximum specific capacitance than MoO_3 nanoplates with 280 F g^{-1}. The unique structure of nanobelts revealed more active crystallographic (010) planes, in favor of Li^+ intercalated MoO_3. Based on the experiment and DFT calculation, Kim et al. [151] found that introducing oxygen vacancies results in a larger interlayer spacing which stimulate more rapid charge-storage kinetics and makes the α-MoO_3 structure be able to be retained during Li ions intercalation/deintercalation. The high specific capacity of α-MoO_3 with higher oxygen vacancies concentration were resulted from enhanced Mo^{4+} formation after lithiation, a process which happens reversibly with no

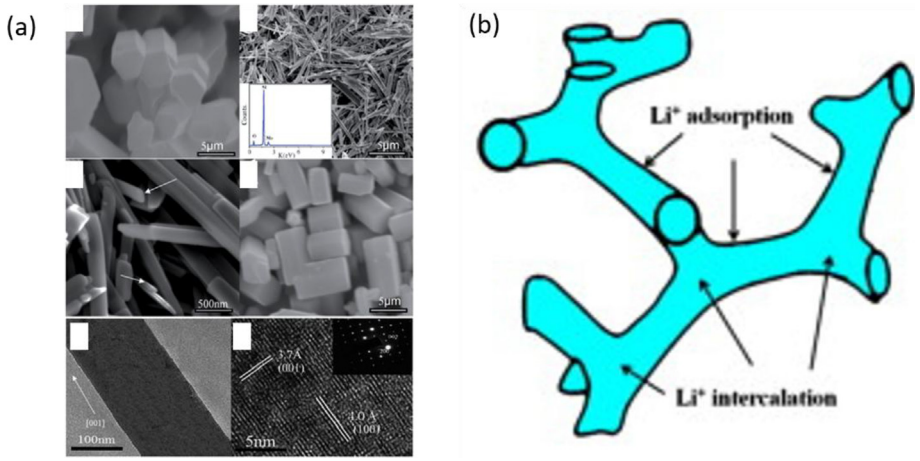

Fig. 10. (a) SEM and TEM images of α-MoO_3 nanobelt. (b) Schematic illustration of the charge storage of m-MoO_2 including intercalation and adsorption of Li^+. Reprinted with permission from a study by Jiang et al. [150] and Li et al. [157]. Copyright (2013) The Royal Society of Chemistry; Copyright (2013) Elsevier B·V.

development of the monoclinic MoO_2. Chen et al. [152] prepared a MoO_3-Mo wires with well-aligned laminated structure, which will benefit Li^+ ion intercalation.

Sanchez et al. [153] reported that similar charge storage at the same time scales has been achieved with α-MoO_3 nanobelts/SWNTs without any iso-orientation. They further reported that the diffusion-controlled ion intercalation contribution in nano α-MoO_3 belts/SWNTs was more than that of templated mesoporous α-MoO_3. Xiao et al. fabricated a freestanding α-MoO_3 nanobelts/CNT with a specific capacitance of 337 F g^{-1}. Higher electronic conductivity of MoO_{3-x} enhances intercalation kinetics and intercalation pseudocapacitance, which leads to greater and faster intercalations [154]. Shakir et al. [155] synthesized MoO_3 nanowires/MWCNTs composite and the specific capacitance was 210 F g^{-1}. MoO_3/MWCNT composite electrode was successfully fabricated by magnetron sputtering with specific capacitance of 93 F g^{-1} [156].

Furthermore, the m-MoO_2 material, the small couple of redox peaks in CV curve can be attributed to the intercalation and deintercalation of Li^+ into/from the tunnel structure of MoO_2. The schematic is presented in Fig. 10b to illustrate the adsorption and intercalation pseudocapacitance of m-MoO_2 [157]. The nanoscaled MoO_2 shows pseudocapacitive behavior and obtains exceptionally faster energy storage kinetics than corresponding bulk material. Such electrochemical behavior depends on the size. However, 15-nm nanocrystals of MoO_2 show a reversible transition from monoclinic to orthorhombic phase during lithium intercalation/deintercalation [158]. Petnikota et al. [159] used graphene oxide to reduce MoO_3 to MoO_2 and supported the final electrode. The Li^+ ion intercalation happened at higher current rate during the charge/discharge is due to differences in reaction kinetics and Li^+ diffusion coefficient. Hercule et al. [160] fabricated a nanorods-nanoflakes $Li_2Co_2(MoO_4)_3$ and demonstrated its intercalation pseudocapacitive behavior in LiOH electrolyte. MoS_2 was seriously considered as an intercalation host electrode for LIB [161]. Recently, M. Chhowalla et al. [162] reported that after exfoliation into nanosheets and subsequent restacking, layered molybdenum sulfides also demonstrated intercalation pseudocapacitance. Kinetic analysis indicates that almost all of the charge storage in MoS_2 is capacitive throughout the entire voltage range measured. The capacity must come from surface-redox processes combined with intercalation over short diffusion path lengths (intercalation pseudocapacitance) [163]. Yoo et al. [164] reported a capacitance of exfoliated-restacked MoS_2 of 250 F g^{-1} in an organic Li^+ ion containing electrolyte. The extremely rapid kinetics leads to the intercalation pseudocapacitance, which is because ionic and electronic transport is enhanced by the slightly expanded layer structure and the metallic 1T-phase. Cook et al. [165] demonstrated that over 80% of the charge storage in these MoS_2 nanocrystals was pseudocapacitance for the thick electrode. Wang et al. [166] introduced graphene into MoS_2 to expand the interlayer distance to increase atomic interface contact/interaction. MoS_2 modified by this interlayer is proved to have predominant pseudocapacitive properties.

3.1.1.5. Mn-based materials. Nanostructured manganese dioxide has the advantages of high surface area, high specific capacitance, wide charge/discharge potential range, rich resource, low cost, and environmental compatibility. In accordance with the previous reports (Table 1), the pseudocapacitance of the MnO_2 electrode in aqueous electrolytes appears to be associated with the ion intercalation/deintercalation reaction in MnO_2 [167,168]. To crystallize MnO_2, the mechanism involving Li^+ intercalation/deintercalation reaction is as follows:

$$MnO_2 + Li^+ + e^- \leftrightarrow MnOOLi$$

Based on the electrochemical testing of MnO_2, the results suggested a typical pseudocapacitive characteristic which was associated with cation intercalation/deintercalation reaction [169]. Xiong et al. [170] investigated the intercalation/deintercalation behavior of Li^+ in 2D layered MnO_2 with a variety of interlayer distances. MnO_2 dried by freeze with exfoliated nanosheets restacked with the greatest interlayer spacing and a less compact 3D network showed the highest rate capability and a stable cyclability beyond 5000 cycles. The Li-birnessite type MnO_2 thin films were studied in Li-based electrolyte. It displayed a typical intercalation pseudocapacitive behavior which appeared in the Na^+-based electrolyte [171]. Misnon et al. [172] studied the influence of ion size in the electrolyte on the specific capacitance of MnO_2 nanoflower electrode. The Li^+-contained electrolyte had the best performance. Thus, the use of smaller cations results in slightly larger specific capacitances [173]. Liu et al. [174–176] modified MnO_2 nanosheet by Co_3O_4. The nanosheet edges in entire exposure could also be conducive to the rapid intercalation of Li^+ into the layered structure, thereby improving the electrochemical kinetics. This hybrid electrode has a capacitance of 480 F g^{-1}, greater than pure MnO_2 conducting matrix compound electrodes. Au-modified MnO_2 exhibits true hybrid energy storage, including surface-redox pseudocapacitance and intercalation pseudocapacitance. A capacity of 1010 F g^{-1} can be obtained for the electrode with a MnO_2 shell thickness of 74 nm [177]. Wang et al. [178] fabricated a nanostructured MnO_2/CNT composite electrode which exhibited a pseudocapacitive behavior accompanied by Li^+ intercalation/deintercalation reaction. Javed et al [179]. synthesized MnS nanoparticles on conductive carbon and found that the diffusion-controlled process dominated the total capacitance, which was due to the Li^+-intercalation process. It exhibited excellent capacitance of 710.6 F g^{-1} at 1 mV s^{-1} in aqueous electrolyte.

3.1.1.6. Other materials. Some other compounds also exhibit the behavior of intercalation pseudocapacitance, but they were not received extensive investigations in terms of the application as intercalation pseudocapacitive electrodes. (Table 1) The Li^+ intercalation/deintercalation in the $LiNi_{0.5}Mn_{1.5}O_4$ solid induced the pseudocapacitance [180]. The charge storage of $LiNi_{0.8}Co_{0.2}O_2$ was demonstrated to mainly come from the pseudocapacitance effect of the intercalation/deintercalation of Li^+ during charge/discharge processes, which had a capacitance of approximately 270 F g^{-1} [181]. $Li_2Co_2(MoO_4)_3$ undergoes pseudocapacitance mechanism through redox reaction and ion intercalation in the bulk material as the BET surface area is relatively low. The high performance demonstrated by the Li-based electrolyte was ascribed to the small size of lithium ion, which was easily intercalated into the inner of the crystal structure [160]. The rapid Li^+ intercalation pseudocapacitance was firstly observed in an amorphous material of $FePO_4$ thin film, which obtained specific powers above 1 MW kg^{-1} [182]. The nano-$LiFePO_4$ exhibited the pseudocapacitive behavior in a very small potential range [183]. Kisu et al. [184] investigated the different reaction mechanisms in the crystalline $LiFePO_4$ and amorphous phase. Li^+ diffusion controlled the crystalline phase, and amorphous phase demonstrated a rapid, surface-controlled, and pseudocapacitive charge-storage mechanism. Li et al. [185] found that charges were stored by nanostructured Fe_3O_4 not only on the surface/near-surface like typical pseudocapacitive materials, but also via Li^+ intercalation in the bulk. Metallic oxide ZnO is regarded as a promising alternative anode material in the application of lithium ion battery owing to its excellent theoretical capacities of 978 mA h g^{-1}. ZnO/ZnO@C composites presented a

Table 1
Summary of electrode materials with Li ion intercalation pseudocapacitance.

Electrode materials	Synthesis method	Electrolyte	Capacity or capacitance	Potential range	Reference
TiO_2 nanotubes	Hydrothermal reaction	1 M $LiPF_6$ in EC/DMC	314.4 mAh g^{-1}	1–2.5 V	[35]
TiO_2 nanoparticle	Wet chemistry	N/A	130 μF cm^{-2}	1.5–3.5 V	[36]
Anatase TiO_2	Wet chemistry	1 M $LiClO_4$ in PC	120 μF cm^{-2}	1.5–3 V	[38]
TiO_2 nanomembrane	Spin-coating	1 M $LiPF_6$ in EC/DMC	200 mAh g^{-1}	1–3 V	[39]
TiO_2-B nanobelts	Microwave irradiation	1 M $LiPF_6$ in EC/DMC	240 mAh g^{-1}	1–−2.5 V	[45]
TiO_2-B nanosheets	Hydrothermal reaction	1 M $LiPF_6$ in EC/DMC	186.6 mAh g^{-1}	1–3 V	[46]
TiO_2-B nanowires	Hydrothermal reaction	1 M $LiPF_6$ in EC/DMC	242 mAh g^{-1}	1–3 V	[47]
Anatase TiO_2	Batch method	1 M $LiPF_6$ in EC/DMC/DEC	168 mAh g^{-1}	1–3 V	[50]
TiO_2 nanosheets	Wet chemistry	1 M $LiPF_6$ in EC/DEC	311 mAh g^{-1}	1–3 V	[51]
TiO_2 nanotubes	Hydrothermal reaction	1 M $LiPF_6$ in EC/DEC	163 mAh g^{-1}	1–3 V	[52]
Anatase TiO_2	Wet chemistry	1 M $LiPF_6$ in EC/DMC	302 mAh g^{-1}	1–3 V	[53]
Nanotubular TiO_2	Anodic oxidation technique	1 M LiCl	200 F g^{-1}	0–1 V	[55]
TiO_2/CNTs	Wet chemistry	1 M $LiPF_6$ in EC/DMC	470 mAh g^{-1}	1.5–2.2 V	[57]
TiO_2/N-doped graphene	Ball milling	1 M $LiPF_6$ in EC/DMC	182.7 mAh g^{-1}	1–2.5 V	[59]
TiO_2/N-doped carbon	Wet chemistry	1 M $LiPF_6$ in EC/DMC	180 mAh g^{-1}	1–3 V	[60]
Nb-doped TiO_2	Electrospinning	1 M $LiPF_6$ in EC/DMC/PC	142 mAh g^{-1}	1.2–2.3 V	[62]
Nb-doped TiO_2	Wet chemistry	1 M $LiPF_6$ in EC/DMC	148 mAh g^{-1}	1.2–2.5 V	[63]
TiO_2/Nb_2O_5	Hydrothermal reaction	1 M $LiPF_6$ in EC/DMC/DEC	166.3 mAh g^{-1}	1–3 V	[64]
TiN/TiO_2 nanowire	Hydrothermal reaction	1 M $LiPF_6$ in EC/DEC	244 mAh g^{-1}	1–3 V	[67]
TiS_2 nanocrystal	Wet chemistry	1 M $LiClO_4$ in PC	167 mAh g^{-1}	1.5–3 V	[70]
$H_2Ti_6O_{13}$-nanowires	Hydrothermal reaction	1 M $LiPF_6$ in EC/DEC	828 F g^{-1}	1–3 V	[72]
$H_{1.1}Na_{0.9}Ti_3O_7$	Hydrothermal flow synthesis	1 M $LiPF_6$ in EC/DMC/DEC	150 mAh g^{-1}	0.01–2.5 V	[74]
$H_2Ti_2O_5$	Hydrothermal reaction	1 M $LiPF_6$ in EC/DMC	228 mAh g^{-1}	1–2.5 V	[76]
$Na_2Ti_6O_{13}$	Wet chemistry	1 M $LiPF_6$ in EC/DMC	150 mAh g^{-1}	1–2 V	[79]
$LiFeTiO_4$	Sol–gel method	1 M $LiPF_6$ in EC/DMC	250 mAh g^{-1}	1.5–4.8 V	[81]
Nb_2O_5	Wet chemistry	1 M $LiClO_4$ in PC	200 mAh g^{-1}	1–2.5 V	[87]
T-Nb_2O_5	Wet chemistry	1 M $LiClO_4$ in PC	130 mAh g^{-1}	1.2–3 V	[6]
T-Nb_2O_5 nanocrystals	Acid-catalyzed hydrolysis	1 M $LiPF_6$ in EC/DMC/EMC	644 C g^{-1}	1.2–3 V	[92]
Nb_2O_5 nanosheets	Hydrothermal reaction	1 M $LiPF_6$ in EC/DMC/DEC	184 mAh g^{-1}	1–2.6 V	[93]
T-Nb_2O_5 nanofibers	Electrospinning	1 M $LiPF_6$ in EC/DEC	160 mAh g^{-1}	1–2.6 V	[94]
T-Nb_2O_5 nanowires/carbon cloth	Hydrothermal reaction	1 M $LiPF_6$ in EC/DEC	182 mAh g^{-1}	1–3 V	[95]
T-Nb_2O_5 quantum dots	Electrodeposition	1 M $LiPF_6$ in EC/DEC	350 mAh g^{-1}	1–3 V	[96]
3D T-Nb_2O_5	Polymerization technology	1 M $LiPF_6$ in EC/DMC	106 mAh g^{-1}	1–3 V	[97]
Nb_2O_5 microspheres	Hydrothermal reaction	1 M $LiPF_6$ in EC/DEC	191.42 mAh g^{-1}	1–3 V	[98]
Ti-doped Nb_2O_5	Hydrothermal reaction	1 M $LiClO_4$ in PC	650 F g^{-1}	3–4 V	[99]
$TiNb_2O_7$	Polymerization technology	1 M $LiPF_6$ in EC/DMC	135 mAh g^{-1}	1–3 V	[100]
Nb_2O_5/carbon	Wet chemistry	1 M $LiPF_6$ in EC/DMC	115.1 mAh g^{-1}	1.1–3 V	[102]
NbO_x/carbon	Hydrothermal reaction	1 M $LiPF_6$ in EC/DMC/DEC	298 mAh g^{-1}	0.01–3 V	[103]
Nb_2O_5/carbon	Wet chemistry	1 M $LiPF_6$ in EC/DMC	180 mAh g^{-1}	1–3.5 V	[104]
T-Nb_2O_5/graphene	Solvothermal reaction	1 M $LiPF_6$ in EC/DMC/EMC	620.5 F g^{-1}	1–3 V	[105]
T-Nb_2O_5/graphene	Hydrothermal reaction	1 M $LiPF_6$ in EC/DMC	110 F g^{-1}	3–4.5 V	[106]
Nb_2O_5@C nanosheets	Hydrothermal reaction	1 M $LiPF_6$ in EC/DMC/EMC	396 mAh g^{-1}	0.01–3 V	[107]
Nb_2O_5/CNTs	Wet chemistry	1 M $LiPF_6$ in EC/DMC	180 mAh g^{-1}	1–3 V	[109]
Nb_2O_5/carbon nanoweb	Wet chemistry	1 M $LiClO_4$ in PC	125 mAh g^{-1}	1.2–2.2 V	[114]
V_2O_5	Electrodeposition	12 M LiCl	606 F g^{-1}	−0.2–−0.8 V	[122]
V_2O_5	CVD	2.5 M $LiNO_3$/0.01 M LiOH	65.9 C g^{-1}	−0.1–0.3 V	[123]
V_2O_5	Hydrothermal reaction	LiCl/PVA	131 F g^{-1}	0–1 V	[124]
V_2O_5	Spin-coating	1 M $LiClO_4$ in PC	155 F g^{-1}	−0.5–0.5 V	[125]
V_2O_5 spheres	Solvothermal process	5 M $LiNO_3$	479 F g^{-1}	−0.2–0.8 V	[126]
V_2O_5	Atomic layer deposition	1 M $LiClO_4$ in PC	900 C g^{-1}	1.8–4 V	[127]
3D V_2O_5	Vertical drying method	1 M $LiClO_4$ in PC	355 F g^{-1}	−1–1v	[129]
V_2O_5 airgel	Solvent removal method	1 M $LiClO_4$ in PC	960 F g^{-1}	1.8–3.6 V	[131]
V_2O_5/CNTs	Electrodeposition	1 M $LiClO_4$ in PC	1230 F g^{-1}	1.5–4 V	[133]
V_2O_5 nanotube/CNTs	Hydrothermal reaction	0.1 M LiTFSI	48.5 F g^{-1}	−0.5–2.5 V	[134]
VO_2 nanobelt	Hydrothermal reaction	1 M $LiPF_6$ in EC/DMC/DEC	178 mAh g^{-1}	1.5–3.5 V	[139]
LiV_3O_8 nanosheets	Sol-gel combustion route	1 M $LiNO_3$	63 mAh g^{-1}	−0.7–2 V	[141]
$Na_{0.33}V_2O_5$ nanowires	Spin-coating	1 M $LiClO_4$ in PC	498 F g^{-1}	−0.6–0.6 V	[143]
$LiNiVO_4$	Hydrothermal reaction	1 M LiOH	456 F g^{-1}	−0.2–0.6 V	[146]
Crystalline α-MoO_3	Electrochemical deposition	1 M $LiPF_6$ in EC/DEC	65 F g^{-1}	0–3 V	[149]
α-MoO_3 nanobelts	Hydrothermal reaction	0.5 M Li_2SO_4	369 F g^{-1}	−0.3–−0.1 V	[150]
MoO_3-Mo wires	High temperature calcination	PVA/LiCl	7.68 mF cm^{-1}	−0.8–0.2 V	[152]
α-MoO_3/SWCNT	Hydrothermal reaction	1 M $LiClO_4$ in PC	348.7 F g^{-1}	1.5–3.5 V	[153]
MoO_{3-x}/CNTs	Hydrothermal reaction	5 M LiCl	337 F g^{-1}	−0.1–−0.9 V	[154]
$Li_2Co_2(MoO_4)_3$	Hydrothermal reaction	2 M LiOH	130 F g^{-1}	0–1.6 V	[160]
MoS_2 nanosheets	Wet chemistry	0.5 M Li_2SO_4	400 F cm^{-3}	−0.15–0.85 V	[162]
MoS_2	Wet chemistry	1 M $LiClO_4$ in THF	250 F g^{-1}	1–2.5 V	[164]
Layered MnO_2	Hydrothermal reaction	0.5 M Li_2SO_4	280 F g^{-1}	0–1 V	[170]
MnO_2 nanoflower	Hydrothermal reaction	1 M LiOH	150 F g^{-1}	0–0.6 V	[172]
Au/MnO_2 nanowires	Wet chemistry	1 M $LiClO_4$	1010 F g^{-1}	−0.4–0.5 V	[177]
MnO_2/CNT	Wet chemistry	1 M LiAc	93.9 F g^{-1}	0.1–1.1 V	[178]
MnS/carbon	Hydrothermal reaction	3 M LiCl	710.6 F g^{-1}	−0.8–0.8 V	[179]
$LiNi_{0.5}Mn_{1.5}O_4$	Electrochemical deposition	1 M LiBF4 in EC/DMC	155 mAh g^{-1}	3.5–5 V	[180]
$LiNi_{0.8}Co_{0.2}O_2$/MWCNT	Wet chemistry	1 M $LiClO_4$ in EC/DEC	270 F g^{-1}	2.75–4.25 V	[181]
nano-$LiFePO_4$	Wet chemistry	1 M $LiPF_4$ in EC/DEC	129 mAh g^{-1}	2–3.4 V	[183]

CNTs, carbon nanotubes.

significant intercalation pseudocapacitive effect, which promoted the rate capability and long cycle life of LIBs [186]. The spinel Ni-doped $MnCo_2O_4$ material possessed fast Li^+ intercalation pseudocapacitance. The capacitive performance was closely ascribed to Li^+ intercalation pseudocapacitance and the yolk-shell structure, which can effectively prevent the particles from being pulverized, and alleviate particles volume changes in the process of cycling [187]. A flexible solid-state SC on the basis of FeS_2 nanospheres supported on carbon-paper was fabricated, which exhibited outstanding electrochemical performance, such as high capacitance of 484 F g^{-1} at 5 mV s^{-1} [188]. Lian et al. [189] indicated that flower-like C@SnS and bulk SnS exhibited intercalation pseudocapacitance. After a long-term lithiation/delithiation process, flower-like C@SnS and bulk SnS exhibited improved rate performance and reversible capacity in comparison with initial state. The pseudocapacitive behavior of $Ni_3N@Ni_3S_2$ electrode during lithium intercalation combines the diffusion-controlled capacity and surface pseudocapacitive capacity. The diffusion contribution of $Ni_3N@Ni_3S_2$ was higher than that of high pseudocapacitance Ni_3N [190]. In the Co-based MOF material, Li^+ ions are intercalated to the carboxyl groups and benzene rings of the S-Co-MOF during the electrochemical process, accompanied by the distortion of CoO_6 octahedral sites. The b-value calculation of the peak currents demonstrated that both intercalation reactions and pseudocapacitive processes contributed to the total capacity [191] (Table 1).

3.1.2. Na^+ intercalation pseudocapacitance

Recently, sodium-ion intercalation devices have been considered as potential alternatives in the application of large-scale energy storage because they are inexpensive and resourceful. Myung et al. [192] demonstrated that rate capability could be enhanced by anatase TiO_2 nanorods coated by a thin carbon layer. They also suggested that instead of an alloying reaction, the sodiation process of anatase nanorods is an intercalation reaction. Inspired by the Li^+-intercalation pseudocapacitance, great anticipation has been given to the introduction of intercalation pseudocapacitive charge-storage mechanism in electrodes to obtain excellent rate capability and lasting cycle life of energy storage devices in sodium-ion batteries. (Table 2)

3.1.2.1. Mn-based electrodes. The MnO_2 charge storage mechanism occurs via intercalation/deintercalation of sodium ions as follows:

$$MnO_2 + Na^+ + e^- \leftrightarrow MnO_2Na$$

On the basis of the ionic radii of the cations, their diffusivity is predicted to increase in the order of $Na^+ < Li^+$. In fact, the voltammetric charge in Li_2SO_4 solution is smaller than that in Na_2SO_4 solution. This can be ascribed to the larger electrical resistance of Li_2SO_4 electrolyte, which was evidenced by Qu et al. [193] using electrochemical impedance spectroscopy. Generally, manganese oxide electrodes can store charges via intercalation/deintercalation of alkali cations into oxide lattice. Two obvious anodic peaks in CV were found in birnessite-type MnO_2. Distinct redox peaks have often been observed for crystalline MnO_2, in which intercalation/deintercalation of Na^+ into/from the bulk oxide is predominant to keep the charge neutrality during the valence conversion of Mn^{3+}/Mn^{4+} [194]. Inoue et al. [194] explained it in terms of the presence of two specific sites for the intercalation of Na^+ in birnessite MnO_2. The perpendicularly oriented planes of birnessite also allow for facile insertion of the Na^+ ions for pseudocapacitive charge storage [195]. The relative pseudocapacitive contributions from surface and intercalation capacitance can be estimated from the scan rate dependence with plots of C_{MnO2} vs. $v^{-1/2}$ and $(C_{MnO2})^{-1}$ vs. $v^{1/2}$, which both show linear behavior [196,197]. At high scan rates, ion diffusion is limited and only surface capacitance contributes, whereas at low scan rates, both surface and intercalation capacitance are present [195]. The contribution from each type of charge-storage mechanism also depends on the crystal structure, water content, surface area, porosity and intercalated cations [196,197]. In contrast, crystalline α-MnO_2 materials exhibit a bulk capacitance of merely ~200 F g^{-1}, whereas the β-MnO_2 crystalline phase has a poorer bulk capacitance of ~10 F g^{-1} [198]. Hierarchical nanostructures of hydrated α-MnO_2 are reported to have a specific capacitance up to 356 F g^{-1} at 2 A g^{-1} [199]. The open structure and crystalline nature of α-MnO_2, and the presence of hydrates in MnO_2 help to improve the charge-storage process as it enhances the diffusion of Na^+, providing the sites for rapid charge transfer and cation diffusion process [200]. The cubic spinel λ-MnO_2 electrode had specific capacitance values greater than 225 F g^{-1} in neutral pH Na-based electrolyte [201]. During the Na^+ intercalation/deintercalation process, Mn_3O_4 is transformed to a layered birnessite-type MnO_2, which possesses an intercalation pseudocapacitive behavior (Fig. 11) [202]. One report suggested that the intercalation of Na^+ into birnessite type MnO_2 in aqueous media was actually protons but not Na^+ ion [171]. However, the operando Raman spectroscopy results suggest that the amount of charge stored in the electrode material correlates well with the amount of Na^+ inserted into the electrode material from the electrolyte. It is also noted that no spectral features corresponding to H^+ insertion are detected during cycling. Therefore, for layered δ-MnO_2, a charge-storage mechanism of Na^+ intercalation/deintercalation is dominated [203]. Inoue et al. [194] reported that Ni-doped MnO_2 had specific capacitances of 225 F g^{-1} 2 mV s^{-1}. K-doped MnO_2 birnessited nanosheets exhibit a gravimetric capacitance of 303 F g^{-1} in the 0.1 M Na_2SO_4 electrolyte [204]. The capacitance of Na-doped MnO_2 is 200 F g^{-1}, which is much greater than rod MnO_2 (102 F g^{-1}) [205]. Lu et al. [206] prepared a polythiophene/MnO_2 nanocomposite as the electrode with intercalation pseudocapacitive behavior. The specific capacitance are found to be 290 and 222 F g^{-1} for the current densities of 1 and 10 A g^{-1}. Patel et al. [195] synthesized the nanocomposites composed of MnO_2 and graphitic carbon. For this composite in Na_2SO_4 electrolyte, the capacitance reached 310 F g^{-1} at 200 mV^{-1}. To enhance electron transport, Huang et al. [207] prepared the direct growth of MnO_2 on carbon substrate. Carbon modification proves to improve the electrical conductivity of MnO_2 with a capacitance of 622 F g^{-1}. The MnO_2 mixed with graphene and CNTs showed a specific capacitance of 481 F g^{-1} at scan rates of 5 mV s^{-1} and cycle stability of 83.3% capacitance retention for more than 15,000 cycles [208]. In the beaded structural Mn_2O_3, both the redox and intercalation pseudocapacitance exert a major influence in the specific capacitance of the nanobeaded electrode material that was directly influenced by the interconnected beaded structure [209].

3.1.2.2. Ti-based electrodes. Despite Li^+ ions intercalation, Ti-based materials also occur as Na^+-ion intercalation reaction. For example, TiO_2 hybrid coupled by graphene featured by excellent Na^+-ion intercalation pseudocapacitance has been investigated for high-rate Na^+ ion batteries (SIBs). Chen et al. [19] were the first to indicate that intercalation pseudocapacitance plays a dominant role in the charge-storage process with respect to the graphene/TiO_2 SIB anode, resulting in superb rate capability and lasting stability. Further analysis of sodiation dynamics on the basis of first-principle calculations demonstrates that graphene hybridized by TiO_2 nanocrystals offers sodium intercalation/deintercalation with more accessible channels at the interface of grapheme-TiO_2 with rather less energy barrier. Chen et al. [210] prepared a pinecone-like hierarchical anatase TiO_2 on carbon substrate (Fig. 12). The higher surface area improves its electronic conductivity which is

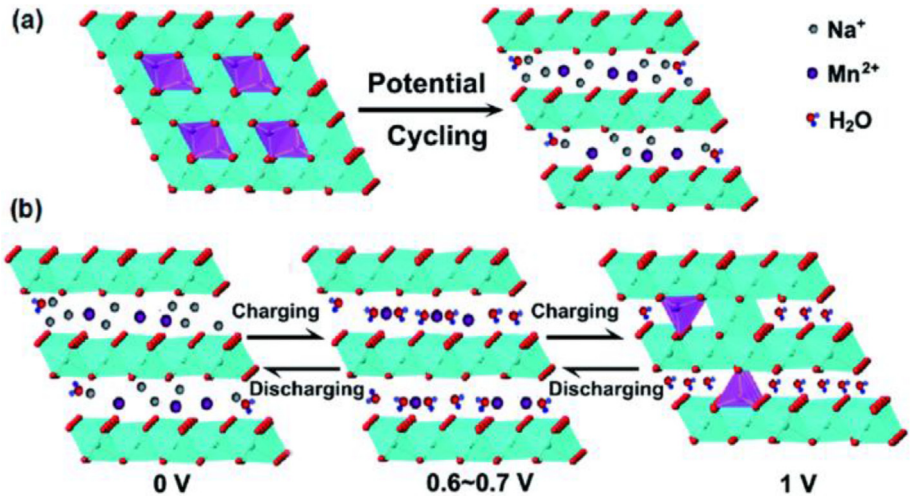

Fig. 11. Possible phase transformation during the charging/discharging process based on the in situ Raman results. Reprinted with permission from a study by Yang et al. [202]. Copyright (2015) The Royal Society of Chemistry.

resulted from conductive carbon, as well as accompanied oxygen vacancies. A sloping voltage plateau emerges at approximately 0.7 V which corresponds to the reversible Na^+ intercalation/deintercalation in host structure. Le et al. [211] synthesized a single-crystal—like anatase TiO_2, delivering a high capacity of 268 mAh g^{-1} at current density of 0.2 C and maintaining 126 mAh g^{-1} at current density of 10 C for more than 18,000 cycles. The TiO_2/carbon composite rich in defects demonstrates mooncake-shaped morphology comprised of TiO_2 nanocrystals featured by well dispersion of average 5-nm particle size in the carbon matrix. It shows a high reversible capacity of 330 mAh g^{-1} at 50 mA g^{-1} when used as an SIBs anode [212]. Yu et al. [213] fabricated a $Li_4Ti_5O_{12}$ spinel thin film and studied its inherent Na^+ ion transport kinetics and coupled pseudocapacitive charging. The intercalation pseudocapacitance is found to be in significant activation by the nanocrystalline microstructure filled with defect-rich surface, which could stimulate Na-ion and electron to access to the surface/subsurface at the same time. The rate capability, together with long-term cycle life of $Li_4Ti_5O_{12}$, could be improved by introducing an intercalation pseudocapacitive charge-storage mechanism. However, TiO_2 phases in $Li_4Ti_5O_{12}$ increases the capacity but decreases the cyclability [214]. Porous $Li_4Ti_5O_{12}$ nanofibers in the confinement of a highly conductive 3D-interconnected graphene framework exhibit a reversible capacity of 195 mAh g^{-1}, which are attributed to the unique structure that provides Na^+ diffusion with short pathways, electron transport with conductive networks, and Na^+ adsorption with many interfacial sites [215]. Xu et al. [216] used the MoS_2 quantum dots to modify $Li_4Ti_5O_{12}$ to boost the electrochemical properties. The Na^+-ion intercalation pseudocapacitance dominated the total capacity. Dong et al. [217] reported a facile method for the in situ growth of $Na_2Ti_3O_7$ on 1D CNTs in the application of an anode material for sodium-ion capacitors. All the b values are fluctuant close to 1, meaning the kinetics of pseudocapacitive contribution. Based on the quantitative calculation, ca. 52.7% of the entire capacity is derived from capacitive contribution at a sweep rate of 0.6 mV s^{-1}. $NaTi_3O_7$ can also use Ti as the substrate. The as-prepared nanoarrays electrode showed exceptionally stable and excellent performance of Na storage in the application of binder-free anodes for sodium-ion battery with a capacity of 227 mAh g^{-1} [218]. Ni et al. [219] introduced S into TiO_2 substrate and the resulting nanoarrays exhibited an improved electrochemical Na-storage activity. Nanostructured $Na_2Ti_3O_7$ layered electrode delivers a large reversible capacity of 114 mA h g^{-1} at 0.1C [220]. The kinetics of $NaTi_2(PO_4)_3$/carbon was investigated in aqueous sodium nitrate solution. Its capacity can reach 70 mAh g^{-1} at 1C rate [221]. Wang prepared $NaTi_2(PO_4)_4$ nanoparticles implanted in the mesoporous carbon matrix. The capacity loss is negligible when increasing the current rate from 50 to 100 C, which could be attributed to the contribution of intercalation pseudocapacitance [222]. The excellent energy and power densities of $Na_2Ti_2O_4(OH)_2$ are also more contributed from Na^+ intercalation pseudocapacitive effect [223]. Zou et al. [224] synthesized a new class of core-shell MAX@$K_2Ti_8O_{17}$ by alkaline hydrothermal reaction and hydrogenation of MAX, which granted high sodium ion-intercalation pseudocapacitance.

3.1.2.3. Mo-based compounds. Molybdenum oxides and molybdenum sulfides are typical pseudocapacitive materials, respectively. The former exhibit pseudocapacitance on surface form and the latter in bulk form. The intertwined MoO_3-CNTs composite electrode was found to be superior to those of either MoO_3 nanowires or randomly entangled mesoporous MWCNTs. The MoO_3 nanowires have a highly crystalline layered structure and the CNTs provide facile conducting pathways for the cations to enter into the van der Waals gaps, giving rise to an intercalation pseudocapacitance mechanism. Consequently, it obtained a capacitance of 178 F g^{-1} [225]. Shakir et al. [226] coated the MoO_3 by SnO_2 and this core-shell electrode reached a specific capacitance of 295 F g^{-1}, which was much higher than pure individual MoO_3 (69 F g^{-1}). Saji et al. [227] studied Mo/Mo oxides composite electrode and the Na^+ intercalation pseudocapacitance was only observed in an inner layer of electrodes.

As a graphene-like 2D material, MoS_2 nanosheets have demonstrated distinctive structural and electronic characteristics. Their multiple layers are stacked by van der Waals force, which allows Na^+ to intercalate easily. Cao et al. [228] found that the fade of small capacitance in the initial 150 cycles based on stability testing was likely owing to the saturation of the 'active' sites on MoS_2 film surface in the process of charge-discharge, and the increase in later cycles could be resulted from capacitance behavior induced by the 'intercalation' which were owing to Na^+ intercalation into van der Waals gaps of multilayers of MoS_2(Fig. 13). The capacitance of MoS_2/graphene electrode was found to increase significantly with continued cycles. This was because layered material re-exfoliated partially with persistent ion intercalation, and the specific capacitance increased via intercalation

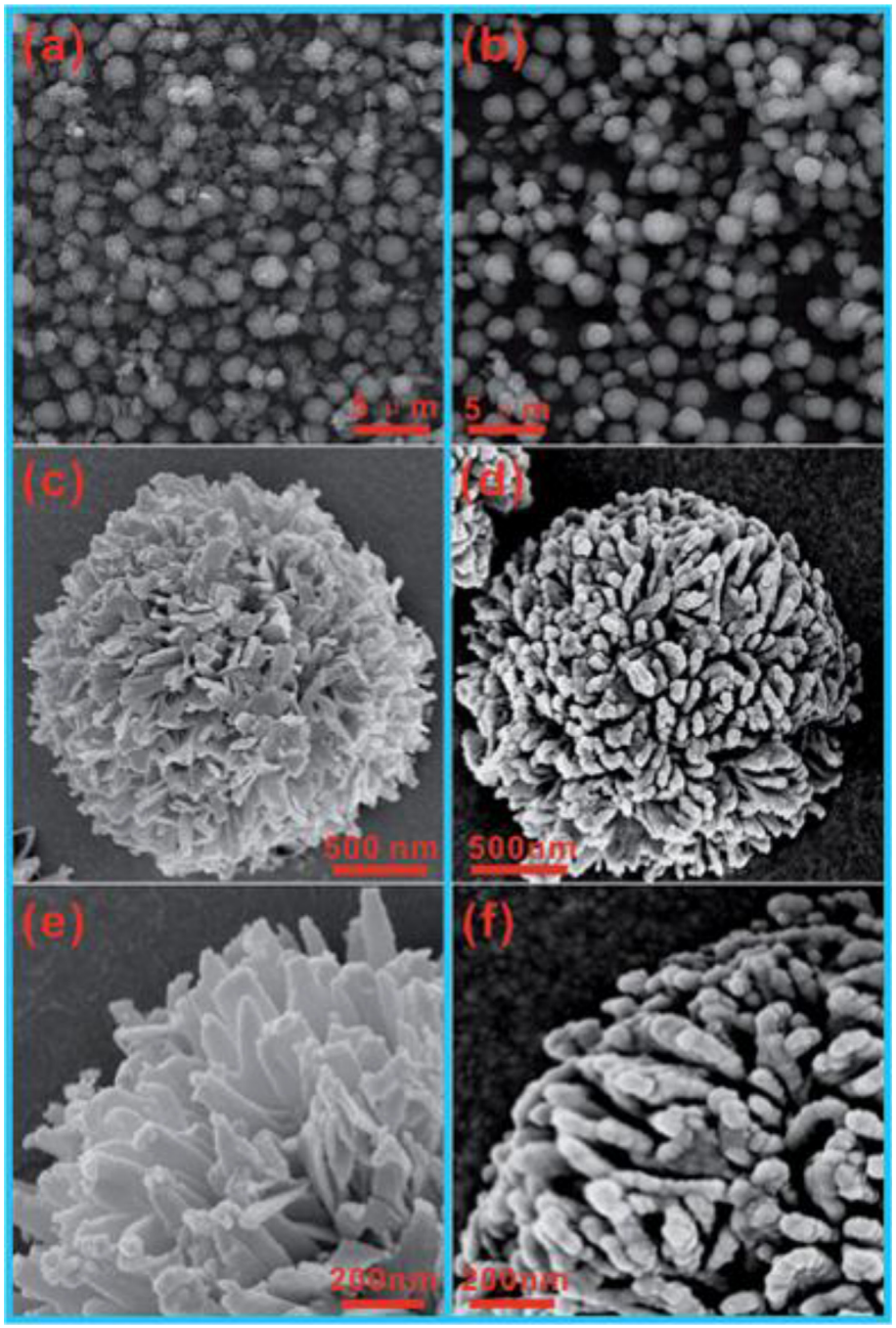

Fig. 12. SEM images of hierarchical anatase TiO_2 on carbon substrate at various magnifications. Reprinted with permission from a study by Chen et al. [210]. Copyright (2016) The Royal Society of Chemistry.

pseudocapacitance [229]. Cook et al. [163] demonstrated that MoS_2 was a versatile ion storage host that was capable of achieving fast kinetics and good cycling performance by synchrotron grazing incidence X-ray diffraction techniques. Huang et al. [230] reported that the expanded interlayer spacing of MoS_2 facilitated Na^+ diffusion in the 2D channels and reduced the volume change of MoS_2 during discharge/charge. Meanwhile, the 1T-phase of MoS_2 can inhibit the phase transition during Na^+ intercalation/deintercalation. This phenomenon was also demonstrated by Wang et al. [231] in the electrode of MoS_2/carbon. In addition, nanoflower-like MoS_2 on the carbon fibers also provided a wide interlayer spacing, which could reduce the ion diffusion pathways and resistance but enhance the availability and accessibility of active surface areas, and thereby ensuring the fast mass transport [232].

3.1.2.4. Other materials. The electrolyte can be easily accessed by intercalation sites of V_2O_5 within the nanocomposites [233]. Based on the simulation, Parija et al. [120] demonstrated that different phases of V_2O_5 had different mobility of Na^+ in the bulk materials. In the V_2O_5/CNTs electrode, interconnected pore channels filled with the electrolyte are formed by interpenetrating structure, thus guaranteeing ion to transport facilely and providing the electrolyte with access to the redox-active material. In addition, effective

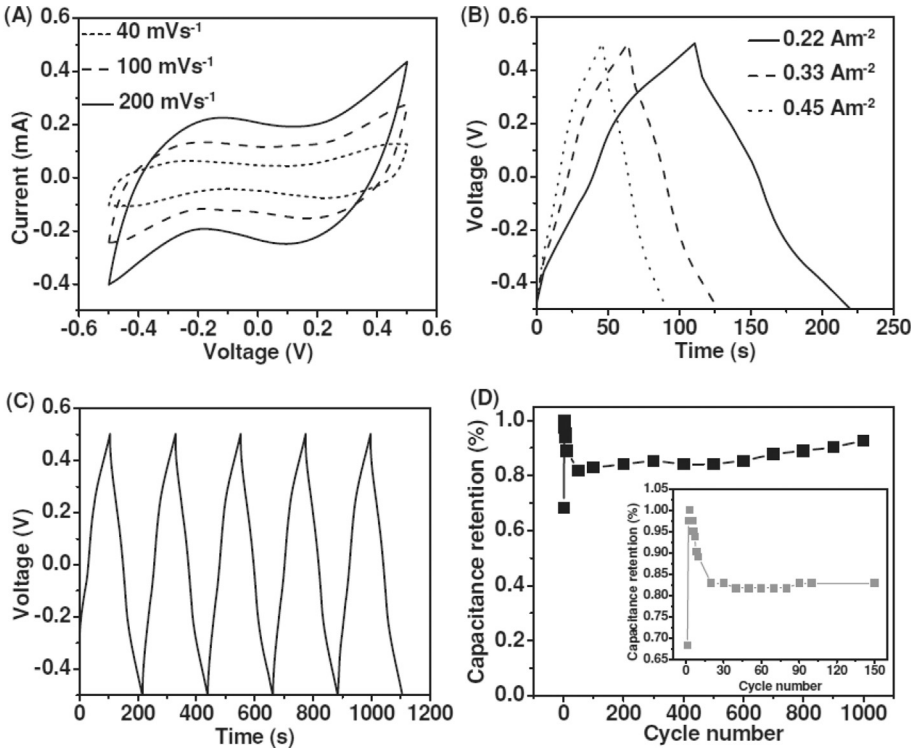

Fig. 13. The electrochemical measurement of MoS_2 film–based microsupercapacitor. Reprinted with permission from a study by Cao et al. [228]. Copyright (2013) John Wiley and Sons.

electron transport can be achieved by the conductive CNT network, whereas ion diffusion paths can be shortened by the small dimension of the nanowires. Consequently, a rapid process of pseudocapacitive charge storage happens, probably preventing phase transformations in ion intercalation/deintercalation, and enhancing cycling stability. This pseudocapacitance is primarily associated with Na^+ intercalation process [233]. Fleischmann et al. [138] synthesized V_2O_5 by ALD on mesoporous carbon substrate. Pseudocapacitive intercalation does not lead to phase transformation for the host lattice and is likely to happen on partial nanometer-sized V_2O_5 coatings in which solid-state diffusion no longer limits intercalation kinetics [4]. α-V_2O_5 shows perfect capacitive properties with a specific capacitance of approximately 238 F g^{-1} at 2 A g^{-1}, but bad cycling stability with a persistent decrease in the initial 2000 cycles before its maintenance [234]. Pan et al. [235] reported that VO_2 had a Faradaic effect–based pseudocapacitance through Na^+ ion intercalation and reaction in the subsurface. Consequently, a specific discharge capacitance of 300 F g^{-1} at 1 A g^{-1} was obtained. Sun et al. [236] showed the intercalation pseudocapacitance in the layer-by-layer stacked VS_2, which had a specific capacity of 150 mA h g^{-1} even at a rate of 20 A g^{-1}. A simple solvothermal approach is used to synthesize the assemblies of hierarchical flower-like VS_2 nanosheets, and the mechanism of intercalation pseudocapacitance governs the sodium storage, especially when current rates are high [237]. The calculated b-value of $NaFe_{0.95}V_{0.05}PO_4$ demonstrated a bulk intercalation reaction [238].

Wang et al. [239] prepared partially single-crystalline mesoporous T-Nb_2O_5 nanosheets composited with graphene, which displayed excellent intercalation pseudocapacitance by shortening Na^+ diffusion pathways and accelerating electron transport. Yang et al. [240] demonstrated that excellent capacitance of Nb_2O_5/CNTs can be ascribed to the inherent intercalation pseudocapacitive behavior. As a Na^+ intercalation pseudocapacitive material, peanut-like Nb_2O_5/carbon electrode delivered a remarkably excellent energy density of 43.2 Wh kg^{-1} and high power density of 5760 W kg^{-1} [241]. The introduction of graphene into Nb_2O_5 not only exhibits mesoporous structure and thin characteristic but also has a vertical (001) facet with a large interplanar lattice spacing of 3.9 Å to the surface of nanosheets. Such particular characteristics provide a large number of open and short pathways for the fast diffusion of Na^+ during charge/discharge processes [239]. Yan et al. [242] suggested that graphene can improve charge transfer and alleviate the volume change in the process of sodiation/desodiation and also offer the storage of sodium ions with more active surface area.

Two-dimensional conductive carbide layers are combined by MXenes with a hydrophilic surface primarily terminated by hydroxyl. Thus, Na^+ can be intercalated electrochemically and offers capacitance in short time [243]. Dall'Agnese et al. [244] studied Na^+-intercalation mechanism with capacitance of 100 F g^{-1} at 0.2 mV s^{-1}, which correlated well with a pseudocapacitive intercalation mechanism. Wang et al. [245] demonstrated that a high rate capability was achieved by the pseudocapacitance of the nanosheet compound MXene Ti_2C relative to Na^+-ion intercalation electrodes, which was because Ti_2C enables reversible intercalation/deintercalation of Na^+ into the interlayer space. The diffusion behavior of Na^+ ions in the interlayer of Ti_2CT_2 MXene nanosheets directly matters the intercalation pseudocapacitance. The high-rate performance is also mainly determined by Na-ion mobility on the surface. Thus, diffusion barriers of Na-ions in the interlayer of Ti_2CT_2 are calculated to provide comprehension on the intercalation pseudocapacitance and rate performance [246]. Kajiyama et al. [247] revealed that reversible intercalation/deintercalation of Na^+ into the interlayer space was exhibited by MXene $Ti_3C_2T_x$ in a non-aqueous Na^+ electrolyte. However, the present electrode materials still demonstrate unpleasant capacity, undesirable rate capability, or bad cycling stability in Na^+ ion-based energy storage systems

Table 2
Summary of electrode materials with Na-ion intercalation pseudocapacitance.

Electrode materials	Synthesis method	Electrolyte	Capacity or capacitance	Potential range	Reference.
MnO_2 nanolayer	Electrodeposition	0.5 M Na_2SO_4	225 F g^{-1}	0–0.8 V	[194]
α-MnO_2	Wet chemistry	1 M Na_2SO_4	356 F g^{-1}	0–0.9 V	[199]
λ-MnO_2	Electrochemical delithiation	1 M Na_2SO_4	225 F g^{-1}	0–1.6 V	[201]
$K_{0.15}MnO_2$ nanosheets	Wet chemistry	0.1 M Na_2SO_4	303 F g^{-1}	0–0.9 V	[204]
Na-doped MnO_2	Hydrothermal reaction	1 M Na_2SO_4	200 F g^{-1}	0–0.9 V	[205]
polythiophene/MnO_2	Wet chemistry	1 M Na_2SO_4	290 F g^{-1}	−0.1–0.8 V	[206]
MnO_2 nanoparticles	Wet chemistry	1 M Na_2SO_4	310 F g^{-1}	−0.4–0.4 V	[195]
MnO_2/carbon	Hydrothermal reaction	1 M Na_2SO_4	622 F g^{-1}	−0.2–1 V	[207]
MnO_2/CNTs	Electrodeposition	0.1 M Na_2SO_4	346 F g^{-1}	0–0.8 V	[208]
TiO_2/carbon	Hydrothermal reaction	1 M $NaClO_4$ in PC	264.1 mA h g^{-1}	0.01–2.5 V	[210]
TiO_2/graphene	Microwave solvothermal method	1 M $NaClO_4$ in EC/PC	268 mAh g^{-1}	0–3 V	[211]
TiO_2/carbon	Hydrothermal reaction	1 M $NaClO_4$ in DEC/PC/EMC	330.2 mAh g^{-1}	0.001–3V	[212]
$Li_4Ti_5O_{12}$	Pulsed laser deposition	1 M $NaClO_4$ in EC/PC	225 mAh g^{-1}	0–3 V	[213]
$Li_4Ti_5O_{12}$ nanosheets	Hydrothermal reaction	1 M $NaClO_4$ in DEC/EC/FEC	145 mAh g^{-1}	0.3–2.5 V	[214]
$Li_4Ti_5O_{12}$ nanofibers	Hydrothermal reaction	1 M $NaClO_4$ in EC/PC	195 mAh g^{-1}	0.05–3 V	[215]
$MoS_2/Li_4Ti_5O_{12}$	Hydrothermal reaction	1 M $NaClO_4$ in EC/PC	101 mAh g^{-1}	0.5–2.5 V	[216]
$Na_2Ti_3O_7$@CNT	Hydrothermal reaction	1 M $NaClO_4$ in DEC/EC/FEC	344 mAh g^{-1}	0.01–2.5 V	[217]
$Na_2Ti_3O_7$ nanoarrays	Hydrothermal reaction	1 M $NaClO_4$ in DEC/EC/FEC	227 mAh g^{-1}	0.01–2.5 V	[218]
$NaTi_2(PO_4)_3$/carbon	Gel-combustion	Saturated $NaNO_3$	70 mAh g^{-1}	−1.1–0.5 V	[221]
MoO_3/MWCNTs	Hydrothermal reaction	1 M NaOH	178 F g^{-1}	−0.75–0.3 V	[225]
SnO_2/MoO_3	Hydrothermal reaction	1 M Na_2SO_4	295 F g^{-1}	0–1 V	[226]
Mo/MoO_3	Commercial products	0.6 M Na_2SO_4	1400 μF cm^{-2}.	−0.05–−0.1 V	[227]
MoS_2 films	Hydrothermal reaction	1 M NaOH	178 F cm^{-3}	−0.5–0.5 V	[228]
MoS_2/graphene	Hydrothermal reaction	1 M Na_2SO_4	1.83 mF cm^{-2}	0–1 V	[229]
MoS_2 nanosheets	Hydrothermal reaction	1 M $NaClO_4$ in DEC/EC/FEC	129 mAh g^{-1}	0.6–3 V	[230]
MoS_2/carbon	Hydrothermal reaction	1 M $NaClO_4$ in DEC/EC/FEC	200 mAh g^{-1}	0.4–4.2 V	[231]
MoS_2/carbon fibers	Electrospinning	1 M $NaClO_4$ in DEC/EC/FEC	104 mAh g^{-1}	0.01–3 V	[232]
V_2O_5/CNTs	Hydrothermal reaction	1 M $NaClO_4$ in PC	400 C g^{-1}	1.5–3.2 V	[233]
α-V_2O_5 nanowires	Hydrothermal reaction	1 M Na_2SO_4	238 F g^{-1}	0–0.9 V	[234]
VO_2	Ball mill	1 M Na_2SO_4	300 F g^{-1}	0–0.8 V	[235]
VS_2 nanosheets	Hydrothermal reaction	1 M $NaSO_3CF_3$ in DGM	250 mAh g^{-1}	0.4–2.2 V	[236]
$NaFe_{0.95}V_{0.05}PO_4$/C	Sol-gel	Saturated $NaNO_3$	105 mAh g^{-1}	−0.8–1 V	[238]
T-Nb_2O_5/CNFs	Electrospinning	1 M $NaClO_4$ in EC/DEC	150 mAh g^{-1}	0.01–2.8 V	[240]
MXene	Wet chemistry	1 M $NaPF_6$ in EC/DMC	100 F g^{-1}	1–3.5 V	[244]
MXene $Ti_3C_2T_x$	High temperature calcination	1 M $NaPF_6$ in EC/DEC	270 mAh g^{-1}	0.1–3 V	[247]

CNTs, carbon nanotubes.

owing to the obvious disparities with regards to size and valence between Li^+ ion and Na^+ ion [170] (Table 2).

3.1.3. Other cation intercalation pseudocapacitance

Generally, Li^+ and Na^+ ions are the most popular cations for intercalation pseudocapacitance. Besides, some other cations, such as K^+, Mg^{2+} and Al^{3+}, could be used as the intercalated ions, as well to produce pseudocapacitance. Different cations were capable to be intercalated along certain planes to show electrochemical performance [190].

Lee et al. [248] found that the intercalation of K^+ would induce the pseudocapacitance for MnO_2 electrode and increasing K^+ concentration in the electrolyte would increase the extent of K^+ intercalation at high scan rates. Li et al. [249] prepared MnO_2 nanoflowers and tested it in the neutral aqueous electrolyte (KCl). This electrode delivered the highest specific capacitance of 81.7 F g^{-1} and an exceptional energy density of 45.4 W h kg^{-1} at 163.5 W kg^{-1}. The K^+ intercalation pseudocapacitance in MnO_2 was also demonstrated by the operando Raman spectroscopy [173]. Cao et al. [250] reported that a layered birnessite-MnO_2 nanoflakes with K^+ pre-intercalation was in situ fabricated on the graphene foam through a one-step simple hydrothermal method. The adjustment in the reaction parameters could control the amount of pre-intercalated K^+. The optimal amount of pre-intercalated K^+ not only improved the intercalation pseudocapacitance, but also enhanced the cycling stability of electrode in corresponding electrolyte. As shown in Fig. 14, an increase in interlayer distance is beneficial for cations to diffuse rapidly in layered MnO_2 hosts based on theoretical calculation and kinetic analysis [170]. Zeng et al. [251] deposited MnO_2 particles at electrospun carbon nanofibers film. This electrode exhibited a capacitance of 141.7 F g^{-1} at 5 mV s^{-1}. Bakhmatyuk et al. [252] observed the intercalation pseudocapacitance in activated carbon electrode with KOH electrolyte. The capacitance reached to 160–260 F g^{-1}, greater than that of double electric layer. Nitrogen-doped carbon has a stronger ability of K^+ adsorption and higher electronic/ionic conductivities, delivering a high rate capability of 154 mA h g^{-1} at 72 C [253]. Maiti et al. [254] reported an MOF-derived CeO_2 with a pseudocapacitance higher than its theoretical capacitance in K^+-based electrolyte. This is due to the extra contribution from the K^+ intercalation pseudocapacitance. The K^+ intercalation behavior of layered Ti_3C_2 Mxene was verified by Lin and Zhang [255]. The energy storage mechanism of layered Ti_3C_2 is intercalation pseudocapacitance that happens accompanied by the ions intercalation into the layers of the bulk material, and the mechanism is good for thick electrodes. Therefore, electrodes with large mass loading could maintain high electrochemical performance. Guan et al. [256] reported an α-MoO_3 with electrochemical deposition on TiO_2 nanotubes in good alignment. The electrochemical testing demonstrated that not only conventional redox pseudocapacitance but also intercalation pseudocapacitance occurred in the α-MoO_3. As a result, it exhibited a capacitance as high as approximately 75.0 F g^{-1} at a scan rate of 5 mV s^{-1} in the electrolyte of 1 M KCl solution. K^+ was able to intercalate along the (010) facet of MoO_3 and showed excellent intercalation capacitance of 180 F cm^{-3} [257]. Tian et al. [258] indicated that the intercalation pseudocapacitance played a dominant role in the charge storage of the MoO_3/carbon nanofibers electrode, while a small amount of diffusion-controlled K-ion intercalation was also involved.

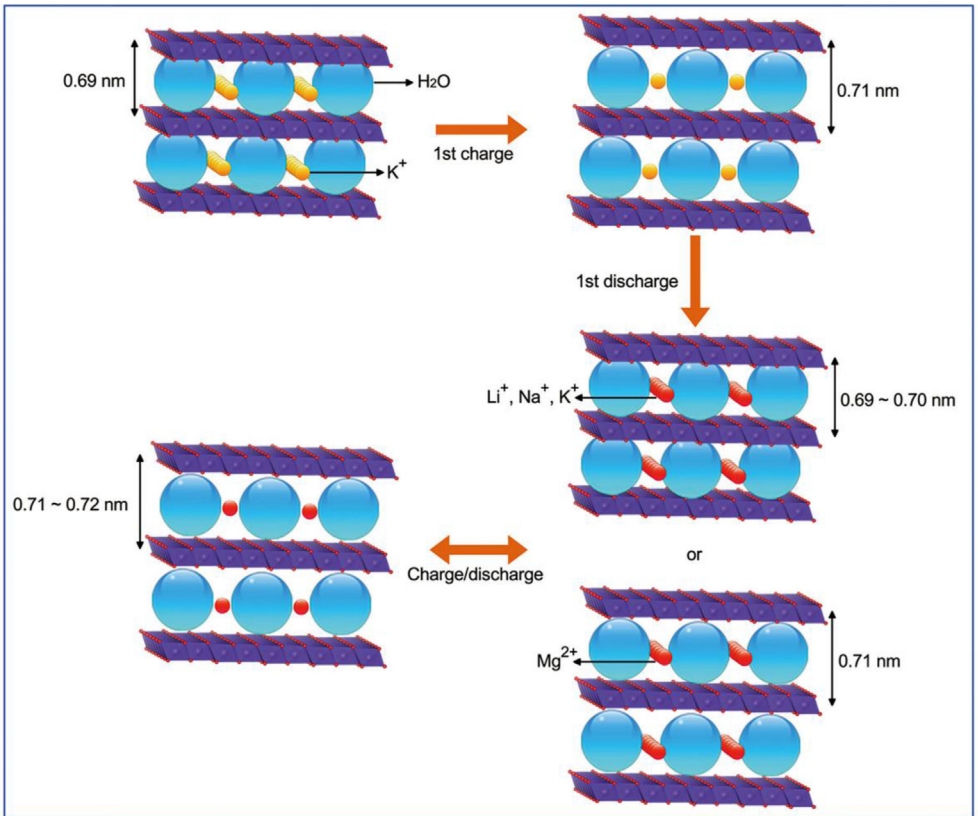

Fig. 14. Schematic of the reversible intercalation/deintercalation of Li^+, Na^+, K^+, and Mg^{2+} ions in layered K-MnO_2. Reprinted with permission from a study by Xiong et al. [170]. Copyright (2017) American Chemical Society.

The development of Mg^{2+}-based batteries and related electrolytes has been discussed recently [259–261]. However, just a few investigations focus on the intercalation pseudocapacitance induced by Mg^{2+} intercalation. Amatucci et al. [262] demonstrated the Mg^{2+}-intercalation pseudocapacitance in the nanocrystalline V_2O_5. The capacity of V_2O_5 was 180 mA g^{-1} in Mg^{2+}-based electrolyte, much higher than that in the Li^+-based electrolyte. This may be due to the additional pseudocapacitance and higher valence of Mg^{2+}. Based on the CV curves of layered V_2O_5 electrode, the intercalation pseudocapacitance happened during the Mg^{2+} intercalation/deintercalation process [263]. As a layered material, MoO_3 also provides the space for Mg^{2+} intercalation, which induced the pseudocapacitance [263]. The Mg^{2+} intercalating into MoO_3 has the capacitance of 265 F cm^{-3} at 0.5 A g^{-1}, which is due to the similar ion size of Mg^{2+} and Li^+ [257].

Among multivalent ions, Al^{3+} ion is able to meet the requirement of small ionic radius and low cost. In addition, Al^{3+} supports multi-electron redox reactions. Therefore, for the same amount of insertion as the monovalent ions, three times electrons can be injected into/extracted from the electrochromic host. Reversible Al^{3+} ion storage behavior in aqueous electrolyte was also proposed for anatase TiO_2 nanotubes. In the case of TiO_2 electrodes, redox reactions of Ti^{3+}/Ti^{4+} at or near the surface result in a pseudocapacitance storage mechanism instead of Al-ion intercalation [264]. Fast and highly reversible Al^{3+} ion intercalation in CuFe-PBA from Al^{3+} ion based aqueous electrolyte was observed. It displayed the typical characteristics of intercalation pseudocapacitance [265]. Jiao et al. [266] observed the intercalation pseudocapacitance in the multiwalled CNTs in the ionic liquid $AlCl_3$/[EMIm]Cl-based electrolyte. Parija et al. [120] investigated the Al^{3+}-intercalation process into the V_2O_5 phase and the phase transformation by simulation. Li et al. [267] prepared $W_{18}O_{49}$ nanowires with wide lattice spacing and layered single-crystal structure and demonstrated the Al^{3+}-intercalation process into the electrode. The high areal capacitances and capacities of the electrodes were mainly owing to $W_{18}O_{49}$ nanowires–based Al^{3+}-intercalation pseudocapacitance instead of the contribution of SCNTs and proton intercalation.

3.2. Anion intercalation pseudocapacitance

Perovskite oxides are the typical anion intercalation materials in the aqueous alkaline solution, (Table 3) which demonstrate by Kudo [268] in 1990s. Perovskite oxides have a typical structure formula of ABO_3 (Fig. 15). As described previously, the larger A-site

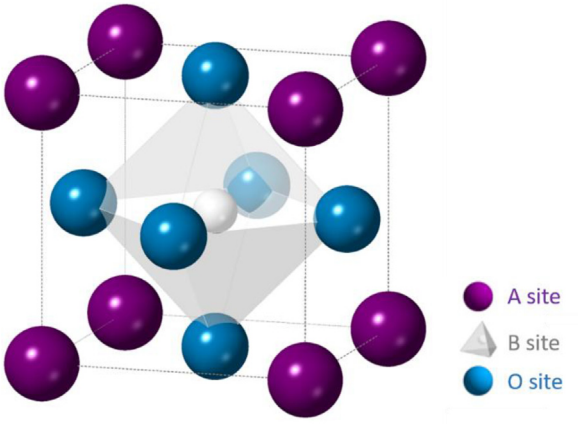

Fig. 15. Typical crystal structure of perovskite ABO_3.

cation is normally a rare-earth or alkaline earth metal element, featured by 12-fold oxygen coordination, whereas the smaller B-site cation is usually a transition metal element characterized by 6-fold oxygen coordination. Normally, A and B cations have the total positive valence of 6, equals to the entire negative valence of oxygen anions. Representative formulas are $A^{2+}B^{4+}O_3$, $A^{1+}B^{5+}O_3$, and $A^{3+}B^{3+}O_3$. $ABO_{3-\delta}$ is the most common form for a majority of perovskite, where δ represents the deficiency or surplus of the oxygen anion relying on the entire valence amount of A- and B-site cations [29]. Owing to various requirements for ionic radius, A- and B-site of ABO_3 perovskite include different types of elements. A-site cation is usually characterized by larger size (1.10−1.80 Å), whereas B-site cation by medium size (0.62−1.00 Å) The following tolerance factor can describe the size limit of ionic radius which could be tolerated for the maintenance of specific structure:

$$t = \frac{R_A + R_B}{\sqrt{2}(R_B + R_O)}$$

where R_A, R_B, and R_O denotes the radius of A-site cation, B-site cation, and oxygen anion, respectively. When t equals to 1, it demonstrates the perfect formation of cubic structure and when it deviates from 1, it represents a discordance between the equilibrium A-O and B-O bond lengths [29]. The perfect simple perovskite structure could be considered as a cubic close-packed structure where the oxygen and the A-site cations are stacked along the cubic [110] direction. Incorporation of various metal elements (at different amounts) in its A and B-site could adjust its structure and composition [29,269]. In addition, both A and B sites could be replaced by other metal cations to form $A_{1-x}A'_xBO_3$ or $AB_{1-y}B'_yO_3$. Furthermore, the adjustable bulk and surface components, as well as the easy tailoring of the physical and chemical properties of perovskite oxides offer great potential to tune the electrochemical properties. Compared with other simple oxides, perovskite oxides have fascinating physical, chemical, and catalytic properties with low cost and environmental friendliness.

Following the pioneer works of Kudo et al., Magnone et al. [270] studied the oxygen intercalation into La_2CuO_4 perovskite oxides. They found that the oxygen anions intercalation was appeared at various potentials for fixed time in the alkaline solution at room temperature. It seems that oxygen intercalation can occur at potentials a bit smaller than oxygen evolution reaction and carries out on a parallel pathway to O_2 evolution at higher anodic potentials. Normally, the oxygen diffusion into the material experiences two processes. First, fast diffusion occurs via a network of extended defects; second, slow diffusion inside the microdomains enclosed by the defect network leads to observable structural changes [271−273]. Unfortunately, they did not make a connection between the oxygen-ion intercalation behavior and the pseudocapacitance. Until 2014, Mefford et al. [28] investigated the mechanism of oxygen-ion intercalation pseudocapacitive behavior in the perovskite $LaMnO_3$ (Fig. 16). It is the first time to report oxygen anion-based intercalation pseudocapacitance and oxygen intercalation for rapid energy storage.

Thermal treatment of perovskite oxides under reduction atmospheres is a very common way to increase the oxygen vacancy concentration of perovskite oxides. Mefford et al. [28] prepared $LaMnO_3$ particles at 700 °C by a reverse-phase hydrolysis method. The $LaMnO_{3-\delta}$ materials were then reduced in a 7% H_2/Ar atmosphere at 400 °C. The oxygen vacancy concentration, determined by iodometric titration of reduced $LaMnO_{3-\delta}$, was about 12% more than the original $LaMnO_{3-\delta}$. Consequently, the specific capacitance of original $LaMnO_3$ and reduced $LaMnO_3$ is 586.7 and 609.8 F g^{-1} at 2 mV s^{-1}, respectively. Coincidently, the enhancement in capacitance with respect to the oxygen-deficient sample is in similarity

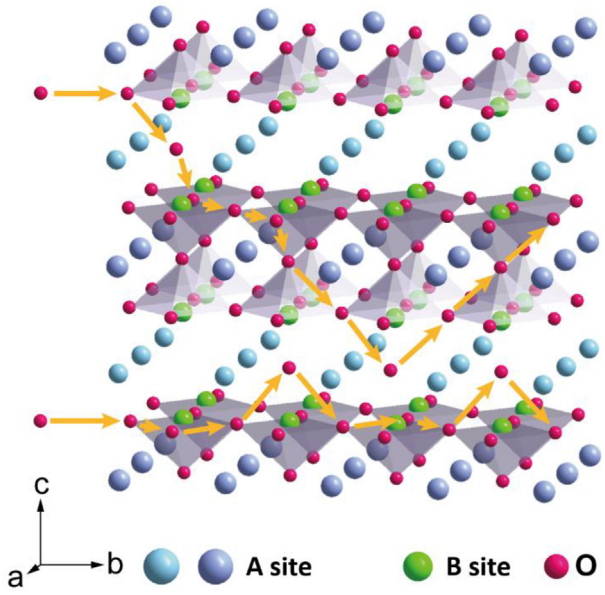

Fig. 16. Mechanism of oxygen intercalation into perovskite oxides.

with the difference in oxygen content between the two materials. Zhu et al. [22] reported the oxygen anions intercalation pseudocapacitive behavior of Nb-doped $SrCoO_{3-\delta}$ perovskite. After thermal treatment in 10%H_2/Ar atmosphere at 500 °C for 5 min, the tetragonal structure was still maintained without the appearance of second phases. However, the amount of oxygen vacancies in the oxide lattice increased from 10.3% for initial sample to 19.4% for the sample after the treatment. For the intercalation pseudocapacitive process, intercalating an electrolyte oxygen ion through OH^- and diffusing O^{2-} along unit cell edges can fill oxygen vacancies, accompanied by the oxidation of Co^{2+} to Co^{3+}. The intercalation of surplus O^{2-} was occurred on the surface through the diffusion and oxidation of Co^{3+}. To enhance the oxygen vacancy concentration, Liu et al. [31] synthesized the double-layered perovskite of $PrBaMn_2O_{6-\delta}$ (f-PBM) which was further treated in H_2 at 800 °C (r-PBM). The oxygen vacancy concentration was increased from 0.125 to 0.715 for r-PBM. The higher oxygen vacancy also led to a larger oxygen diffusion rate, which is ascribed to better power density (Fig. 17). Interestingly, the high-temperature thermal treatment in reducing atmosphere not only enhanced the oxygen deficient structure but also transferred the crystalline structure of PBM from the mixed cubic and hexagonal structure to the pure cubic structure. Furthermore, the oxygen vacancy formation energies of two phase of PBM were calculated by DFT calculation. The cubic PBM is 2.19 eV, which is less than the hexagonal PBM. It suggests the formation of an oxygen vacancy is somewhat easier in cubic PBM than in the hexagonal phase. Therefore, the oxygen vacancy concentration of r-PBM is rather greater than that of f-PBM. Consequently, f-PBM and r-PBM demonstrate excellent gravimetric capacitance of 462.3 and 1034.8 F g^{-1} at 1 A g^{-1}, respectively. Forslund et al. [274] reduced the $CaMnO_3$ perovskite in 7%H_2/Ar gas to obtain high oxygen vacancy contents. The reduced $CaMnO_3$ possessed oxygen vacancies four times higher than original $CaMnO_3$.

Another way for the modification of perovskite material is to partially substitute the cations in A or B-site partially with different cations of various ionic radius and valence. Such substitution is beneficial to obtain desirable oxygen vacancies, ionic conductivity, and electric conductivity of perovskite oxides. For example, oxygen vacancies and electron conduction could be improved by the

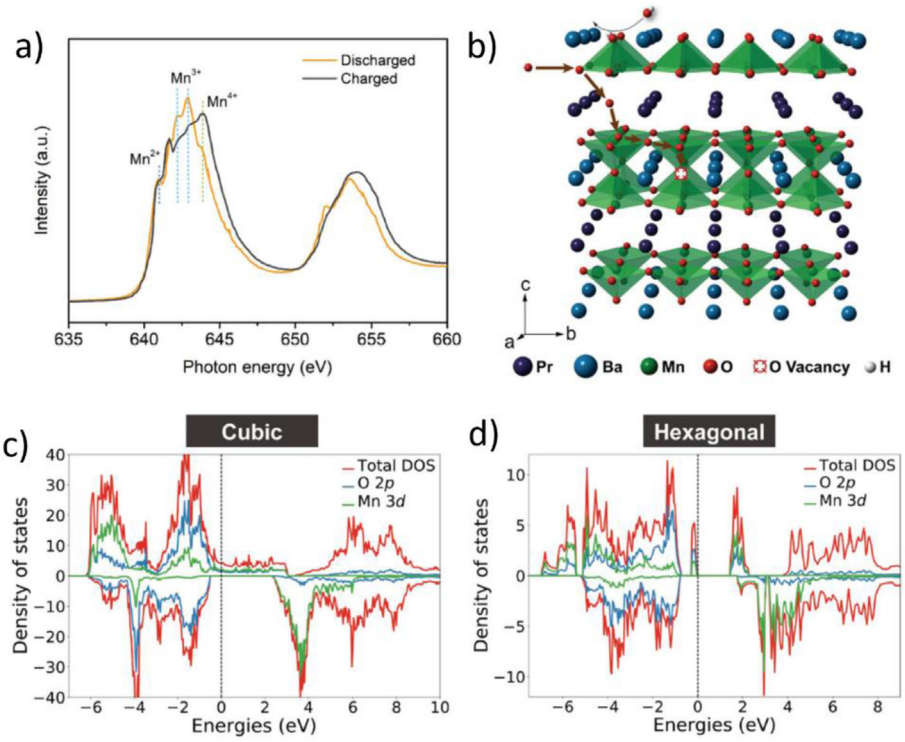

Fig. 17. (a) Near edge X-ray absorption fine structure (NEXAFS) spectra measured at the Mn 2p adsorption edge (Mn L-edge). (b) A schematic diagram of oxygen intercalation into r-PBM during the energy storage process. DFT + U calculated density of states (DOS) for (c) cubic and (d) hexagonal PBM. Reprinted with permission from a study by Liu et al. [31]. Copyright (2018) John Wiley and Sons. PBM, $PrBaMn_{2O6-\delta}$.

incorporation of metal cation featured by low valence into A-site and the incorporation of transition metal elements into B-site, respectively [275]. Wang et al. [276] prepared $LaMnO_3$ perovskite oxide doped by 15% Sr as the electrode of SC. The specific capacitance of $La_{0\cdot85}Sr_{0\cdot15}MnO_3$ and $LaMnO_3$ is 198 and 187 F g^{-1} at 0.5 A g^{-1}, respectively. The higher specific capacitance of $La_{0\cdot85}Sr_{0\cdot15}MnO_3$ can be resulted from the 3D structure and higher conductivity. After comparing a series of $La_{1-x}Sr_xMnO_3$ perovskites, Lang et al. [277] came to the same conclusion that 15% dopant is optimal. They also suggested that the charge-storage efficiency of the sample may vary due to the doping of strontium. Cao et al. [278] studied the influence of A-site element on the electrochemical properties of $La_xSr_{1-x}CoO_{3-\delta}$ ($0.3<x<1$) nanofibers. The different ratio of Sr in the A site did not affect the crystalline structure, maintaining a pure single rhombohedral phase. With the increase in Sr content, the diameters of samples decrease and the roughness of surface enlarge. The best specific capacitance (747.8 F g^{-1} at 2 A g^{-1}) of $La_xSr_{1-x}CoO_{3-\delta}$ was obtained at $x = 0.7$. The change in specific capacitance of $La_xSr_{1-x}CoO_{3-\delta}$ with Sr content is due to the variation of oxygen vacancies and the appearance of lattice distortion, and the oxygen vacancies increase markedly with the growth of Sr-doping. Alexander et al. [33] found that increasing the Sr^{2+} content would enhance the oxygen vacancy concentration. Although small amount of Sr substitution would introduce some oxygen vacancies into the perovskite structure, excessive Sr substitution caused structural distortion, thus causing the degeneration of electrochemical properties [279]. Liu et al. [31] reported a double perovskite oxide of $PrBaMn_2O_{6-\delta}$ and its cubic phase with layered structure facilitated the oxygen-ion diffusion and the oxygen vacancy concentration, thus contributing to the outstanding capacitance. Wang et al. [280] reported an A site cation-ordered double perovskite $PrBaCo_2O_{6-\delta}$ oxide in the application of the electrode for anion intercalation SC. The oxygen atoms in this perovskite located in the Pr^{3+} planes can be partially or even entirely removed, producing numerous oxygen vacancies to significantly enhance the diffusivity of ions in the reaction. However, not all A-site doping could result in beneficial effect for the electrochemical performance of perovskites. Tabari et al. [281] prepared various $La_{1-x}Ca_xMnO_{3-\delta}$ perovskites to investigate the effect of Ca incorporation into the B-site of perovskite on the pseudocapacitive behavior. It showed that the capacitance decreased with the amount of incorporated Ca^{2+} into the $LaMnO_{3-\delta}$ structure. This effect is related to the formation of Mn^{4+}, which hindered the electron transfer in the structure. Thus, the capacitance of $La_{1-x}Ca_xMnO_{3-\delta}$ is smaller than that of $LaMnO_{3-\delta}$. In another study, instead, Mo et al. [26] believed that only excessive Ca doping into the $LaMnO_3$ could decrease the specific capacitance of perovskite electrode. More investigation is then needed to clarify this discrepancy.

Arjun et al. [282] investigated the effects of different cations (Mn, Fe, Cr, and Ni) in B-site on the oxygen-ion intercalation pseudocapacitance of perovskite oxide electrodes. Among these four perovskites, $LaNiO_3$ demonstrated the best performance. However, the cycle stability of $LaNiO_3$ reduced apparently, implying that material degradation of perovskite electrode is a big concern. The higher current density is also one of the secondary reasons for the reduced life span. The oxygen-ion intercalation pseudocapacitance of $LaNiO_3$ was also demonstrated by Che et al. [24] with a specific capacitance of about 480 F g^{-1} at 0.1 mV^{-1}. The mechanism of intercalation revealed that charge storage in this type of perovskite electrode was linked to the oxygen-ion intercalation into oxygen vacancies, primarily attributed to different valence states of Ni in B-site in perovskite. The $LaCoO_3$ perovskite nanoparticles could exhibit a specific capacitance of 200 F g^{-1} at 10 A g^{-1} and 246 F g^{-1} at 50 A g^{-1} [283]. Elsiddig et al. [284] prepared multiple $LaMn_{1\pm x}O_3$ perovskites by sol-gel method and studied their performance in SCs. The non-stoichiometric $LaMn_{1\cdot1}O_3$ sample demonstrated much larger specific capacity than stoichiometric $LaMnO_3$ perovskite. This

is because oxygen and cation vacancies, together with a high ratio of Mn^{4+}/Mn^{3+} are responsible for the electrochemical performance. George et al. [285] compared Co, Fe, and Ni dopants on the Mn sites in $SrMnO_3$ perovskite. Among them, $SrMn_{0.8}Co_{0.2}O_3$ exhibited the best performance with a capacitance of about 420 F g^{-1} at 0.5 A g^{-1}. This phenomenon may be ascribed to the easier valence change of cobalt under electrochemical condition than Fe and Ni. Alexander et al. [33] studied the influence of B-site elements (includes Fe, Mn, and Co) on the $La_{1-x}Sr_xBO_{3-\delta}$ perovskite electrode. Mn-doped oxide exhibited the highest specific capacitance than the Fe- and Co-doped ones. Xu et al. [27] synthesized a B-site cation-ordered double perovskite $Ba_2Bi_{0.1}Sc_{0.2}Co_{1.7}O_{6-\delta}$ as the electrode of SCs. It had a high oxygen vacancy concentration, as well as oxygen diffusion rate due to the low valence element doping and cation-ordering structure. Consequently, the highest capacitance of 1050 F g^{-1} was achieved at current density of 1 A g^{-1}. Alexander et al. [32] observed that replacing Ni with Fe in the B site of $LaNiO_3$ perovskite enhanced the $Ni^{2+}/^{3+}$ redox to higher potentials, whereas the inductive effect made the $Fe^{3+}/^{4+}$ redox peaks shifted to lower potentials. This strategy has the potential to prepare high voltage oxygen-ion intercalation-type pseudocapacitors. Thus, this electrode enjoyed a potential window of 1.8 V and the highest discharge voltage at 1.1 V.

Liu et al. [30] compared $SrCoO_{3-\delta}$ (SC) and $Ba_{0.5}Sr_{0.5}Co_{0.8}Fe_{0.2}O_{3-\delta}$ (BSCF) as the electrodes in oxygen-ion intercalation-type SC. Interestingly, they found that the cation leaching of BSCF led to an obvious change of specific area and cycling stability of electrode, giving rise to a higher surface area of BSCF and providing more active sites for electrochemical reaction. However, over-leaching of Ba^{2+} and Sr^{2+} can lead to the phase collapse of the perovskite structure. Further cycling testing demonstrated a substantial drop in capacitance for the BSCF electrode. Thus, to avoid over-leaching of compositional cations, it was critical to tailor the components appropriately to obtain a stable capacitance performance for perovskite oxides in the application of oxygen anion intercalation-type electrodes for SCs with alkaline solution electrolyte. Lang et al. [277] found that the leaching of Sr and Mn into the KOH electrolyte after a number of charge/discharge reaction led to the damage of perovskite structure and poor cycle stability. The Ca^{2+} and Mn^{2+} leaching in the $La_{0.5}Ca_{0.5}MnO_3$ perovskite during cycling testing were responsible for the significant decline in stability [26].

Although the oxygen intercalation process is a bulk mechanism, to some extent, higher surface area and porous structure can still enhance the electrochemical performance of perovskite electrodes. Guo et al. [286] used the polyvinylpyrrolidone as the additive to prohibit the growth of $LaCoO_3$ nanospheres via the solvothermal method. This electrode displayed an enhanced electrochemical performance and a specific capacitance of 203 F g^{-1} at 1 A g^{-1}, resulting from the synergistic effect of both size reduction and porous morphology. Li et al. [287] prepared a 2D perovskite $LaNiO_3$ nanosheets featured by hierarchical porous structure. It showed uniform sheet-like morphology with approximately 50-nm thick and high surface area and large pore volume. In the asymmetric SC testing, this electrode displayed a great energy density of 65.8 Wh kg^{-1} at 1.8 kW kg^{-1}, owing to more active sites for redox reaction and void space between the nanosheets. The same group also prepared $LaFeO_3$ nanotubes with a diameter of 25 nm, which showed a specific capacitance of 313.21 F g^{-1} at 0.8 A g^{-1} [23]. Hu et al. [288] prepared porous $CeMnO_3$ perovskite nanofibers with an excellent specific surface area of 103.9 m^2 g^{-1}. The specific capacitance of $CeMnO_3$ nanofibers was 160 F g^{-1} at 1 A g^{-1}. The porous structure enhanced the rate of ion transport and the high surface area accelerated the diffusion of electrolyte ion into perovskite. $SrTiO_3$ perovskite with excellent specific surface area was in the application of the electrode for solid-state SC. The cubic structure of $SrTiO_3$ is undeniably useful for SCs owing to its 3D diffusion channels for oxygen-anion diffusion (Fig. 18). It displayed a capacitance of 592 F g^{-1} at 5 mV s^{-1}, which was due to its large specific surface area, mesoporous structure, as well as excellent mass transfer rate of electrolytic ions [289].

The composite electrode of perovskite and other components have also attracted extensive attentions recently. To enhance the electrochemical performance of $LaMnO_3$ perovskite, Elsiddig et al. [290] introduced the reduced graphene oxide doped by nitrogen (N-rGO) into the $LaMnO_3$ to prepare the composite electrodes. The characteristics of the composite materials primarily depend on the amount of N-rGO. Compared with the pure graphene or $LaMnO_3$ perovskite, the composite electrode with 25% N-rGO exhibited the specific capacitance of 687 F g^{-1} at 5 mV s^{-1}. They believed that the synergistic effect between N-rGO and $LaMnO_3$ were beneficial for the overall electrochemical performance. Lang et al. [25]prepared a core-shell nanoflower materials consisting of $La_{0.85}Sr_{0.15}MnO_3$ and $NiCo_2O_4$, showing a capacitance of 1341 F g^{-1} at 0.5 A g^{-1}. However, this strategy does not improve the intrinsic properties of $La_{0.85}Sr_{0.15}MnO_3$ perovskite. Most of the capacitance should come from the contribution of $NiCo_2O_4$, which have a super high pseudocapacitance [291]. The $LaMnO_3$/rGO/PANI electrode in all solid-state SCs also demonstrated oxygen-ion intercalation pseudocapacitance, especially at lower current densities. This is because the electrolyte ions did not have sufficient time to intercalate/deintercalate into the deficient site in perovskite at higher current densities [292]. He et al. [293] fabricated a core/shell nanorods consisting of $La_{0.7}Sr_{0.3}CoO_3$ and MnO_2 as the electrode for SC. The core/shell structure not only provided a transport pathway for electrons but also allowed fast and reversible charge-discharge behavior. Thus, the electrolyte demonstrated a specific capacitance of 570 F g^{-1} at 1 A g^{-1}. Lang et al. [294] modified the $La_{0.85}Sr_{0.15}MnO_3$ perovskite by Ag nanoparticles, which acted as a highly conductive phase in the perovskite. Therefore, they not only accelerated charge transfer but also contributed to a small amount of pseudocapacitance.

In addition to the simple perovskite, there are multiple derivatives of perovskite including Ruddlesden-Popper (RP) oxides

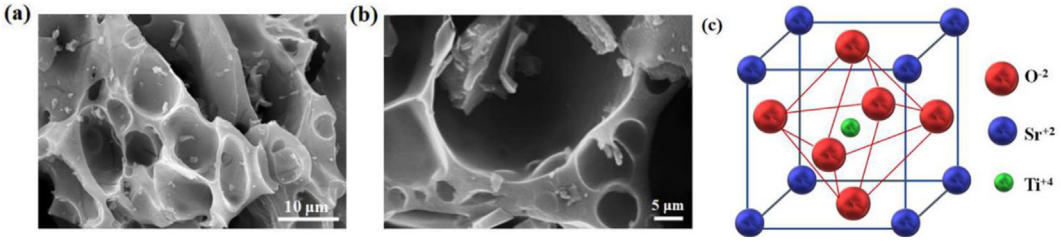

Fig. 18. (a, b) SEM images of $SrTiO_3$ at different microscales; (c) Idealized cubic crystal structure of $SrTiO_3$. Reprinted with permission from a study by Tomar et al. [289]. Copyright (2019) Elsevier B·V.

that have a crystal structure represented as $A_{n+1}B_nO_{3n+1}$ or equivalently $(AO)(ABO_{3+d})_n$, wherein n(BO_6) octahedra perovskite layers are separated by rock salt (AO)(OA) double layers. Some of these perovskite derivatives have also been investigated as oxygen-anion intercalative electrodes of SCs. Huang et al. [295] prepared a RP-type $LaSr_3Fe_3O_{10-\delta}$ in the application of oxygen-ion intercalation-type SCs. The high oxygen vacancy concentration in RP oxide facilitates the oxygen intercalation process. The oxidation state transformation of Fe may also make contribution to the pseudocapacitance. In a 6-M KOH electrolyte, $LaSr_3Fe_3O_{10-\delta}$ electrode demonstrated a specific capacitance of 233 F g^{-1}. The RP-type $La_2NiO_{4+\delta}$ oxide was also investigated as the electrode of pseudocapacitors. It delivered a capacitance of 657.4 F g^{-1} under 2 mV s^{-1} in 3-M KOH electrolyte. The electrochemical experiment indicated that the oxygen intercalation/deintercalation processes in RP-type $La_2NiO_{4+\delta}$ is associated with successive structure alternation of perovskite $LaNiO_3$ layers and LaO rock salt layers [296]. Forslund et al. [274] made a comparison between $CaMnO_{3-\delta}$ perovskite and $Ca_2MnO_{4-\delta}$ RP materials in terms of charge storage by anion intercalation. Interestingly, at high scan rates the measured capacitance of $CaMnO_{3-\delta}$ is significantly greater than that of $Ca_2MnO_{4-\delta}$ RP, whereas this trend reverses at low scan rates. This phenomenon can be explained by that a larger portion of the charge stored is due to diffusion-limited oxide anion intercalation into and out of the bulk material at lower scan rates. To improve conductivity and oxygen-ion diffusion rate in the $La_2NiO_{4+\delta}$ RP perovskite, Wei et al. [297] decorated the perovskite by Ag nanoparticles. Because Ag has the excellent electric conductivity, and is available for oxygen diffusion, Ag addition on $La_2NiO_{4+\delta}$ surface has positive effects on its performance. The coating of Ag on $La_2NiO_{4+\delta}$ surface improves the capacity and the cycling stability, which shows strong synergistic effect between Ag nanoparticles and $La_2NiO_{4+\delta}$.

In spite of the perovskite oxides, some other materials were also demonstrated to have the oxygen-ions intercalation pseudocapacitive behavior. Ajay et al. [298] found that the oxygen ions could intercalate into the $NiMoO_4$ in the form of OH^- and induced the pseudocapacitance. The CV test indicates that by lowering the scan rate, it is possible to increase OH^- intercalation/deintercalation reactions, contributing to an increase in the total capacitance of the electrode. It was found that the total contribution coming from the diffusion-controlled Faradaic processes and capacitive contribution was estimated to be 60–70% and 40–30%, respectively. Tao et al. [299] modified $Zn_xCo_{1-x}O$ by an atomic-level structure engineering method. This modification changed the primary charge-storage mechanism of $Zn_xCo_{1-x}O$ from surface-redox reactions to oxygen-ion intercalation into bulk material. The mechanism of oxygen intercalation in the bulk $Zn_xCo_{1-x}O$ can be described as:

$$Zn_xCo_{1-x}O_{1-\delta} + (2\delta + 2y)OH^- \leftrightarrow Zn_xCo_{1-x}O_{1+y} + 2(\delta + y)e^- + (\delta + y)H_2O$$

The DFT calculation revealed that numerous [110] facets on the surface of region of $Zn_xCo_{1-x}O$ enabled oxygen ions to intercalate easily into this oxide with a low energy barrier, and rapid electrical conduction was assured by Zn doping in atomic uniform. The obtained $Zn_xCo_{1-x}O$ exhibited high-rate performance with capacitance as high as 450 F g^{-1} at 1 V s^{-1} [299] (Table 3).

Table 3
Summary of electrode materials with anion intercalation pseudocapacitance.

Electrode materials	Synthesis method	Electrolyte	Capacity or capacitance	Potential range	Reference
$LaMnO_3$	Wet chemistry	6 M KOH	609.8 F g^{-1}	−1.2–0 V	[28]
$SrCo_{0.9}Nb_{0.1}O_{3-\delta}$	Sol-gel	6 M KOH	773.6 F g^{-1}	0–0.5 V	[22]
reduced $PrBaMn_2O_{6-\delta}$	Sol-gel	6 M KOH	1034.8 F g^{-1}	0–0.5 V	[31]
$CaMnO_{3-\delta}$	Sol-gel	1 M KOH	~220 F g^{-1}	−1.3–−0.1 V	[274]
$La_{0.85}Sr_{0.15}MnO_3$	Sol-gel	1 M KOH	198 F g^{-1}	−0.96–0.65 V	[276]
$LaMnO_3$	Sol-gel	1 M KOH	187 F g^{-1}	−0.96–0.65 V	[276]
$La_{1-x}Sr_xMnO_3$	Sol-gel	1 M KOH	102 F g^{-1}	−0.8–0.5 V	[277]
$PrBaCo_2O_{6-\delta}$	Sol-gel	6 M KOH	428.2 C g^{-1}	−0.1–0.55	[280]
$La_{0.5}Ca_{0.5}MnO_3$	Sol-gel	1 M KOH	170 F g^{-1}	−1–0.6 V	[26]
$LaNiO_3$	Sol-gel	3 M LiOH	106.6 F g^{-1}	−1–0 V	[282]
$LaCrO_3$	Sol-gel	3 M LiOH	24.4 F g^{-1}	−1–0 V	[282]
$LaFeO_3$	Sol-gel	3 M LiOH	16.4 F g^{-1}	−1–0 V	[282]
$LaMnO_3$	Sol-gel	3 M LiOH	56.8 F g^{-1}	−1–0 V	[282]
$LaNiO_{3-\delta}$	Sol-gel	1 M KOH	478.7 F g^{-1}	0–0.6 V	[24]
$LaCoO_3$	Wet chemistry	3 M KOH	299.6 F g^{-1}	0–0.5 V	[283]
$LaMn_{1\pm x}O_3$	Sol-gel	6 M KOH	727.6 C g^{-1}	−1–0.56 V	[284]
$La_{0.2}Sr_{0.8}MnO_{2.7}$	Sol-gel	1 M KOH	492 F g^{-1}	−0.6–0.4 V	[33]
$Ba_2Bi_{0.1}Sc_{0.2}Co_{1.7}O_{6-\delta}$	Sol-gel	6 M KOH	1050 F g^{-1}	0–0.5 V	[27]
$SrCoO_{3-\delta}$	Sol-gel	6 M KOH	572 F g^{-1}	0–0.5 V	[30]
$Ba_{0.5}Sr_{0.5}Co_{0.8}Fe_{0.2}O_{3-\delta}$	Sol-gel	6 M KOH	610 F g^{-1}	0–0.5 V	[30]
$La_{0.85}Sr_{0.15}MnO_3$	Sol-gel	1 M KOH	102 F g^{-1}	−0.8–0.5 V	[277]
$LaCoO_3$ nanospheres	Solvothermal method	6 M KOH	203 F g^{-1}	0–0.5 V	[286]
$LaNiO_3$	Sol-gel	6 M KOH	139.2 mAh g^{-1}	−0.09–0.36 V	[287]
$LaFeO_3$	Sol-gel	2 M KOH	313.2 F g^{-1}	0–0.5 V	[23]
$CeMnO_3$ nanofiber	Electrospinning	6 M KOH	159.6 F g^{-1}	−0.1–0.6 V	[288]
$SrTiO_3$	Sol-gel	3 M KOH	592 F g^{-1}	−0.2–0.6 V	[289]
$LaMnO_3$/N-rGO	Hydrothermal reaction	1 M KOH	687 F g^{-1}	−1–0.65 V	[290]
$La_{0.85}Sr_{0.15}MnO_3/NiCo_2O_4$	Wet chemistry	6 M KOH	1341 F g^{-1}	−0.2–0.5 V	[25]
$La_{0.7}Sr_{0.3}CoO_{3-\delta}/MnO_2$	Electrospinning	6 M KOH	630 F g^{-1}	0–0.5 V	[293]
$Ag/La_{0.85}Sr_{0.15}MnO_3$	Wet chemistry	N/A	186 F g^{-1}	−0.8–0.5 V	[294]
$LaSr_3Fe_3O_{10-\delta}$	Hydrothermal reaction	6 M KOH	380 F g^{-1}	0–0.35 V	[295]
$La_2NiO_{4+\delta}$	Sol-gel	3 M KOH	657.4 F g^{-1}	0–0.6 V	[296]
$Ca_2MnO_{4-\delta}$	Sol-gel	1 M KOH	310 F g^{-1}	−0.6–0.4 V	[274]
$Ag/La_2NiO_{4+\delta}$	Citrate method	1 M KOH	466.4 C g^{-1}	0–0.6 V	[297]
$NiMoO_4$	Microwave method	1 M KOH	1650 F g^{-1}	0–0.5 V	[298]
$Zn_xCo_{1-x}O$	Cation exchange method	6 M KOH	450 F g^{-1}	−1–−0.2 V	[299]

4. Conclusions

Intercalation pseudocapacitance that store energy through charge intercalation into the electrode bulk but in a behavior similar to a SC electrode based on surface-redox pseudocapacitance has received increasing importance during the past several years. The presence of intercalation pseudocapacitance in electrode materials could narrow the difference between LIBs and SCs from the aspects of both capacity and rate performance. Hence, intercalation pseudocapacitors may combine the advantages of batteries (high energy density) with that of SCs (high power density), and bridge the energy and power density gap between batteries and traditional pseudocapacitors. In addition, in some LIBs with nanostructured intercalation-type electrodes, the intercalation pseudocapacitance could also be appeared to a certain degree effectively improves the rate performance of the electrode, making the rate performance of LIB approaching that of SCs. For the intercalation pseudocapacitance, its electrochemical process is battery-like, that is, the reaction penetrates into the electrode bulk, whereas its electrochemical behavior takes after that of a SC, very fast reaction kinetics without phase transition during the reaction.

As to the charge carrier, both cation intercalation and anion intercalation pseudocapacitance could be appeared. For the cation intercalation pseudocapacitance, Li^+, Na^+, K^+, Mg^{2+}, and Al^{3+} were reported, while Li^+ and Na^+ are most popular. As to the anion intercalation, O^{2-} is the main charge species and very few cases, OH^-. The typical pseudocapacitive electrode materials have this property for the bulk materials and their electrode performance is less dependent on the specific surface area. RuO_2, MnO_2, B-TiO_2 and Nb_2O_5 are the well-known typical intercalation pseudocapacitive electrode materials. Some other materials only possess intercalation pseudocapacitive behavior when the particles are decreased to nanoscale. This type of materials can be found in more sophisticated electrode materials and materials with the surface mostly exposed to the electrolyte. Their performance is closely related to the electrode morphology. If the electrode is in bulk phase, the intercalation pseudocapacitance may not be appeared. Anyway, the kinetics in intercalation pseudocapacitance is limited by the surface process for these materials so that the entire behavior is capacitive-like.

A vital rule for the design of intercalation pseudocapacitive electrode materials is that the material should have a structure without experience phase transformations during the intercalation reaction. Furthermore, the unique crystal structure should allow cations to transport inside rapidly. Thus, the intercalation pseudocapacitance electrode materials usually contain open channels in their structure, which lower the energy barrier and promote the local charge transfer. In addition, reduce cation diffusion time can improve the rate performance of cation-intercalation pseudocapacitive electrode materials. Thus, although high specific surface area is not a necessary, it does help to improve the rate performance of intercalation pseudocapacitive electrode materials. For some intercalation pseudocapacitive electrode materials, such size effect is more prominent. Based on this, composite electrodes, consisting of oxides and conductive materials, like metal fibers or carbonaceous materials, have received great attentions in recent years in the application of high rate intercalation electrodes for pseudocapacitors. However, the effects of many factors, such as morphology, polymorph, doping, surface areas, and hierarchical structure, on pseudocapacitive lithium-ion storage have not been fully investigated, as well as the lithium-ion storage mechanism at the surface is not fully understood.

In addition to the pseudocapacitance induced by cations intercalation, oxygen anion intercalation pseudocapacitance was also observed in some perovskite oxides in aqueous alkaline solution. The capacitive charge storage in perovskite electrodes is penetrated into the bulk via filling oxygen vacancy sites. Therefore, high oxygen vacancy concentration is beneficial to improve the capacitance. However, excessive oxygen vacancy content may induce the damage or collapse of crystal structure, consequently causing a decrease or disappearance of anion intercalation pseudocapacitance. It is thus crucial to create the oxygen-deficient structure with appropriate oxygen vacancy concentration. It is well known that many perovskites are semiconductors with poor electrical conductivity. Further promotion of anion intercalation pseudocapacitance is restricted by low conductivity of perovskites, which is an intrinsic disadvantage. Typically, the perovskite oxide possesses the anion intercalation pseudocapacitance in the alkaline KOH electrolyte owing to the presence of OH^- ions that are readily accessible from electrolyte. It should be mentioned that some perovskite materials were reported to have anion intercalation pseudocapacitance in the neutral electrolyte of Na_2SO_4 in literature [278,279,281,285,300,301]. Because OH^- is required for realizing O^{2-} intercalation into the perovskite lattice while there is low OH^- concentration in neural solution, such pseudocapacitance may be resulted from the conventional surface Faradaic redox reaction instead of intercalation pseudocapacitance.

Some specific perovskites with unique crystal structure may further enhance the electrochemical performance. For example, the layered double perovskite with A-site ordering structure facilitate the diffusion of oxygen ion under the electrochemical condition. The stable crystalline structure of perovskite in the alkaline electrolyte solution is beneficial for the long-term cycling stability. Therefore, to develop highly capacitive perovskite-based electrodes for oxygen anion intercalation-type SCs, effective strategies, including detailed structural/electrochemical characterizations, calculation methods, and the fabrication techniques of practical SCs, should be realized to increase specific capacitance, long term operation stability, and energy and power densities. In addition, an increase in potential windows and specific capacitance will contribute to the enhancement of energy density.

Although highly promising for increasing the energy density of SCs and power density of LIBs, the materials that show intercalation pseudocapacitance behavior are still few, further research is urgently needed to develop alternative electrode materials that demonstrate superior intercalation pseudocapacitance performance over a wide range of conditions. On the other hand, the fundamental knowledge about intercalation pseudocapacitance need to be further exploited, and more efficient characterization techniques that can facilely distinguish the contribution of intercalation pseudocapacitance contribution to the total capacity is necessary.

Declaration of competing interest

The authors declare that they have no known competing financial interests or personal relationships that could have appeared to influence the work reported in this paper.

Acknowledgment

The work was supported by the Australian Research Council Discovery Project Grants DP150104365 and DP160104835.

References

[1] J.M. Tarascon, M. Armand, Issues and challenges facing rechargeable lithium batteries, Nature 414 (2001) 359–367.
[2] A. Patil, V. Patil, D. Wook Shin, J.-W. Choi, D.-S. Paik, S.-J. Yoon, Issue and challenges facing rechargeable thin film lithium batteries, Mater. Res. Bull. 43 (2008) 1913–1942.

[3] X. Shen, Y. Li, T. Qian, J. Liu, J. Zhou, C. Yan, J.B. Goodenough, Lithium anode stable in air for low-cost fabrication of a dendrite-free lithium battery, Nat. Commun. 10 (2019) 900.

[4] V. Augustyn, P. Simon, B. Dunn, Pseudocapacitive oxide materials for high-rate electrochemical energy storage, Energy Environ. Sci. 7 (2014) 1597–1614.

[5] K. Brezesinski, J. Wang, J. Haetge, C. Reitz, S.O. Steinmueller, S.H. Tolbert, B.M. Smarsly, B. Dunn, T. Brezesinski, Pseudocapacitive contributions to charge storage in highly ordered mesoporous group V transition metal oxides with iso-oriented layered nanocrystalline domains, J. Am. Chem. Soc. 132 (2010) 6982–6990.

[6] V. Augustyn, J. Come, M.A. Lowe, J.W. Kim, P.-L. Taberna, S.H. Tolbert, H.D. Abruña, P. Simon, B. Dunn, High-rate electrochemical energy storage through Li^+ intercalation pseudocapacitance, Nat. Mater. 12 (2013) 518–522.

[7] J.W. Kim, V. Augustyn, B. Dunn, The effect of crystallinity on the rapid pseudocapacitive response of Nb_2O_5, Adv. Energy Mater. 2 (2012) 141–148.

[8] T. Kudo, H. Obayashi, T. Gejo, Electrochemical behavior of the perovskite-type $Nd_{1-x}Sr_xCoO_3$ in an aqueous alkaline solution, J. Electrochem. Soc. 122 (1975) 159–163.

[9] B.E. Conway, Electrochemical Supercapacitors: Scientific Fundamentals and Technological Applications, Springer Science & Business Media, 2013.

[10] B.-Y. Chang, E. Ahn, S.-M. Park, Real-time staircase cyclic voltammetry fourier transform electrochemical impedance spectroscopic studies on underpotential deposition of lead on gold, J. Phys. Chem. C 112 (2008) 16902–16909.

[11] D. Rochefort, A.-L. Pont, Pseudocapacitive behaviour of RuO_2 in a proton exchange ionic liquid, Electrochem. Commun. 8 (2006) 1539–1543.

[12] J. Liu, J. Wang, C. Xu, H. Jiang, C. Li, L. Zhang, J. Lin, Z.X. Shen, Advanced energy storage devices: basic principles, analytical methods, and rational materials design, Adv. Sci. 5 (2018) 1700322.

[13] M. Wei, K. Wei, M. Ichihara, H. Zhou, Nb_2O_5 nanobelts: a lithium intercalation host with large capacity and high rate capability, Electrochem. Commun. 10 (2008) 980–983.

[14] C. Choi, D.S. Ashby, D.M. Butts, R.H. DeBlock, Q. Wei, J. Lau, B. Dunn, Achieving high energy density and high power density with pseudocapacitive materials, Nat. Rev. Mater. 5 (2019) 5–19.

[15] M. Okubo, E. Hosono, J. Kim, M. Enomoto, N. Kojima, T. Kudo, H. Zhou, I. Honma, Nanosize effect on high-rate Li-ion intercalation in $LiCoO_2$ electrode, J. Am. Chem. Soc. 129 (2007) 7444–7452.

[16] L. Cao, J. He, J. Li, J. Yan, J. Huang, Y. Qi, L. Feng, Surface tiny grain-dependent enhanced rate performance of MoO3 nanobelts with pseudocapacitance contribution for lithium-ion battery anode, J. Power Sources 392 (2018) 87–93.

[17] H. Lindström, S. Södergren, A. Solbrand, H. Rensmo, J. Hjelm, A. Hagfeldt, S.-E. Lindquist, Li^+ ion insertion in TiO_2 (anatase). 2. Voltammetry on nanoporous films, J. Phys. Chem. B 101 (1997) 7717–7722.

[18] M. Park, X. Zhang, M. Chung, G.B. Less, A.M. Sastry, A review of conduction phenomena in Li-ion batteries, J. Power Sources 195 (2010) 7904–7929.

[19] C. Chen, Y. Wen, X. Hu, X. Ji, M. Yan, L. Mai, P. Hu, B. Shan, Y. Huang, Na^+ intercalation pseudocapacitance in graphene-coupled titanium oxide enabling ultra-fast sodium storage and long-term cycling, Nat. Commun. 6 (2015) 6929.

[20] Y. Zhao, C. Han, J. Yang, J. Su, X. Xu, S. Li, L. Xu, R. Fang, H. Jiang, X. Zou, B. Song, L. Mai, Q. Zhang, Stable Alkali metal ion intercalation compounds as optimized metal oxide nanowire cathodes for lithium batteries, Nano Lett. 15 (2015) 2180–2185.

[21] A.A. Lubimtsev, P.R.C. Kent, B.G. Sumpter, P. Ganesh, Understanding the origin of high-rate intercalation pseudocapacitance in Nb_2O_5 crystals, J. Mater. Chem. 1 (2013) 14951–14956.

[22] L. Zhu, Y. Liu, C. Su, W. Zhou, M. Liu, Z. Shao, Perovskite $SrCo_{0.9}Nb_{0.1}O_{3-\delta}$ as an anion-intercalated electrode material for supercapacitors with ultrahigh volumetric energy density, Angew. Chem. 128 (2016) 9728–9731.

[23] Z. Li, W. Zhang, C. Yuan, Y. Su, Controlled synthesis of perovskite lanthanum ferrite nanotubes with excellent electrochemical properties, RSC Adv. 7 (2017) 12931–12937.

[24] W. Che, M. Wei, Z. Sang, Y. Ou, Y. Liu, J. Liu, Perovskite $LaNiO_{3-\delta}$ oxide as an anion-intercalated pseudocapacitor electrode, J. Alloys Compd. 731 (2018) 381–388.

[25] X. Lang, H. Zhang, X. Xue, C. Li, X. Sun, Z. Liu, H. Nan, X. Hu, H. Tian, Rational design of $La_{0.85}Sr_{0.15}MnO_3$@$NiCo_2O_4$ Core–Shell architecture supported on Ni foam for high performance supercapacitors, J. Power Sources 402 (2018) 213–220.

[26] H. Mo, H. Nan, X. Lang, S. Liu, L. Qiao, X. Hu, H. Tian, Influence of calcium doping on performance of $LaMnO_3$ supercapacitors, Ceram. Int. 44 (2018) 9733–9741.

[27] Z. Xu, Y. Liu, W. Zhou, M.O. Tade, Z. Shao, B-site cation-ordered double-perovskite oxide as an outstanding electrode material for supercapacitive energy storage based on the anion intercalation mechanism, ACS Appl. Mater. Interfaces 10 (2018) 9415–9423.

[28] J.T. Mefford, W.G. Hardin, S. Dai, K.P. Johnston, K.J. Stevenson, Anion charge storage through oxygen intercalation in $LaMnO_3$ perovskite pseudocapacitor electrodes, Nat. Mater. 13 (2014) 726–732.

[29] J. Sunarso, S.S. Hashim, N. Zhu, W. Zhou, Perovskite oxides applications in high temperature oxygen separation, solid oxide fuel cell and membrane reactor: a review, Prog. Energy Combust. Sci. 61 (2017) 57–77.

[30] Y. Liu, J. Dinh, M.O. Tade, Z. Shao, Design of perovskite oxides as anion-intercalation-type electrodes for supercapacitors: cation leaching effect, ACS Appl. Mater. Interfaces 8 (2016) 23774–23783.

[31] Y. Liu, Z. Wang, J.-P.M. Veder, Z. Xu, Y. Zhong, W. Zhou, M.O. Tade, S. Wang, Z. Shao, Highly defective layered double perovskite oxide for efficient energy storage via reversible pseudocapacitive oxygen-anion intercalation, Adv. Energy Mater. 8 (2018) 1702604.

[32] C.T. Alexander, R.P. Forslund, K.P. Johnston, K.J. Stevenson, Tuning redox transitions via the inductive effect in $LaNi_{1-x}Fe_xO_{3-\delta}$ perovskites for high-power asymmetric and symmetric pseudocapacitors, ACS Appl. Energy Mater. 2 (2019) 6558–6568.

[33] C.T. Alexander, J.T. Mefford, J. Saunders, R.P. Forslund, K.P. Johnston, K.J. Stevenson, Anion-based pseudocapacitance of the perovskite library $La_{1-x}Sr_xBO_{3-\delta}$ (B = Fe, Mn, Co), ACS Appl. Mater. Interfaces 11 (2019) 5084–5094.

[34] L. Kavan, M. Kalbáč, M. Zukalová, I. Exnar, V. Lorenzen, R. Nesper, M. Graetzel, Lithium storage in nanostructured TiO_2 made by hydrothermal growth, Chem. Mater. 16 (2004) 477–485.

[35] J. Li, Z. Tang, Z. Zhang, Preparation and novel lithium intercalation properties of titanium oxide nanotubes, Electrochem. Solid State Lett. 8 (2005) A316–A319.

[36] J. Wang, J. Polleux, T. Brezesinski, S. Tolbert, B. Dunn, Pseduocapacitive effects in nanostructured transition metal oxide materials, Meet. Abstr. MA2007-01 (2007), 116-116.

[37] J. Wang, J. Polleux, J. Lim, B. Dunn, Pseudocapacitive contributions to electrochemical energy storage in TiO_2 (anatase) nanoparticles, J. Phys. Chem. C 111 (2007) 14925–14931.

[38] J. Wang, J. Polleux, T. Brezesinski, S. Tolbert, B. Dunn, The pseudocapacitance behaviors of TiO_2 (anatase) nanoparticles, ECS Trans 11 (2008) 101–111.

[39] S. Huang, L. Zhang, X. Lu, L. Liu, L. Liu, X. Sun, Y. Yin, S. Oswald, Z. Zou, F. Ding, O.G. Schmidt, Tunable pseudocapacitance in 3D $TiO_{2-\delta}$ nanomembranes enabling superior lithium storage performance, ACS Nano 11 (2017) 821–830.

[40] H. Lindström, S. Södergren, A. Solbrand, H. Rensmo, J. Hjelm, A. Hagfeldt, S.-E. Lindquist, Li^+ ion insertion in TiO_2 (anatase). 1. Chronoamperometry on CVD films and nanoporous films, J. Phys. Chem. B 101 (1997) 7710–7716.

[41] M.V. Koudriachova, N.M. Harrison, S.W. de Leeuw, Effect of diffusion on lithium intercalation in titanium dioxide, Phys. Rev. Lett. 86 (2001) 1275–1278.

[42] M. Zukalová, M. Kalbáč, L. Kavan, I. Exnar, M. Graetzel, Pseudocapacitive lithium storage in TiO2(B), Chem. Mater. 17 (2005) 1248–1255.

[43] D. Panduwinata, J.D. Gale, A first principles investigation of lithium intercalation in TiO_2-B, J. Mater. Chem. 19 (2009) 3931–3940.

[44] M.V. Koudriachova, Role of the surface in Li insertion into nanowires of TiO_2-B, Surf. Interface Anal. 42 (2010) 1330–1332.

[45] C. Chen, Y. Mei, Y. Huang, X. Hu, Phase control of TiO_2 nanobelts by microwave irradiation as anode materials with tunable Li-diffusion kinetics, Mater. Res. Bull. 96 (2017) 365–371.

[46] X. Li, G. Wu, X. Liu, W. Li, M. Li, Orderly integration of porous TiO_2(B) nanosheets into bunchy hierarchical structure for high-rate and ultralong-lifespan lithium-ion batteries, Nanomater. Energy 31 (2017) 1–8.

[47] Y. Meng, D. Wang, Y. Wei, K. Zhu, Y. Zhao, X. Bian, F. Du, B. Liu, Y. Gao, G. Chen, Competition between insertion of Li^+ and Mg^{2+}: an example of TiO_2-B nanowires for Mg rechargeable batteries and Li^+/Mg^{2+} hybrid-ion batteries, J. Power Sources 346 (2017) 134–142.

[48] J. Kang, S.-H. Wei, K. Zhu, Y.-H. Kim, First-principles theory of electrochemical capacitance of nanostructured materials: dipole-assisted subsurface intercalation of lithium in pseudocapacitive TiO_2 anatase nanosheets, J. Phys. Chem. C 115 (2011) 4909–4915.

[49] T. Brezesinski, J. Wang, S.H. Tolbert, B. Dunn, Next generation pseudocapacitor materials from sol–gel derived transition metal oxides, J. Sol. Gel Sci. Technol. 57 (2011) 330–335.

[50] M.J. Sussman, A. Yasin, G.P. Demopoulos, On the complex interplay of crystallinity and surface area effects on Li-ion intercalation and pseudocapacitive storage properties of nanocrystalline anatase, J. Power Sources 272 (2014) 58–67.

[51] B. Hao, Y. Yan, X. Wang, G. Chen, Synthesis of anatase TiO_2 nanosheets with enhanced pseudocapacitive contribution for fast lithium storage, ACS Appl. Mater. Interfaces 5 (2013) 6285–6291.

[52] J. Qu, J.E. Cloud, Y. Yang, J. Ding, N. Yuan, Synthesis of nanoparticles-deposited double-walled TiO_2-B nanotubes with enhanced performance for lithium-ion batteries, ACS Appl. Mater. Interfaces 6 (2014) 22199–22208.

[53] J.-Y. Shin, D. Samuelis, J. Maier, Sustained lithium-storage performance of hierarchical, nanoporous anatase TiO_2 at high rates: emphasis on interfacial storage phenomena, Adv. Funct. Mater. 21 (2011) 3464–3472.

[54] W. Zhuang, L. Lu, W. Li, R. An, X. Feng, X. Wu, Y. Zhu, X. Lu, In-situ synthesized mesoporous TiO_2-B/anatase microparticles: improved anodes for lithium ion batteries, Chin. J. Chem. Eng. 23 (2015) 583–589.

[55] B. Saruhan, Y. Gönüllü, B. Arndt, Pseudocapacitive and hierarchically ordered porous electrode materials supercapacitors, in: Energy Harvesting and Storage: Materials, Devices, and Applications IV, 2013, pp. 872810–872811.

[56] M.J. Sussman, N. Brodusch, R. Gauvin, G.P. Demopoulos, Binder-free fabrication of nanotitania/carbon lithium-ion intercalation electrodes, J. Electrochem. Soc. 160 (2013) A3100–A3107.

[57] K. Hemalatha, A.S. Prakash, K. Guruprakash, M. Jayakumar, TiO_2 coated carbon nanotubes for electrochemical energy storage, J. Mater. Chem. 2 (2014) 1757–1766.

[58] E. Liu, J. Wang, C. Shi, N. Zhao, C. He, J. Li, J.-Z. Jiang, Anomalous interfacial lithium storage in graphene/TiO_2 for lithium ion batteries, ACS Appl. Mater. Interfaces 6 (2014) 18147–18151.

[59] S. Li, P. Xue, C. Lai, J. Qiu, M. Ling, S. Zhang, Pseudocapacitance of amorphous TiO_2@nitrogen doped graphene composite for high rate lithium storage, Electrochim. Acta 180 (2015) 112–119.

[60] C. Chen, B. Zhang, L. Miao, M. Yan, L. Mai, Y. Huang, X. Hu, Binding TiO_2-B nanosheets with N-doped carbon enables highly durable anodes for lithium-ion batteries, J. Mater. Chem. 4 (2016) 8172–8179.

[61] C. Senthil, T. Kesavan, A. Bhaumik, M. Yoshio, M. Sasidharan, Nitrogen rich carbon coated TiO_2 nanoparticles as anode for high performance lithium-ion battery, Electrochim. Acta 255 (2017) 417–427.

[62] M. Fehse, S. Cavaliere, P.E. Lippens, I. Savych, A. Iadecola, L. Monconduit, D.J. Jones, J. Rozière, F. Fischer, C. Tessier, L. Stievano, Nb-doped TiO_2 nanofibers for lithium ion batteries, J. Phys. Chem. C 117 (2013) 13827–13835.

[63] M. Lübke, J. Shin, P. Marchand, D. Brett, P. Shearing, Z. Liu, J.A. Darr, Highly pseudocapacitive Nb-doped TiO_2 high power anodes for lithium-ion batteries, J. Mater. Chem. 3 (2015) 22908–22914.

[64] Y. Liu, L. Lin, W. Zhang, M. Wei, Heterogeneous TiO_2@Nb_2O_5 composite as a high-performance anode for lithium-ion batteries, Sci. Rep. 7 (2017) 7204.

[65] S. Lou, X. Cheng, J. Gao, Q. Li, L. Wang, Y. Cao, Y. Ma, P. Zuo, Y. Gao, C. Du, H. Huo, G. Yin, Pseudocapacitive Li^+ intercalation in porous $Ti_2Nb_{10}O_{29}$ nanospheres enables ultra-fast lithium storage, Energy Storage Mater 11 (2018) 57–66.

[66] G. Hasegawa, A. Kitada, S. Kawasaki, K. Kanamori, K. Nakanishi, Y. Kobayashi, H. Kageyama, T. Abe, Impact of electrolyte on pseudocapacitance and stability of porous titanium nitride (TiN) monolithic electrode, J. Electrochem. Soc. 162 (2015) A77–A85.

[67] W. Wen, J.-M. Wu, Y.-Z. Jiang, L.-L. Lai, J. Song, Pseudocapacitance-enhanced Li-ion microbatteries derived by a TiN@TiO_2 nanowire anode, Inside Chem. 2 (2017) 404–416.

[68] B.E. Conway, Transition from "supercapacitor" to "battery" behavior in electrochemical energy storage, J. Electrochem. Soc. 138 (1991) 1539–1548.

[69] B.E. Conway, V. Birss, J. Wojtowicz, The role and utilization of pseudocapacitance for energy storage by supercapacitors, J. Power Sources 66 (1997) 1–14.

[70] G.A. Muller, J.B. Cook, H.-S. Kim, S.H. Tolbert, B. Dunn, High performance pseudocapacitor based on 2D layered metal chalcogenide nanocrystals, Nano Lett. 15 (2015) 1911–1917.

[71] J. Whiteley, S. Hafner, S.S. Han, S.C. Kim, V.-D. Le, C. Ban, Y.H. Kim, K.H. Oh, S.-H. Lee, All-solid-state disordered $LiTiS_2$ pseudocapacitor, J. Mater. Chem. 5 (2017) 15661–15668.

[72] Y. Wang, Z. Hong, M. Wei, Y. Xia, Layered $H_2Ti_6O_{13}$-nanowires: a new promising pseudocapacitive material in non-aqueous electrolyte, Adv. Funct. Mater. 22 (2012) 5185–5193.

[73] A. Byeon, M. Boota, M. Beidaghi, K.V. Aken, J.W. Lee, Y. Gogotsi, Effect of hydrogenation on performance of TiO_2(B) nanowire for lithium ion capacitors, Electrochem. Commun. 60 (2015) 199–203.

[74] M. Lübke, P. Marchand, D.J.L. Brett, P. Shearing, R. Gruar, Z. Liu, J.A. Darr, High power layered titanate nano-sheets as pseudocapacitive lithium-ion battery anodes, J. Power Sources 305 (2016) 115–121.

[75] J. Li, Z. Tang, Z. Zhang, Pseudocapacitive characteristic of lithium ion storage in hydrogen titanate nanotubes, Chem. Phys. Lett. 418 (2006) 506–510.

[76] R. Xu, J. Li, A. Tan, Z. Tang, Z. Zhang, Novel lithium titanate hydrate nanotubes with outstanding rate capabilities and long cycle life, J. Power Sources 196 (2011) 2283–2288.

[77] A.R. Armstrong, G. Armstrong, J. Canales, P.G. Bruce, TiO_2-B nanowires, Angew. Chem. Int. Ed. 43 (2004) 2286–2288.

[78] X.B. Ke, H.Y. Zhu, X.P. Gao, J.W. Liu, Z.F. Zheng, High-performance ceramic membranes with a separation layer of metal oxide nanofibers, Adv. Mater. 19 (2007) 785–790.

[79] R. Dominko, E. Baudrin, P. Umek, D. Arčon, M. Gaberšček, J. Jamnik, Reversible lithium insertion into $Na_2Ti_6O_{13}$ structure, Electrochem. Commun. 8 (2006) 673–677.

[80] M. Gracia, J.R. Gancedo, J.L. Gautier, J. de la Figuera, J.F. Marco, Influence of the manganese substitution on the cation distribution and magnetic structure of the spinel-related $LiFe_{1-x}Mn_{1+x}O_4$ ($x = 0.00, 0.25, 0.50, 0.75$) system, Hyperfine Interact. 240 (2019) 19.

[81] R. Chen, M. Knapp, M. Yavuz, S. Ren, R. Witte, R. Heinzmann, H. Hahn, H. Ehrenberg, S. Indris, Nanoscale spinel $LiFeTiO_4$ for intercalation pseudocapacitive Li^+ storage, Phys. Chem. Chem. Phys. 17 (2015) 1482–1488.

[82] B. Reichman, A.J. Bard, Electrochromism at niobium pentoxide electrodes in aqueous and acetonitrile solutions, J. Electrochem. Soc. 127 (1980) 241–242.

[83] B. Reichman, A.J. Bard, The application of Nb_2O_5 as a cathode in nonaqueous lithium cells, J. Electrochem. Soc. 128 (1981) 344–346.

[84] H.-L. Girard, B. Dunn, L. Pilon, Simulations and interpretation of three-electrode cyclic voltammograms of pseudocapacitive electrodes, Electrochim. Acta 211 (2016) 420–429.

[85] R. Kodama, Y. Terada, I. Nakai, S. Komaba, N. Kumagai, Electrochemical and in situ XAFS-XRD investigation of Nb_2O_5 for rechargeable lithium batteries, J. Electrochem. Soc. 153 (2006) A583–A588.

[86] J. Come, V. Augustyn, J.W. Kim, P. Rozier, P.-L. Taberna, P. Gogotsi, J.W. Long, B. Dunn, P. Simon, Electrochemical kinetics of nanostructured Nb_2O_5 electrodes, J. Electrochem. Soc. 161 (2014) A718–A725.

[87] N. Kumagai, Y. Tateshita, Y. Takatsuka, M. Baba, T. Ikeda, K. Tanno, Intercalation of lithium in r.f.-sputtered niobium oxide film as electrode material for lithium-ion batteries, J. Power Sources 54 (1995) 175–179.

[88] D. Chen, J.-H. Wang, T.-F. Chou, B. Zhao, M.A. El-Sayed, M. Liu, Unraveling the nature of anomalously fast energy storage in T-Nb_2O_5, J. Am. Chem. Soc. 139 (2017) 7071–7081.

[89] T. Ohzuku, K. Sawai, T. Hirai, Electrochemistry of L-niobium pentoxide a lithium/non-aqueous cell, J. Power Sources 19 (1987) 287–299.

[90] L. Kong, X. Cao, J. Wang, W. Qiao, L. Ling, D. Long, Revisiting Li^+ intercalation into various crystalline phases of Nb_2O_5 anchored on graphene sheets as pseudocapacitive electrodes, J. Power Sources 309 (2016) 42–49.

[91] K.J. Griffith, A.C. Forse, J.M. Griffin, C.P. Grey, High-rate intercalation without nanostructuring in metastable Nb_2O_5 bronze phases, J. Am. Chem. Soc. 138 (2016) 8888–8899.

[92] L. Kong, C. Zhang, J. Wang, D. Long, W. Qiao, L. Ling, Ultrahigh intercalation pseudocapacitance of mesoporous orthorhombic niobium pentoxide from a novel cellulose nanocrystal template, Mater. Chem. Phys. 149–150 (2015) 495–504.

[93] M. Liu, C. Yan, Y. Zhang, Fabrication of Nb_2O_5 nanosheets for high-rate lithium ion storage applications, Sci. Rep. 5 (2015) 8326.

[94] J.Y. Cheong, J.-W. Jung, D.-Y. Youn, C. Kim, S. Yu, S.-H. Cho, K.R. Yoon, I.-D. Kim, Mesoporous orthorhombic Nb_2O_5 nanofibers as pseudocapacitive electrodes with ultra-stable Li storage characteristics, J. Power Sources 360 (2017) 434–442.

[95] J. Zhang, H. Chen, X. Sun, X. Kang, Y. Zhang, C. Xu, Y. Zhang, High intercalation pseudocapacitance of free-standing T-Nb_2O_5 Nanowires@carbon cloth hybrid supercapacitor electrodes, J. Electrochem. Soc. 164 (2017) A820–A825.

[96] Z. Guangyu, Y. Chen, Z. Li, L. Changle, S. Kening, T -Nb_2O_5 quantum dots prepared by electrodeposition for fast Li ion intercalation/deintercalation, Nanotechnology 28 (2017) 215401.

[97] S. Lou, X. Cheng, L. Wang, J. Gao, Q. Li, Y. Ma, Y. Gao, P. Zuo, C. Du, G. Yin, High-rate capability of three-dimensionally ordered macroporous T-Nb_2O_5 through Li^+ intercalation pseudocapacitance, J. Power Sources 361 (2017) 80–86.

[98] J. Zhai, Y. Wu, X. Zhao, Q. Yang, Facile preparation of flower-like hierarchical Nb_2O_5 microspheres self-assembled by nanorod for high-power anodes in advanced hybrid supercapacitor, J. Alloys Compd. 715 (2017) 275–283.

[99] X. Wang, P.S. Lee, Titanium doped niobium oxide for stable pseudocapacitive lithium ion storage and its application in 3 V non-aqueous supercapacitors, J. Mater. Chem. 3 (2015) 21706–21712.

[100] S. Lou, X. Cheng, Y. Zhao, A. Lushington, J. Gao, Q. Li, P. Zuo, B. Wang, Y. Gao, Y. Ma, C. Du, G. Yin, X. Sun, Superior performance of ordered macroporous $TiNb_2O_7$ anodes for lithium ion batteries: understanding from the structural and pseudocapacitive insights on achieving high rate capability, Nanomater. Energy 34 (2017) 15–25.

[101] D. Cao, Z. Yao, J. Liu, J. Zhang, C. Li, H-Nb_2O_5 wired by tetragonal tungsten bronze related domains as high-rate anode for Li-ion batteries, Energy Storage Mater 11 (2018) 152–160.

[102] E. Lim, H. Kim, C. Jo, J. Chun, K. Ku, S. Kim, H.I. Lee, I.-S. Nam, S. Yoon, K. Kang, J. Lee, Advanced hybrid supercapacitor based on a mesoporous niobium pentoxide/carbon as high-performance anode, ACS Nano 8 (2014) 8968–8978.

[103] Y. Cai, X. Li, L. Wang, H. Gao, Y. Zhao, J. Ma, Oleylamine-assisted hydrothermal synthesis of ultrasmall NbO_x nanoparticles and their in situ conversion to NbO_x@C with highly reversible lithium storage, J. Mater. Chem. 3 (2015) 1396–1399.

[104] E. Lim, C. Jo, H. Kim, M.-H. Kim, Y. Mun, J. Chun, Y. Ye, J. Hwang, K.-S. Ha, K.C. Roh, K. Kang, S. Yoon, J. Lee, Facile synthesis of Nb_2O_5@Carbon core–shell nanocrystals with controlled crystalline structure for high-power anodes in hybrid supercapacitors, ACS Nano 9 (2015) 7497–7505.

[105] L. Kong, C. Zhang, J. Wang, W. Qiao, L. Ling, D. Long, Free-standing T-Nb_2O_5/graphene composite papers with ultrahigh gravimetric/volumetric capacitance for Li-ion intercalation pseudocapacitor, ACS Nano 9 (2015) 11200–11208.

[106] G. Ma, K. Li, Y. Li, B. Gao, T. Ding, Q. Zhong, J. Su, L. Gong, J. Chen, L. Yuan, B. Hu, J. Zhou, K. Huo, High-performance hybrid supercapacitor based on graphene-wrapped mesoporous T-Nb_2O_5 nanospheres anode and mesoporous carbon-coated graphene cathode, Chem. Electro. Chem 3 (2016) 1360–1368.

[107] L. Wang, B. Ruan, J. Xu, H.K. Liu, J. Ma, Amorphous carbon layer contributing Li storage capacity to Nb_2O_5@C nanosheets, RSC Adv. 5 (2015) 36104–36107.

[108] K. Kim, S.-G. Woo, Y.N. Jo, J. Lee, J.-H. Kim, Niobium oxide nanoparticle core–amorphous carbon shell structure for fast reversible lithium storage, Electrochim. Acta 240 (2017) 316–322.

[109] G. Luo, H. Li, D. Zhang, L. Gao, T. Lin, A template-free synthesis via alkaline route for Nb_2O_5/carbon nanotubes composite as pseudo-capacitor material with high-rate performance, Electrochim. Acta 235 (2017) 175–181.

[110] X. Wang, G. Li, R. Tjandra, X. Fan, X. Xiao, A. Yu, Fast lithium-ion storage of Nb_2O_5 nanocrystals in situ grown on carbon nanotubes for high-performance asymmetric supercapacitors, RSC Adv. 5 (2015) 41179–41185.

[111] X. Wang, C. Yan, J. Yan, A. Sumboja, P.S. Lee, Orthorhombic niobium oxide nanowires for next generation hybrid supercapacitor device, Nanomater. Energy 11 (2015) 765–772.

[112] C. Zhang, R. Maloney, M.R. Lukatskaya, M. Beidaghi, B. Dyatkin, E. Perre, D. Long, W. Qiao, B. Dunn, Y. Gogotsi, Synthesis and electrochemical properties of niobium pentoxide deposited on layered carbide-derived carbon, J. Power Sources 274 (2015) 121–129.

[113] C.-H. Lai, D. Ashby, M. Moz, Y. Gogotsi, L. Pilon, B. Dunn, Designing pseudocapacitance for Nb_2O_5/carbide-derived carbon electrodes and hybrid devices, Langmuir 33 (2017) 9407–9415.

[114] M.Y. Song, N.R. Kim, H.J. Yoon, S.Y. Cho, H.-J. Jin, Y.S. Yun, Long-lasting Nb_2O_5-based nanocomposite materials for Li-ion storage, ACS Appl. Mater. Interfaces 9 (2017) 2267–2274.

[115] C. Yang, Y. Zhang, F. Lv, C. Lin, Y. Liu, K. Wang, J. Feng, X. Wang, Y. Chen, J. Li, S. Guo, Porous $ZrNb_{24}O_{62}$ nanowires with pseudocapacitive behavior achieve high-performance lithium-ion storage, J. Mater. Chem. 5 (2017) 22297–22304.

[116] L. Kong, C. Zhang, J. Wang, W. Qiao, L. Ling, D. Long, Nanoarchitectured Nb_2O_5 hollow, Nb_2O_5@carbon and NbO_2@carbon core-shell microspheres for ultrahigh-rate intercalation pseudocapacitors, Sci. Rep. 6 (2016) 21177.

[117] C. Zhang, M. Beidaghi, M. Naguib, M.R. Lukatskaya, M.-Q. Zhao, B. Dyatkin, K.M. Cook, S.J. Kim, B. Eng, X. Xiao, D. Long, W. Qiao, B. Dunn, Y. Gogotsi, Synthesis and charge storage properties of hierarchical niobium pentoxide/carbon/niobium carbide (MXene) hybrid materials, Chem. Mater. 28 (2016) 3937–3943.

[118] C. Zhang, S.J. Kim, M. Ghidiu, M.-Q. Zhao, M.W. Barsoum, V. Nicolosi, Y. Gogotsi, Layered orthorhombic Nb_2O_5@$Nb_4C_3T_x$ and TiO_2@$Ti_3C_2T_x$ hierarchical composites for high performance Li-ion batteries, Adv. Funct. Mater. 26 (2016) 4143–4151.

[119] D. McNulty, D.N. Buckley, C. O'Dwyer, Comparative electrochemical charge storage properties of bulk and nanoscale vanadium oxide electrodes, J. Solid State Electrochem. 20 (2016) 1445–1458.

[120] A. Parija, Y. Liang, J.L. Andrews, L.R. De Jesus, D. Prendergast, S. Banerjee, Topochemically de-intercalated phases of V_2O_5 as cathode materials for multivalent intercalation batteries: a first-principles evaluation, Chem. Mater. 28 (2016) 5611–5620.

[121] K. Takahashi, S.J. Limmer, Y. Wang, G. Cao, Synthesis and electrochemical properties of single-crystal V_2O_5 nanorod arrays by template-based electrodeposition, J. Phys. Chem. B 108 (2004) 9795–9800.

[122] J.-M. Li, K.-H. Chang, C.-C. Hu, A novel vanadium oxide deposit for the cathode of asymmetric lithium-ion supercapacitors, Electrochem. Commun. 12 (2010) 1800–1803.

[123] H. Yin, C. Song, Y. Wang, S. Li, M. Zeng, Z. Zhang, Z. Zhu, K. Yu, Influence of morphologies and pseudocapacitive contributions for charge storage in V_2O_5 micro/nano-structures, Electrochim. Acta 111 (2013) 762–770.

[124] G. Wang, X. Lu, Y. Ling, T. Zhai, H. Wang, Y. Tong, Y. Li, LiCl/PVA gel electrolyte stabilizes vanadium oxide nanowire electrodes for pseudocapacitors, ACS Nano 6 (2012) 10296–10302.

[125] D. Wei, M.R.J. Scherer, C. Bower, P. Andrew, T. Ryhänen, U. Steiner, A nanostructured electrochromic supercapacitor, Nano Lett. 12 (2012) 1857–1862.

[126] J. Yang, T. Lan, J. Liu, Y. Song, M. Wei, Supercapacitor electrode of hollow spherical V_2O_5 with a high pseudocapacitance in aqueous solution, Electrochim. Acta 105 (2013) 489–495.

[127] I.E. Rauda, V. Augustyn, L.C. Saldarriaga-Lopez, X. Chen, L.T. Schelhas, G.W. Rubloff, B. Dunn, S.H. Tolbert, Nanostructured pseudocapacitors based on atomic layer deposition of V_2O_5 onto conductive nanocrystal-based mesoporous ITO scaffolds, Adv. Funct. Mater. 24 (2014) 6717–6728.

[128] E. Armstrong, D. McNulty, H. Geaney, C. O'Dwyer, Electrodeposited structurally stable V_2O_5 inverse opal networks as high performance thin film lithium batteries, ACS Appl. Mater. Interfaces 7 (2015) 27006–27015.

[129] Z. Tong, H. Xu, G. Liu, J. Zhao, Y. Li, Pseudocapacitive effect and Li^+ diffusion coefficient in three-dimensionally ordered macroporous vanadium oxide for energy storage, Electrochem. Commun. 69 (2016) 46–49.

[130] W. Dong, D.R. Rolison, B. Dunna, Electrochemical properties of high surface area vanadium oxide aerogels, Electrochem. Solid State Lett. 3 (2000) 457–459.

[131] V. Augustyn, B. Dunn, Vanadium oxide aerogels: nanostructured materials for enhanced energy storage, C. R. Chim. 13 (2010) 130–141.

[132] S. Passerini, J.J. Ressler, D.B. Le, B.B. Owens, W.H. Smyrl, High rate electrodes of V_2O_5 aerogel, Electrochim. Acta 44 (1999) 2209–2217.

[133] I.-H. Kim, J.-H. Kim, B.-W. Cho, K.-B. Kim, Pseudocapacitive properties of electrochemically prepared vanadium oxide on carbon nanotube film substrate, J. Electrochem. Soc. 153 (2006) A1451–A1458.

[134] S.D. Perera, B. Patel, N. Nijem, K. Roodenko, O. Seitz, J.P. Ferraris, Y.J. Chabal, K.J. Balkus, Vanadium oxide nanowire–carbon nanotube binder-free flexible electrodes for supercapacitors, Adv. Energy Mater. 1 (2011) 936–945.

[135] M. Sathiya, A.S. Prakash, K. Ramesha, J.M. Tarascon, A.K. Shukla, V_2O_5-Anchored carbon nanotubes for enhanced electrochemical energy storage, J. Am. Chem. Soc. 133 (2011) 16291–16299.

[136] C. Zhang, S.-H. Park, S.E. O'Brien, A. Seral-Ascaso, M. Liang, D. Hanlon, D. Krishnan, A. Crossley, N. McEvoy, J.N. Coleman, V. Nicolosi, Liquid exfoliation of interlayer spacing-tunable 2D vanadium oxide nanosheets: high capacity and rate handling Li-ion battery cathodes, Nanomater. Energy 39 (2017) 151–161.

[137] S. Fleischmann, M. Zeiger, N. Jackel, B. Kruner, V. Lemkova, M. Widmaier, V. Presser, Tuning pseudocapacitive and battery-like lithium intercalation in vanadium dioxide/carbon onion hybrids for asymmetric supercapacitor anodes, J. Mater. Chem. 5 (2017) 13039–13051.

[138] S. Fleischmann, D. Leistenschneider, V. Lemkova, B. Krüner, M. Zeiger, L. Borchardt, V. Presser, Tailored mesoporous carbon/vanadium pentoxide hybrid electrodes for high power pseudocapacitive lithium and sodium intercalation, Chem. Mater. 29 (2017) 8653–8662.

[139] G. Ren, M.N.F. Hoque, X. Pan, J. Warzywoda, Z. Fan, Vertically aligned VO_2(B) nanobelt forest and its three-dimensional structure on oriented graphene for energy storage, J. Mater. Chem. 3 (2015) 10787–10794.

[140] L. Zhang, K. Zhao, Y. Luo, Y. Dong, W. Xu, M. Yan, W. Ren, L. Zhou, L. Qu, L. Mai, Acetylene black induced heterogeneous growth of macroporous CoV_2O_6 nanosheet for high-rate pseudocapacitive lithium-ion battery anode, ACS Appl. Mater. Interfaces 8 (2016) 7139–7146.

[141] H. Heli, H. Yadegari, A. Jabbari, Investigation of the lithium intercalation behavior of nanosheets of LiV_3O_8 in an aqueous solution, J. Phys. Chem. C 115 (2011) 10889–10897.

[142] L. Shen, H. Lv, S. Chen, P. Kopold, P.A. van Aken, X. Wu, J. Maier, Y. Yu, Peapod-like Li_3VO_4/N-doped carbon nanowires with pseudocapacitive properties as advanced materials for high-energy lithium-ion capacitors, Adv. Mater. 29 (2017) 1700142.

[143] N.T. Hong Trang, N. Lingappan, I. Shakir, D.J. Kang, Growth of single-crystalline β-$Na_{0.33}V_2O_5$ nanowires on conducting substrate: a binder-free electrode for energy storage devices, J. Power Sources 251 (2014) 237–242.

[144] X. Ji, K. Xu, C. Chen, B. Zhang, H. Wan, Y. Ruan, L. Miao, J. Jiang, Different charge-storage mechanisms in disulfide vanadium and vanadium carbide monolayer, J. Mater. Chem. 3 (2015) 9909–9914.

[145] Y. Zhu, L. Peng, D. Chen, G. Yu, Intercalation pseudocapacitance in ultrathin $VOPO_4$ nanosheets: toward high-rate alkali-ion-based electrochemical energy storage, Nano Lett. 16 (2016) 742–747.

[146] H. Hareendrakrishnakumar, R. Chulliyote, M.G. Joseph, Effect of crystallite size on the intercalation pseudocapacitance of lithium nickel vanadate in aqueous electrolyte, J. Solid State Electrochem. 22 (2017) 1–9.

[147] T. Brezesinski, J. Wang, S.H. Tolbert, B. Dunn, Ordered mesoporous α-MoO_3 with iso-oriented nanocrystalline walls for thin-film pseudocapacitors, Nat. Mater. 9 (2010) 146.

[148] D. Guan, J. Li, X. Gao, C. Yuan, Effects of amorphous and crystalline MoO_3 coatings on the Li-ion insertion behavior of a TiO_2 nanotube anode for lithium ion batteries, RSC Adv. 4 (2014) 4055–4062.

[149] L. Can, L. Zhengcao, Z. Zhengjun, MoO_x thin films deposited by magnetron sputtering as an anode for aqueous micro-supercapacitors, Sci. Technol. Adv. Mater. 14 (2013), 065005.

[150] J. Jiang, J. Liu, S. Peng, D. Qian, D. Luo, Q. Wang, Z. Tian, Y. Liu, Facile synthesis of α-MoO_3 nanobelts and their pseudocapacitive behavior in an aqueous Li_2SO_4 solution, J. Mater. Chem. 1 (2013) 2588–2594.

[151] H.-S. Kim, J.B. Cook, H. Lin, Jesse S. Ko, Sarah H. Tolbert, V. Ozolins, B. Dunn, Oxygen vacancies enhance pseudocapacitive charge storage properties of MoO_{3-x}, Nat. Mater. 16 (2016) 454.

[152] J. Chen, S. Han, H. Zhao, J. Bai, L. Wang, G. Sun, Z. Zhang, X. Pan, J. Zhou, E. Xie, Robust wire-based supercapacitors based on hierarchical α-MoO_3 nanosheet arrays with well-aligned laminated structure, Chem. Eng. J. 320 (2017) 34–42.

[153] B. Mendoza-Sánchez, P.S. Grant, Charge storage properties of a α-MoO_3/carboxyl-functionalized single-walled carbon nanotube composite electrode in a Li ion electrolyte, Electrochim. Acta 98 (2013) 294–302.

[154] X. Xiao, Z. Peng, C. Chen, C. Zhang, M. Beidaghi, Z. Yang, N. Wu, Y. Huang, L. Miao, Y. Gogotsi, J. Zhou, Freestanding MoO_{3-x} nanobelt/carbon nanotube films for Li-ion intercalation pseudocapacitors, Nanomater. Energy 9 (2014) 355–363.

[155] I. Shakir, M. Shahid, S. Cherevko, C.-H. Chung, D.J. Kang, Ultrahigh-energy and stable supercapacitors based on intertwined porous MoO_3–MWCNT nanocomposites, Electrochim. Acta 58 (2011) 76–80.

[156] L.S. Aravinda, U. Bhat, B. Ramachandra Bhat, Binder free MoO_3/multiwalled carbon nanotube thin film electrode for high energy density supercapacitors, Electrochim. Acta 112 (2013) 663–669.

[157] X. Li, J. Shao, J. Li, L. Zhang, Q. Qu, H. Zheng, Ordered mesoporous MoO_2 as a high-performance anode material for aqueous supercapacitors, J. Power Sources 237 (2013) 80–83.

[158] H.-S. Kim, J.B. Cook, S.H. Tolbert, B. Dunn, The development of pseudocapacitive properties in nanosized-MoO_2, J. Electrochem. Soc. 162 (2015) A5083–A5090.

[159] S. Petnikota, K.W. Teo, L. Chen, A. Sim, S.K. Marka, M.V. Reddy, V.V.S.S. Srikanth, S. Adams, B.V.R. Chowdari, Exfoliated graphene oxide/MoO_2 composites as anode materials in lithium-ion batteries: an insight into intercalation of Li and conversion mechanism of MoO_2, ACS Appl. Mater. Interfaces 8 (2016) 10884–10896.

[160] K.M. Hercule, Q. Wei, O.K. Asare, L. Qu, A.M. Khan, M. Yan, C. Du, W. Chen, L. Mai, Interconnected nanorods–nanoflakes $Li_2Co_2(MoO_4)_3$ framework structure with enhanced electrochemical properties for supercapacitors, Adv. Energy Mater. 5 (2015) 1500060.

[161] F.C. Laman, K. Brandt, Effect of discharge current on cycle life of a rechargeable lithium battery, J. Power Sources 24 (1988) 195–206.

[162] M. Acerce, D. Voiry, M. Chhowalla, Metallic 1T phase MoS_2 nanosheets as supercapacitor electrode materials, Nat. Nanotechnol. 10 (2015) 313–318.

[163] J.B. Cook, H.-S. Kim, Y. Yan, J.S. Ko, S. Robbennolt, B. Dunn, S.H. Tolbert, Mesoporous MoS_2 as a transition metal dichalcogenide exhibiting pseudocapacitive Li and Na-ion charge storage, Advanced Energy Materials 6 (2016) 1501937.

[164] H.D. Yoo, Y. Li, Y. Liang, Y. Lan, F. Wang, Y. Yao, Intercalation pseudocapacitance of exfoliated molybdenum disulfide for ultrafast energy storage, Chem. Nano. Mat 2 (2016) 688–691.

[165] J.B. Cook, H.-S. Kim, T.C. Lin, C.-H. Lai, B. Dunn, S.H. Tolbert, Pseudocapacitive charge storage in thick composite MoS_2 nanocrystal-based electrodes, Adv. Energy Mater. 7 (2017) 1601283.

[166] R. Wang, S. Wang, D. Jin, Y. Zhang, Y. Cai, J. Ma, L. Zhang, Engineering layer structure of MoS_2-graphene composites with robust and fast lithium storage for high-performance Li-ion capacitors, Energy Storage Mater 9 (2017) 195–205.

[167] S.-E. Chun, S.-I. Pyun, G.-J. Lee, A study on mechanism of charging/discharging at amorphous manganese oxide electrode in 0.1M Na_2SO_4 solution, Electrochim. Acta 51 (2006) 6479–6486.

[168] S.-L. Kuo, N.-L. Wu, Investigation of pseudocapacitive charge-storage reaction of MnO2 · nH2O supercapacitors in aqueous electrolytes, J. Electrochem. Soc. 153 (2006) A1317–A1324.

[169] J. Ni, W. Lu, L. Zhang, B. Yue, X. Shang, Y. Lv, Low-temperature synthesis of monodisperse 3D manganese oxide nanoflowers and their pseudocapacitance properties, J. Phys. Chem. C 113 (2009) 54–60.

[170] P. Xiong, R. Ma, N. Sakai, X. Bai, S. Li, T. Sasaki, Redox active cation intercalation/deintercalation in two-dimensional layered MnO_2 nanostructures for high-rate electrochemical energy storage, ACS Appl. Mater. Interfaces 9 (2017) 6282–6291.

[171] C.R. Arias, C. Debiemme-Chouvy, C. Gabrielli, C. Laberty-Robert, A. Pailleret, H. Perrot, O. Sel, New insights into pseudocapacitive charge-storage mechanisms in Li-birnessite type MnO_2 monitored by fast quartz crystal microbalance methods, J. Phys. Chem. C 118 (2014) 26551–26559.

[172] I.I. Misnon, R.A. Aziz, N.K.M. Zain, B. Vidhyadharan, S.G. Krishnan, R. Jose, High performance MnO_2 nanoflower electrode and the relationship between solvated ion size and specific capacitance in highly conductive electrolytes, Mater. Res. Bull. 57 (2014) 221–230.

[173] D. Chen, D. Ding, X. Li, G.H. Waller, X. Xiong, M.A. El-Sayed, M. Liu, Probing the charge storage mechanism of a pseudocapacitive MnO_2 electrode using in operando Raman spectroscopy, Chem. Mater. 27 (2015) 6608–6619.

[174] J. Liu, J. Jiang, C. Cheng, H. Li, J. Zhang, H. Gong, H.J. Fan, Co_3O_4 nanowire@MnO_2 ultrathin nanosheet core/shell arrays: a new class of high-performance pseudocapacitive materials, Adv. Mater. 23 (2011) 2076–2081.

[175] S. Chen, J. Zhu, X. Wu, Q. Han, X. Wang, Graphene Oxide–MnO_2 nanocomposites for supercapacitors, ACS Nano 4 (2010) 2822–2830.

[176] J. Liu, J. Essner, J. Li, Hybrid supercapacitor based on coaxially coated manganese oxide on vertically aligned carbon nanofiber arrays, Chem. Mater. 22 (2010) 5022–5030.

[177] W. Yan, J.Y. Kim, W. Xing, K.C. Donavan, T. Ayvazian, R.M. Penner, Lithographically patterned gold/manganese dioxide core/shell nanowires for high capacity, high rate, and high cyclability hybrid electrical energy storage, Chem. Mater. 24 (2012) 2382–2390.

[178] Y. Wang, A. Yuan, X. Wang, Pseudocapacitive behaviors of nanostructured manganese dioxide/carbon nanotubes composite electrodes in mild aqueous electrolytes: effects of electrolytes and current collectors, J. Solid State Electrochem. 12 (2008) 1101–1107.

[179] M.S. Javed, X. Han, C. Hu, M. Zhou, Z. Huang, X. Tang, X. Gu, Tracking pseudocapacitive contribution to superior energy storage of MnS nanoparticles grown on carbon textile, ACS Appl. Mater. Interfaces 8 (2016) 24621–24628.

[180] M. Mohamedi, M. Makino, K. Dokko, T. Itoh, I. Uchida, Electrochemical investigation of $LiNi_{0.5}Mn_{1.5}O_4$ thin film intercalation electrodes, Electrochim. Acta 48 (2002) 79–84.

[181] G. Wang, M. Qu, Z. Yu, R. Yuan, $LiNi_{0.8}Co_{0.2}O_2$/MWCNT composite electrodes for supercapacitors, Mater. Chem. Phys. 105 (2007) 169–174.

[182] K.B. Gandrud, O. Nilsen, H. Fjellvåg, Ultra-high power capabilities in amorphous $FePO_4$ thin films, J. Power Sources 306 (2016) 454–458.

[183] Y. Wang, D. Zhao, R. Che, Y. Xia, Pseudo-capacitive profile vs. Li-intercalation in nano-$LiFePO_4$, J. Power Sources 236 (2013) 230–237.

[184] K. Kisu, E. Iwama, W. Naoi, P. Simon, K. Naoi, Electrochemical kinetics of nanostructure $LiFePO_4$/graphitic carbon electrodes, Electrochem. Commun. 72 (2016) 10–14.

[185] R. Li, J. Liu, Mechanistic investigation of the charge storage process of pseudocapacitive Fe_3O_4 nanorod film, Electrochim. Acta 120 (2014) 52–56.

[186] Q. Li, H. Zhang, S. Lou, Y. Qu, P. Zuo, Y. Ma, X. Cheng, C. Du, Y. Gao, G. Yin, Pseudocapacitive Li^+ intercalation in ZnO/ZnO@C composites enables high-rate lithium-ion storage and stable cyclability, Ceram. Int. 43 (2017) 11998–12004.

[187] L. Wu, J. Lang, S. Wang, P. Zhang, X. Yan, Study of Ni-dopped $MnCo_2O_4$ yolk-shell submicron-spheres with fast Li^+ intercalation pseudocapacitance as an anode for high-performance lithium ion batteries, Electrochim. Acta 203 (2016) 128–135.

[188] M.S. Javed, Z. Jiang, C. Zhang, L. Chen, C. Hu, X. Gu, A high-performance flexible solid-state supercapacitor based on Li-ion intercalation into tunnel-structure iron sulfide, Electrochim. Acta 219 (2016) 742–750.

[189] Q. Lian, G. Zhou, J. Liu, C. Wu, W. Wei, L. Chen, C. Li, Extrinsic pseudocapacitve Li-ion storage of SnS anode via lithiation-induced structural optimization on cycling, J. Power Sources 366 (2017) 1–8.

[190] B. Long, M.-S. Balogun, L. Luo, W. Qiu, Y. Luo, S. Song, Y. Tong, Phase boundary derived pseudocapacitance enhanced nickel-based composites for electrochemical energy storage devices, Adv. Energy Mater. (2017) 1701681.

[191] C. Li, X. Hu, X. Lou, L. Zhang, Y. Wang, J.-P. Amoureux, M. Shen, Q. Chen, B. Hu, The organic-moiety-dominated Li^+ intercalation/deintercalation mechanism of a cobalt-based metal-organic framework, J. Mater. Chem. 4 (2016) 16245–16251.

[192] K.-T. Kim, G. Ali, K.Y. Chung, C.S. Yoon, H. Yashiro, Y.-K. Sun, J. Lu, K. Amine, S.-T. Myung, Anatase titania nanorods as an intercalation anode material for rechargeable sodium batteries, Nano Lett. 14 (2014) 416–422.

[193] Q. Qu, P. Zhang, B. Wang, Y. Chen, S. Tian, Y. Wu, R. Holze, Electrochemical performance of MnO_2 nanorods in neutral aqueous electrolytes as a cathode for asymmetric supercapacitors, J. Phys. Chem. C 113 (2009) 14020–14027.

[194] R. Inoue, Y. Nakashima, K. Tomono, M. Nakayama, Electrically rearranged birnessite-type MnO_2 by repetitive potential steps and its pseudocapacitive properties, J. Electrochem. Soc. 159 (2012) A445–A451.

[195] M.N. Patel, X. Wang, D.A. Slanac, D.A. Ferrer, S. Dai, K.P. Johnston, K.J. Stevenson, High pseudocapacitance of MnO_2 nanoparticles in graphitic disordered mesoporous carbon at high scan rates, J. Mater. Chem. 22 (2012) 3160–3169.

[196] S. Ardizzone, G. Fregonara, S. Trasatti, "Inner" and "outer" active surface of RuO_2 electrodes, Electrochim. Acta 35 (1990) 263–267.

[197] A. Zolfaghari, F. Ataherian, M. Ghaemi, A. Gholami, Capacitive behavior of nanostructured MnO_2 prepared by sonochemistry method, Electrochim, Acta 52 (2007) 2806–2814.

[198] M.J. Young, A.M. Holder, S.M. George, C.B. Musgrave, Charge storage in cation incorporated α-MnO_2, Chem. Mater. 27 (2015) 1172–1180.

[199] A. Sumboja, U.M. Tefashe, G. Wittstock, P.S. Lee, Monitoring electroactive ions at manganese dioxide pseudocapacitive electrodes with scanning electrochemical microscope for supercapacitor electrodes, J. Power Sources 207 (2012) 205–211.

[200] M. Ghaemi, F. Ataherian, A. Zolfaghari, S.M. Jafari, Charge storage mechanism of sonochemically prepared MnO_2 as supercapacitor electrode: effects of physisorbed water and proton conduction, Electrochim. Acta 53 (2008) 4607–4614.

[201] J.F. Whitacre, T. Wiley, S. Shanbhag, Y. Wenzhuo, A. Mohamed, S.E. Chun, E. Weber, D. Blackwood, E. Lynch-Bell, J. Gulakowski, C. Smith, D. Humphreys, An aqueous electrolyte, sodium ion functional, large format energy storage device for stationary applications, J. Power Sources 213 (2012) 255–264.

[202] L. Yang, S. Cheng, X. Ji, Y. Jiang, J. Zhou, M. Liu, Investigations into the origin of pseudocapacitive behavior of Mn_3O_4 electrodes using in operando Raman spectroscopy, J. Mater. Chem. 3 (2015) 7338–7344.

[203] L. Yang, S. Cheng, J. Wang, X. Ji, Y. Jiang, M. Yao, P. Wu, M. Wang, J. Zhou, M. Liu, Investigation into the origin of high stability of δ-MnO_2 pseudocapacitive electrode using operando Raman spectroscopy, Nanomater. Energy 30 (2016) 293–302.

[204] M. Yeager, W. Du, R. Si, D. Su, N. Marinković, X. Teng, Highly efficient $K_{0.15}MnO_2$ birnessite nanosheets for stable pseudocapacitive cathodes, J. Phys. Chem. C 116 (2012) 20173–20181.

[205] A.A. Radhiyah, M. Izan Izwan, V. Baiju, C. Kwok Feng, I. Jamil, R. Jose, Doubling of electrochemical parameters via the pre-intercalation of Na^+ in layered MnO_2 nanoflakes compared to α-MnO_2 nanorods, RSC Adv. 5 (2015) 9667–9673.

[206] Q. Lu, Y. Zhou, Synthesis of mesoporous polythiophene/MnO_2 nanocomposite and its enhanced pseudocapacitive properties, J. Power Sources 196 (2011) 4088–4094.

[207] Y. Huang, Y. Li, Z. Hu, G. Wei, J. Guo, J. Liu, A carbon modified MnO_2 nanosheet array as a stable high-capacitance supercapacitor electrode, J. Mater. Chem. 1 (2013) 9809–9813.

[208] C.J. Hung, P. Lin, T.Y. Tseng, Electrophoretic fabrication and pseudocapacitive properties of graphene/manganese oxide/carbon nanotube nanocomposites, J. Power Sources 243 (2013) 594–602.

[209] M.S. Kolathodi, S.N. Hanumantha Rao, T.S. Natarajan, G. Singh, Beaded manganese oxide (Mn_2O_3) nanofibers: preparation and application for capacitive energy storage, J. Mater. Chem. 4 (2016) 7883–7891.

[210] J. Chen, G. Zou, H. Hou, Y. Zhang, Z. Huang, X. Ji, Pinecone-like hierarchical anatase TiO_2 bonded with carbon enabling ultrahigh cycling rates for sodium storage, J. Mater. Chem. 4 (2016) 12591–12601.

[211] Z. Le, F. Liu, P. Nie, X. Li, X. Liu, Z. Bian, G. Chen, H.B. Wu, Y. Lu, Pseudocapacitive sodium storage in mesoporous single-crystal-like TiO_2–graphene nanocomposite enables high-performance sodium-ion capacitors, ACS Nano 11 (2017) 2952–2960.

[212] H. He, Q. Zhang, H. Wang, H. Zhang, J. Li, Z. Peng, Y. Tang, M. Shao, Defect-rich $TiO_{2-\delta}$ nanocrystals confined in a mooncake-shaped porous carbon matrix as an advanced Na ion battery anode, J. Power Sources 354 (2017) 179–188.

[213] P. Yu, C. Li, X. Guo, Sodium storage and pseudocapacitive charge in textured $Li_4Ti_5O_{12}$ thin films, J. Phys. Chem. C 118 (2014) 10616–10624.

[214] L.Y. Yang, H.Z. Li, J. Liu, S.S. Tang, Y.K. Lu, S.T. Li, J. Min, N. Yan, M. Lei, $Li_4Ti_5O_{12}$ nanosheets as high-rate and long-life anode materials for sodium-ion batteries, J. Mater. Chem. 3 (2015) 24446–24452.

[215] C. Chen, H. Xu, T. Zhou, Z. Guo, L. Chen, M. Yan, L. Mai, P. Hu, S. Cheng, Y. Huang, J. Xie, Integrated intercalation-based and interfacial sodium storage in graphene-wrapped porous $Li_4Ti_5O_{12}$ nanofibers composite aerogel, Adv. Energy Mater. 6 (2016) 1600322.

[216] G. Xu, L. Yang, X. Wei, J. Ding, J. Zhong, P.K. Chu, MoS_2-Quantum-Dot-Interspersed $Li_4Ti_5O_{12}$ nanosheets with enhanced performance for Li- and Na-ion batteries, Adv. Funct. Mater. 26 (2016) 3349–3358.

[217] S. Dong, L. Shen, H. Li, P. Nie, Y. Zhu, Q. Sheng, X. Zhang, Pseudocapacitive behaviours of $Na_2Ti_3O_7$@CNT coaxial nanocables for high-performance sodium-ion capacitors, J. Mater. Chem. 3 (2015) 21277–21283.

[218] S. Fu, J. Ni, Y. Xu, Q. Zhang, L. Li, Hydrogenation driven conductive $Na_2Ti_3O_7$ nanoarrays as robust binder-free anodes for sodium-ion batteries, Nano Lett. 16 (2016) 4544–4551.

[219] J. Ni, S. Fu, C. Wu, Y. Zhao, J. Maier, Y. Yu, L. Li, Superior sodium storage in $Na_2Ti_3O_7$ nanotube Arrays through surface engineering, Adv. Energy Mater. 6 (2016) 1502568.

[220] H. Li, L. Peng, Y. Zhu, D. Chen, X. Zhang, G. Yu, An advanced high-energy sodium ion full battery based on nanostructured $Na_2Ti_3O_7$/$VOPO_4$ layered materials, Energy Environ. Sci. 9 (2016) 3399–3405.

[221] M. Vujković, M. Mitrić, S. Mentus, High-rate intercalation capability of $NaTi_2(PO_4)_3$/C composite in aqueous lithium and sodium nitrate solutions, J. Power Sources 288 (2015) 176–186.

[222] D. Wang, Q. Liu, C. Chen, M. Li, X. Meng, X. Bie, Y. Wei, Y. Huang, F. Du, C. Wang, G. Chen, NASICON-structured $NaTi_2(PO_4)_3$@C nanocomposite as the low operation-voltage anode material for high-performance sodium-ion batteries, ACS Appl. Mater. Interfaces 8 (2016) 2238–2246.

[223] B. Babu, M.M. Shaijumon, High performance sodium-ion hybrid capacitor based on $Na_2Ti_2O_4(OH)_2$ nanostructures, J. Power Sources 353 (2017) 85–94.

[224] G. Zou, J. Guo, X. Liu, Q. Zhang, G. Huang, C. Fernandez, Q. Peng, Hydrogenated core–shell MAX@$K_2Ti_8O_{17}$ pseudocapacitance with ultrafast sodium storage and long-term cycling, Adv. Energy Mater. 7 (2017) 1700700.

[225] I. Shakir, M. Sarfraz, Evaluation of electrochemical charge storage mechanism and structural changes in intertwined MoO_3–MWCNTs composites for supercapacitor applications, Electrochim. Acta 147 (2014) 380–384.

[226] I. Shakir, M. Shahid, M. Nadeem, D.J. Kang, Tin oxide coating on molybdenum oxide nanowires for high performance supercapacitor devices, Electrochim. Acta 72 (2012) 134–137.

[227] V.S. Saji, C.-W. Lee, Potential and pH dependent pseudocapacitance of Mo/Mo oxides - an impedance study, Electrochim. Acta 137 (2014) 647–653.

[228] L. Cao, S. Yang, W. Gao, Z. Liu, Y. Gong, L. Ma, G. Shi, S. Lei, Y. Zhang, S. Zhang, R. Vajtai, P.M. Ajayan, Direct laser-patterned micro-supercapacitors from paintable MoS_2 films, Small 9 (2013) 2905–2910.

[229] M.A. Bissett, I.A. Kinloch, R.A.W. Dryfe, Characterization of MoS_2–graphene composites for high-performance coin cell supercapacitors, ACS Appl. Mater. Interfaces 7 (2015) 17388–17398.

[230] L. Huang, Q. Wei, X. Xu, C. Shi, X. Liu, L. Zhou, L. Mai, Methyl-functionalized MoS_2 nanosheets with reduced lattice breathing for enhanced pseudocapacitive sodium storage, Phys. Chem. Chem. Phys. 19 (2017) 13696–13702.

[231] R. Wang, S. Wang, X. Peng, Y. Zhang, D. Jin, P.K. Chu, L. Zhang, Elucidating the intercalation pseudocapacitance mechanism of MoS_2–carbon monolayer interoverlapped superstructure: toward high-performance sodium-ion-based hybrid supercapacitor, ACS Appl. Mater. Interfaces 9 (2017) 32745–32755.

[232] C. Zhao, C. Yu, M. Zhang, Q. Sun, S. Li, M. Norouzi Banis, X. Han, Q. Dong, J. Yang, G. Wang, X. Sun, J. Qiu, Enhanced sodium storage capability enabled by super wide-interlayer-spacing MoS_2 integrated on carbon fibers, Nano-mater. Energy 41 (2017) 66–74.

[233] Z. Chen, V. Augustyn, X. Jia, Q. Xiao, B. Dunn, Y. Lu, High-performance sodium-ion pseudocapacitors based on hierarchically porous nanowire composites, ACS Nano 6 (2012) 4319–4327.

[234] M. Yao, P. Wu, S. Cheng, L. Yang, Y. Zhu, M. Wang, H. Luo, B. Wang, D. Ye, M. Liu, Investigation into the energy storage behaviour of layered α-V_2O_5 as a pseudo-capacitive electrode using operando Raman spectroscopy and a quartz crystal microbalance, Phys. Chem. Chem. Phys. 19 (2017) 24689–24695.

[235] X. Pan, Y. Zhao, G. Ren, Z. Fan, Highly conductive VO_2 treated with hydrogen for supercapacitors, Chem. Commun. (Camb.) 49 (2013) 3943–3945.

[236] R. Sun, Q. Wei, J. Sheng, C. Shi, Q. An, S. Liu, L. Mai, Novel layer-by-layer stacked VS_2 nanosheets with intercalation pseudocapacitance for high-rate sodium ion charge storage, Nanomater. Energy 35 (2017) 396–404.

[237] D. Yu, Q. Pang, Y. Gao, Y. Wei, C. Wang, G. Chen, F. Du, Hierarchical flower-like VS_2 nanosheets – a high rate-capacity and stable anode material for sodium-ion battery, Energy Storage Mater 11 (2018) 1–7.

[238] M. Vujković, S. Mentus, Potentiodynamic and galvanostatic testing of $NaFe_{0.95}V_{0.05}PO_4$/C composite in aqueous $NaNO_3$ solution, and the properties of aqueous $Na_{1.2}V_3O_8$/$NaNO_3$/$NaFe_{0.95}V_{0.05}PO_4$/C battery, J. Power Sources 325 (2016) 185–193.

[239] L. Wang, X. Bi, S. Yang, Partially single-crystalline mesoporous Nb_2O_5 nanosheets in between graphene for ultrafast sodium storage, Adv. Mater. 28 (2016) 7672–7679.

[240] L. Yang, Y.-E. Zhu, J. Sheng, F. Li, B. Tang, Y. Zhang, Z. Zhou, T-Nb_2O_5/C nanofibers prepared through electrospinning with prolonged cycle durability for high-rate sodium-ion batteries induced by pseudocapacitance, Small (2017) 1702588.

[241] H. Li, Y. Zhu, S. Dong, L. Shen, Z. Chen, X. Zhang, G. Yu, Self-assembled Nb_2O_5 nanosheets for high energy–high power sodium ion capacitors, Chem. Mater. 28 (2016) 5753–5760.

[242] L. Yan, G. Chen, S. Sarker, S. Richins, H. Wang, W. Xu, X. Rui, H. Luo, Ultrafine Nb_2O_5 nanocrystal coating on reduced graphene oxide as anode material for high performance sodium ion battery, ACS Appl. Mater. Interfaces 8 (2016) 22213–22219.

[243] M.R. Lukatskaya, O. Mashtalir, C.E. Ren, Y. Dall'Agnese, P. Rozier, P.L. Taberna, M. Naguib, P. Simon, M.W. Barsoum, Y. Gogotsi, Cation intercalation and high volumetric capacitance of two-dimensional titanium carbide, Science 341 (2013) 1502–1505.

[244] Y. Dall'Agnese, P.-L. Taberna, Y. Gogotsi, P. Simon, Two-dimensional vanadium carbide (MXene) as positive electrode for sodium-ion capacitors, J. Phys. Chem. Lett. 6 (2015) 2305–2309.

[245] X. Wang, S. Kajiyama, H. Iinuma, E. Hosono, S. Oro, I. Moriguchi, M. Okubo, A. Yamada, Pseudocapacitance of MXene nanosheets for high-power sodium-ion hybrid capacitors, Nat. Commun. 6 (2015) 6544.

[246] X. Ji, K. Xu, C. Chen, B. Zhang, Y. Ruan, J. Liu, L. Miao, J. Jiang, Probing the electrochemical capacitance of MXene nanosheets for high-performance pseudocapacitors, Phys. Chem. Chem. Phys. 18 (2016) 4460–4467.

[247] S. Kajiyama, L. Szabova, K. Sodeyama, H. Iinuma, R. Morita, K. Gotoh, Y. Tateyama, M. Okubo, A. Yamada, Sodium-ion intercalation mechanism in MXene nanosheets, ACS Nano 10 (2016) 3334–3341.

[248] K.-T. Lee, N.-L. Wu, Manganese oxide electrochemical capacitor with potassium poly(acrylate) hydrogel electrolyte, J. Power Sources 179 (2008) 430–434.

[249] Q. Li, X. Sun, K. Lozano, Y. Mao, Asymmetric supercapacitors with dominant pseudocapacitance based on manganese oxide nanoflowers in a neutral aqueous electrolyte, RSC Adv. 3 (2013) 24886–24890.

[250] L.L. Cao, B.Z. Yu, T. Cheng, X.L. Zheng, X.H. Li, W.L. Li, Z.Y. Ren, H.M. Fan, Optimized K^+ pre-intercalation in layered manganese dioxide nanoflake arrays with high intercalation pseudocapacitance, Ceram. Int. 43 (2017) 14897–14904.

[251] Z. Zeng, Y. Liu, W. Zhang, H. Chevva, J. Wei, Improved supercapacitor performance of MnO_2-electrospun carbon nanofibers electrodes by mT magnetic field, J. Power Sources 358 (2017) 22–28.

[252] B.P. Bakhmatyuk, B.Y. Venhryn, Grygorchak II, M.M. Micov, S.I. Mudry, Intercalation pseudo-capacitance in carbon systems of energy storage, Rev. Adv. Mater. Sci. 14 (2007) 151–156.

[253] C. Chen, Z. Wang, B. Zhang, L. Miao, J. Cai, L. Peng, Y. Huang, J. Jiang, Y. Huang, L. Zhang, J. Xie, Nitrogen-rich hard carbon as a highly durable anode for high-power potassium-ion batteries, Energy Storage Mater 8 (2017) 161–168.

[254] S. Maiti, A. Pramanik, S. Mahanty, Extraordinarily high pseudocapacitance of metal organic framework derived nanostructured cerium oxide, Chem. Commun. (Camb.) 50 (2014) 11717–11720.

[255] S.-Y. Lin, X. Zhang, Two-dimensional titanium carbide electrode with large mass loading for supercapacitor, J. Power Sources 294 (2015) 354–359.

[256] D. Guan, X. Gao, J. Li, C. Yuan, Enhanced capacitive performance of TiO_2 nanotubes with molybdenum oxide coating, Appl. Surf. Sci. 300 (2014) 165–170.

[257] X. Xiao, C. Zhang, S. Lin, L. Huang, Z. Hu, Y. Cheng, T. Li, W. Qiao, D. Long, Y. Huang, L. Mai, Y. Gogotsi, J. Zhou, Intercalation of cations into partially reduced molybdenum oxide for high-rate pseudocapacitors, Energy. Storage Mater 1 (2015) 1–8.

[258] K. Tian, L. Wei, X. Zhang, Y. Jin, X. Guo, Membranes of carbon nanofibers with embedded MoO_3 nanoparticles showing superior cycling performance for all-solid-state flexible supercapacitors, Mater, Today Energy 6 (2017) 27–35.

[259] J.L. Acosta, E. Morales, Synthesis and characterization of polymeric electrolytes for solid state magnesium batteries, Electrochim. Acta 43 (1998) 791–797.

[260] C. Liebenow, A novel type of magnesium ion conducting polymer electrolyte, Electrochim. Acta 43 (1998) 1253–1256.

[261] G.G. Kumar, N. Munichandraiah, Reversibility of Mg/Mg^{2+} couple in a gel polymer electrolyte, Electrochim. Acta 44 (1999) 2663–2666.

[262] G.G. Amatucci, F. Badway, A. Singhal, B. Beaudoin, G. Skandan, T. Bowmer, I. Plitz, N. Pereira, T. Chapman, R. Jaworski, Investigation of yttrium and polyvalent ion intercalation into nanocrystalline vanadium oxide, J. Electrochem. Soc. 148 (2001) A940–A950.

[263] G. Gershinsky, H.D. Yoo, Y. Gofer, D. Aurbach, Electrochemical and spectroscopic analysis of Mg^{2+} intercalation into thin film electrodes of layered oxides: V_2O_5 and MoO_3, Langmuir 29 (2013) 10964–10972.

[264] Y.J. He, J.F. Peng, W. Chu, Y.Z. Li, D.G. Tong, Retracted Article: black mesoporous anatase TiO_2 nanoleaves: a high capacity and high rate anode for aqueous Al-ion batteries, J. Mater. Chem. 2 (2014) 1721–1731.

[265] Z. Li, K. Xiang, W. Xing, W.C. Carter, Y.-M. Chiang, Reversible aluminum-ion intercalation in prussian blue analogs and demonstration of a high-power aluminum-ion asymmetric capacitor, Adv. Energy Mater. 5 (2015) 1401410.

[266] H. Jiao, J. Wang, J. Tu, H. Lei, S. Jiao, Aluminum-ion asymmetric supercapacitor incorporating carbon nanotubes and an ionic liquid electrolyte: Al/$AlCl_3$-[EMIm]Cl/CNTs, Energy Technol. 4 (2016) 1112–1118.
[267] K. Li, Y. Shao, S. Liu, Q. Zhang, H. Wang, Y. Li, R.B. Kaner, Aluminum-ion-intercalation supercapacitors with ultrahigh areal capacitance and highly enhanced cycling stability: power supply for flexible electrochromic devices, Small 13 (2017) 1700380.
[268] T. Kudo, Electrochemical behavior of the perovskite-type $Nd_{1-x}Sr_xO_3$ in an aqueous alkaline solution, J. Electrochem. Soc. 122 (1975) 159.
[269] R. Roy, Multiple ion substitution in the perovskite lattice, J. Am. Ceram. Soc. 37 (1954) 581–588.
[270] E. Magnone, G. Cerisola, M. Ferretti, A. Barbucci, Electrochemical investigation of oxygen intercalation into $La_2CuO_{4+\delta}$ phases, J. Solid State Chem. 144 (1999) 8–15.
[271] E. Goldberg, A. Nemudry, V. Boldyrev, R. Schöllhorn, Model for anomalous transport of oxygen in nonstoichiometric perovskites: 1. General formulation of the problem, Solid. State Ionics 110 (1998) 223–233.
[272] E. Goldberg, A. Nemudry, V. Boldyrev, R. Schöllhorn, Model for anomalous transport of oxygen in nonstoichiometric perovskites: analytical and numerical solutions, Solid State Ionics 122 (1999) 17–22.
[273] A. Nemudry, E.L. Goldberg, M. Aguirre, M.Á. Alario-Franco, Electrochemical topotactic oxidation of nonstoichiometric perovskites at ambient temperature, Solid State Sci. 4 (2002) 677–690.
[274] R.P. Forslund, J. Pender, C.T. Alexander, K.P. Johnston, K.J. Stevenson, Comparison of perovskite and perovskite derivatives for use in anion-based pseudocapacitor applications, J. Mater. Chem. 7 (2019) 21222–21231.
[275] J. Sunarso, S. Baumann, J.M. Serra, W.A. Meulenberg, S. Liu, Y.S. Lin, J.C. Diniz da Costa, Mixed ionic–electronic conducting (MIEC) ceramic-based membranes for oxygen separation, J. Membr. Sci. 320 (2008) 13–41.
[276] X.W. Wang, Q.Q. Zhu, X.E. Wang, H.C. Zhang, J.J. Zhang, L.F. Wang, Structural and electrochemical properties of $La_{0.85}Sr_{0.15}MnO_3$ powder as an electrode material for supercapacitor, J. Alloys Compd. 675 (2016) 195–200.
[277] X. Lang, H. Mo, X. Hu, H. Tian, Supercapacitor performance of perovskite $La_{1-x}Sr_xMnO_3$, Dalton Trans. 46 (2017) 13720–13730.
[278] Y. Cao, B. Lin, Y. Sun, H. Yang, X. Zhang, Symmetric/asymmetric supercapacitor based on the perovskite-type lanthanum cobaltate nanofibers with Sr-substitution, Electrochim. Acta 178 (2015) 398–406.
[279] P.P. Ma, B. Zhu, N. Lei, Y.K. Liu, B. Yu, Q.L. Lu, J.M. Dai, S.H. Li, G.H. Jiang, Effect of Sr substitution on structure and electrochemical properties of perovskite-type $LaMn_{0.9}Ni_{0.1}O_3$ nanofibers, Mater. Lett. 252 (2019) 23–26.
[280] Z. Wang, Y. Liu, Y. Chen, L. Yang, Y. Wang, M. Wei, A-site cation-ordered double perovskite $PrBaCo_2O_{5+\delta}$ oxide as an anion-inserted pseudocapacitor electrode with outstanding stability, J. Alloys Compd. 810 (2019) 151830.
[281] T. Tabari, D. Singh, A. Calisan, M. Ebadi, H. Tavakkoli, B. Caglar, Microwave assisted synthesis of $La_{1-x}Ca_xMnO_3$ (x = 0, 0.2 and 0.4): structural and capacitance properties, Ceram. Int. 43 (2017) 15970–15977.
[282] N. Arjun, G.-T. Pan, T.C.K. Yang, The exploration of Lanthanum based perovskites and their complementary electrolytes for the supercapacitor applications, Results Phys 7 (2017) 920–926.
[283] M.P. Harikrishnan, A.C. Bose, Perovskite oxide $LaCoO_3$ electrode as high performance pseudocapacitor, AIP Conf. Proc. 2082 (2019), 060001.
[284] Z.A. Elsiddig, H. Xu, D. Wang, W. Zhang, X. Guo, Y. Zhang, Z. Sun, J. Chen, Modulating Mn^{4+} ions and oxygen vacancies in nonstoichiometric $LaMnO_3$ perovskite by a facile sol-gel method as high-performance supercapacitor electrodes, Electrochim. Acta 253 (2017) 422–429.
[285] G. George, S.L. Jackson, C.Q. Luo, D. Fang, D. Luo, D. Hu, J. Wen, Z. Luo, Effect of doping on the performance of high-crystalline $SrMnO_3$ perovskite nanofibers as a supercapacitor electrode, Ceram. Int. 44 (2018) 21982–21992.
[286] Y. Guo, T. Shao, H. You, S. Li, C. Li, L. Zhang, Polyvinylpyrrolidone-assisted solvothermal synthesis of porous $LaCoO_3$ nanospheres as supercapacitor electrode, Int. J. Electrochem. Sci. 12 (2017) 7121–7127.
[287] Z. Li, W. Zhang, H. Wang, B. Yang, Two-dimensional perovskite $LaNiO_3$ nanosheets with hierarchical porous structure for high-rate capacitive energy storage, Electrochim. Acta 258 (2017) 561–570.
[288] Q. Hu, B. Yue, F. Yang, H. Shao, J. Wang, L. Ji, Y. Jia, Y. Wang, J. Liu, Facile synthesis and electrochemical properties of perovskite-type $CeMnO_3$ nanofibers, ChemistrySelect 4 (2019) 11903–11912.
[289] A.K. Tomar, G. Singh, R.K. Sharma, Charge storage characteristics of mesoporous strontium titanate perovskite aqueous as well as flexible solid-state supercapacitor cell, J. Power Sources 426 (2019) 223–232.
[290] Z.A. Elsiddig, D. Wang, H. Xu, W. Zhang, T. Zhang, P. Zhang, W. Tian, Z. Sun, J. Chen, Three-dimensional nitrogen-doped graphene wrapped $LaMnO_3$ nanocomposites as high-performance supercapacitor electrodes, J. Alloys Compd. 740 (2018) 148–155.
[291] Y. Liu, Z. Wang, Y. Zhong, M. Tade, W. Zhou, Z. Shao, Molecular design of mesoporous $NiCo_2O_4$ and $NiCo_2S_4$ with sub-micrometer-polyhedron architectures for efficient pseudocapacitive energy storage, Adv. Funct. Mater. 27 (2017) 1701229.
[292] P.M. Shafi, V. Ganesh, A.C. Bose, $LaMnO_3$/RGO/PANI ternary nanocomposites for supercapacitor electrode application and their outstanding performance in all-solid-state asymmetrical device design, ACS Appl. Energy Mater. 1 (2018) 2802–2812.
[293] L. He, Y. Shu, W. Li, M. Liu, Preparation of $La_{0.7}Sr_{0.3}CoO_{3-\delta}$ (LSC)@MnO_2 core/shell nanorods as high-performance electrode materials for supercapacitors, J. Mater. Sci. Mater. Electron. 30 (2019) 17–25.
[294] X. Lang, X. Sun, Z. Liu, H. Nan, C. Li, X. Hu, H. Tian, Ag nanoparticles decorated perovskite $La_{0.85}Sr_{0.15}MnO_3$ as electrode materials for supercapacitors, Mater. Lett. 243 (2019) 34–37.
[295] L. Huang, Q. Li, G. Zhang, X. Zhou, Z. Shao, W. Zhou, J. Cao, The preparation of $LaSr_3Fe_3O_{10-\delta}$ and its electrochemical performance, J. Solid State Electrochem. 21 (2017) 1343–1348.
[296] Z. Sang, W. Che, S. Yang, Y. Liu, Ruddlesden-Popper type $La_2NiO_{4+\delta}$ oxide as a pseudocapacitor electrode, Mater. Lett. 217 (2018) 23–26.
[297] M. Wei, W. Che, H. Li, Z. Wang, F. Yan, Y. Liu, J. Liu, Ruddlesden-Popper type $La_2NiO_{4+\delta}$ oxide coated by Ag nanoparticles as an outstanding anion intercalation cathode for hybrid supercapacitors, Appl. Surf. Sci. 484 (2019) 551–559.
[298] A. Ajay, A. Paravannoor, J. Joseph, V. Amruthalakshmi, S.S. Anoop, S.V. Nair, A. Balakrishnan, 2 D amorphous frameworks of $NiMoO_4$ for supercapacitors: defining the role of surface and bulk controlled diffusion processes, Appl. Surf. Sci. 326 (2015) 39–47.
[299] T. Ling, P. Da, X. Zheng, B. Ge, Z. Hu, M. Wu, X.-W. Du, W.-B. Hu, M. Jaroniec, S.-Z. Qiao, Atomic-level structure engineering of metal oxides for high-rate oxygen intercalation pseudocapacitance, Sci. Adv. 4 (2018), eaau6261.
[300] S. Nagamuthu, S. Vijayakumar, K.-S. Ryu, Cerium oxide mixed $LaMnO_3$ nanoparticles as the negative electrode for aqueous asymmetric supercapacitor devices, Mater. Chem. Phys. 199 (2017) 543–551.
[301] P.M. Shafi, N. Joseph, A. Thirumurugan, A.C. Bose, Enhanced electrochemical performances of agglomeration-free $LaMnO_3$ perovskite nanoparticles and achieving high energy and power densities with symmetric supercapacitor design, Chem. Eng. J. 338 (2018) 147–156.